Stability of zinc phthalocyanine and fullerene C_{60} organic solar cells

DISSERTATION

zur Erlangung des akademischen Grades

Doctor rerum naturalium
(Dr. rer. nat.)

vorgelegt

der Fakultät Mathematik und Naturwissenschaften
der Technischen Universität Dresden

von

M.Sc. Rudolf Lessmann

geboren am 3 Mai 1978 in Trier

Eingereicht am 12/10/2009

Die Dissertation wurde in der Zeit von 04 / 2005 bis 09 / 2009
im Institut für Angewandte Photophysik angefertigt.

1. Gutachter: Prof. Dr. K. Leo

2. Gutachter: Prof. Dr. H. Lakner

Tag der Verteidigung: 10.05.2010

This work is dedicated to my parents, Margaretha and Werner Lessmann, to my brother Raphael, and to my better half 崔小波 *(Cuīxiǎobō)*

Abstract

Organic solar cells promise electricity generation at very low cost, and higher installation flexibility as compared to inorganic solar cells. The lower cost is achieved by cheaper semiconductors and easier manufacturing processes. The flexibility is naturally given by these ultra-thin, amorphous layers. Also the power conversion efficiency can be high enough for many applications. The organic molecules have to withstand the constant excitation by photons, transport of energy in form of excitons and charge. A small but significant amount of these photons has energy over the absorption gap, the excess of energy must be released without breaking the molecular bonds. In consequence, the solar cells can also heat up to temperatures at above 80 ºC. The objective of this work is to answer the question if the small molecules organic solar cells can be stable enough to operate under a very long time. The stability of organic doped layers in an organic solar cell is also addressed. This work starts with a general introduction followed by the description of the experimental procedures. The aging experiments of the solar cell were done with a self developed equipment. The fabrication of this equipment (a set of measurement boxes) was necessary to maintain the conditions, under which a solar cell can be aged, as constant as possible. The measurement boxes were used to control the electrical load of the cell, its temperature, the illumination intensity, and its electric connection to the I *vs.*V measurement equipment. A software package was also developed to control the equipment and to facilitate the work and visualization of the high volume of collected data. The model solar cells chosen for the aging experiments were donor-acceptor heterojunctions devices formed with the well-known materials C_{60} and Zinc Phthalocyanine. Two basic different structures were analyzed, because they offered reasonable performance and potentially long lifetime: the flat heterojunction (FHJ) and the mixed heterojunction in a Metal-Insulator-p-Semiconductor (m-i-p) configuration. Variations of the FHJ and of the m-i-p structures are also used to verify the limits of the stability of electrically p- and n- doped organic semiconducting layers. The least stable solar cells are the FHJ devices. These devices show a fast initial decrease of all their characteristic conversion parameters but the open circuit voltage. After a few hundred hours, the saturation current (current under a reverse bias of 1 V) was almost stable. The saturation current is related to the number of absorbing centers, the decrease indicates that the degradation of the absorbing centers has stopped. With wavelength resolved external quantum efficiency measurements and chemical analysis, it was found that the degradation is related to the oxidation of C_{60}. It was also shown that the use of organic dopants do not significantly affect the lifetime. The results show that the m-i-p solar cells are more stable than the FHJ devices. They are also stable under high temperatures up to 105 ºC. Outdoor testing also showed that the solar cells remained chemically, electrically and mechanically stable during a 900 h test.

Contents

List of Figures

B	electrical susceptance
C_{ADC}	ADC conversion factor
C_B	conduction band
E	energy
E_{A}	activation energy
E_{a}	electron affinity
ξ	Fermi level
E_{EX}	vertical excitation energy (absorption)
E_{Vac}	vacuum energy level
ϵ	permittivity
E_{ph}	photon energy
E_X	exciton energy
FF	fill factor
F	electrical field
ϕ	barrier height
G	electrical conductance
I	current
I_L	photo current
I_{SC}	short circuit current
I_{PH}	photo current
$I(-1\mathrm{V})$	current at -1 V, approximated to saturation current
I_0	reverse bias saturation current
IP	ionization potential
IP_D	ionization potential of the donor
IP_A	ionization potential of the acceptor
ISC	intersystem crossing
J_{SCLC}	space charge limited current density
k_{B}	Boltzmann constant
m-i-p	Metal-Insulator-p-Semiconductor
MPP	maximum power point
μ	charge carrier mobility
μ_e	electron mobility
μ_h	hole mobility
μ_{S}	Seebeck mobility
n	ideality factor
N_C	density of conduction states
N_V	density of valence states
Nr_{ph}	number of photons
Nr_{el}	number of electrons
ν	frequency
n_e	density of electrons
n_h	density of holes
P	polarization
q	charge
R	electrical resistance
$R(\lambda)$	responsivity
R_S	series resistance
R_{sh}	shunt resistance
R_{PT1K}	resistance of the temperature sensor (platinum resistor)
S	reverse saturation ratio
S_{Seebeck}	Seebeck coefficient
T_{g}	glass transition temperature
θ	phase of Impedance
V	voltage
V_B	valence band
V_{OC}	open circuit voltage
X	electrical reactance
ξ_X	exciton binding energy
Y	electrical admitance
Z	electrical impedance

Introduction

Solar cells are only one type of many different solar energy converters, which are parts of a larger group of energy sources, the so-called renewable sources. Renewable source does mean, in principle, that the energy source will not run out by use. Equipment for extraction of energy originating from renewable sources is being produced on a large scale, e.g., for hydroelectric and eolic power, for ethanol production from sugar-cane, and in a smaller scale for photovoltaics. The economical benefits of the production and use are obvious [4], otherwise no industrial mass production would be justified. Some economical benefits are generated by governments like Germany and Denmark. They foresee greater political independence from other countries that nowadays are the main suppliers of energy sources in form of fossil fuel [5]. Furthermore, some countries decided not to further develop nuclear fission power [6].

The energy sources available on Earth can be divided into primary and non-primary. The primary are the energy irradiated from the Sun, the nuclear energy, and the tidal energy. The geothermal energy can also be treated as primary. Non-primary energy sources are e.g. wind, potential-gravitational energy from the water, and biomass; all those are renewable and driven by the energy from the Sun. Also generated with Sun energy are the non-renewable carbon deposits in form of petrol, gas, and coal.

The total world energy consumption is increasing as developing countries are approaching the industrialization level of the richest countries. The energy consumption of a country is roughly reflected by its gross domestic product. From the common forms of energy sources used, the most preferred type is the electrical energy, because it can be easily transmitted over very long distances [7], and easily be converted into thermal energy, mechanical energy, and electromagnetic energy (specially light). The electrical energy also drives the revolution of the information technology. One drawback of the electrical energy is that large amounts of charge cannot be easily stored. To be stored in large density, the electrical energy is usually converted into chemical energy or potential gravitational energy [8].

Two examples of efficient harvesting of energy are the use of the solar irradiation to heat water and the use of wind to generate electricity. The most interesting deployment of energy would be realized by the efficient conversion of primary energy into electricity. The Sun is the obvious choice as energy source, it delivers 1 366 W/m^2 over the Earth cross-section, 1 000 W/m^2 are left after the absorption from the atmosphere. Approximately 3 % of the Earth's solid surface is urban area, given a cross section of illuminated urban area of $3.8 \cdot 10^6$ km^2. In a rough estimation, 10% of this area can be considered roof, where $\sim$ 380 TW of power is not profitably used. Conventional Si photovoltaic modules can convert more than 10% of this energy into electricity. 38 TWh could be generated in one hour, that is twice of the energy that the world consumes. This calculation has not yet considered non-urban areas, especial solar parks, and large desert areas that could be used for light harvesting. The increase in demand could be partly covered by the increase in efficiency of the solar cells for some time. This shows that the earth energy demands can be completely supplied by the solar energy.

Photovoltaic is not yet the dominant form of electricity generation because other sources are still cheaper. They tend to be more expensive if, e.g. the pollution caused by burning fossil fuel is taken into account. Furthermore, the production of inorganic solar cells is very expensive, i.e. highly energy consuming. But the Sun delivers its energy for free. This paradoxal situation can only be changed when the installed amount of photovoltaic converters becomes very large. If it is not done by leagal measures then only economic benefits can drive the changes of the energy sources from fossil to renewable sources.

For the time being, the electrical energy will not be for free and will follow more or less the market dynamics. It is then obvious that the cheapest sources will continue to be the most widely used ones. The photovoltaic market has a good chance when it comes to organic solar cells. Some organic dyes with a very high absorption coefficient can be used to fabricate very thin solar cells. With a mixture, e.g. of fullerene and phthalocyanine, almost all of the incident visible solar radiation can easily be absorbed, in a converter that is only about $1\,\mu$m thick [9]. This thin film device can be produced very cheaply. It is estimated that, for large-scale production (reel to reel), the price of the organic materials is less relevant than the price of substrate and electrodes [10]. However, there are some limitations in efficiency that still have to be overcome. Efficiency is one of the key issues for organic solar cells. The only intrinsic limitation of conversion efficiency seems to be the high amount of energy lost when the charges, that are created by light (photon) absorption, are separated. The excitonic binding energy is still large compared to the photon energy itself. Other limitations are the limited transport capabilities of organic semiconductors, i.e. the low mobility of the charge carriers that limits the practical maximum thickness of the absorbing layers. This limitation can be efficiently overcome with the use of multiple junction solar cells [11].

OLEDs and organic solar cells can be compared because they perform a complementary process, transforming electrons in photons ou vice-versa. The intermediate step is an excited state of the organic semiconductor called exciton. A simplification of both processes is represented by the equation below.

$$\begin{array}{ccccc} \multicolumn{5}{c}{\xrightarrow{\qquad\text{OLED}\qquad}} \\ e+h & \rightleftharpoons & \mathit{exciton} & \rightleftharpoons & \mathit{photon} \\ \multicolumn{5}{c}{\xleftarrow{\qquad\text{organic solar cell}\qquad}} \end{array}$$

OLEDs can be made with very stable emitter materials, also emitting blue light (fluorescent emitters). In contrast, organic solar cells are, in most of the applications, submitted to much higher energy excitations.

Although OLEDs have achieved a very high photon to electron conversion efficiency of up to 20% [12], this high efficiency can not be directly taken as a must for organic solar cells. An OLED emitting monochromatic or mixed light (e.g. white) emits photons with defined energy, typically limited between 1.5 eV and 3.0 eV. The comparison is not straight forward because an ideal solar cell needs to harvest all the incident solar light, which spectrum has a nearly black body photon energy distribution. A standard solar spectrum is shown in figure 1. The visible region represents a large amount of the incident energy, considerable power is also available in the infra-red region. The more narrow region of the ultra violet, with wavelengths below 400 nm is labeled in the figure by “UV”.

A general concern about OLEDs and organic solar cells is the chemical stability of the compounds which are directly involved to energy conversion process (charge into photon and vice-versa). In organic semiconductors this process usually includes an intermediate step, in which the opposite charge carriers are bound in the form of excitons. The concern is that the high energies related to the process below can either break a chemical bound (fragmentation of the molecule) or enable a chemical reaction with another molecule:

Ways to overcome these issues are provide by UV filtering e.g. by a glass substrate, additional UV filters, and fast exciton separation in the solar cell. Most of the higher efficient small molecule solar cells includes a fullerene compound, which has a long triplet exciton decay time of ~50 ms [13]. The separation of excitons is usually very fast in so called bulk heterojunction solar cells. There, materials that are electron acceptor and electron donor are mixed in the same layer creating a large surface interface.

An approach to make stable devices is to choose materials that are known to be stable under harsh conditions such as high illumination in a reactive environment. A large set of experimental organic solar cells uses C_{60} or a derivative like PCBM [14–16]. This fullerene derivatives are chemically more

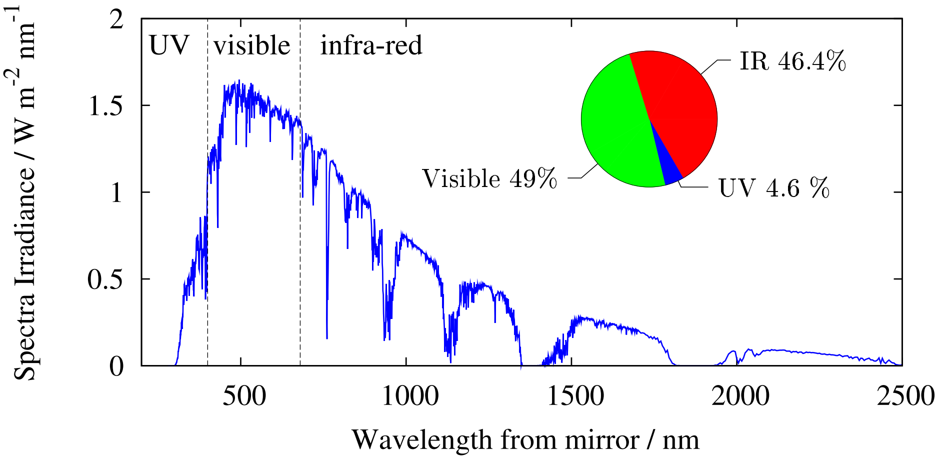

Figure 1: AM 1.5 Solar spectrum. The AM1.5 spectrum refers to "air mass 1.5", meaning that the incident light gets absorbed and scattered by passing trough the equivalent of 1.5 times the atmosphere thickness.

reactive than planar cyclic carbon systems. Due to the bending of the rings, they do not have the same stability as aromatic molecules. Still, it is known that those molecules are remarkably stable in devices [17, 18]. Phthalocyanines, especially ZnPc, are highly stable in the solid state, even exposed to air and to light [19]. They are also good charge carriers transporters and some have adequate energy levels to be combined with C_{60}. Those materials also have other advantages, such as high thermal stability. Therefore, the combination of ZnPc and C_{60} seem to be a good choice to form stable heterojunction organic solar cells.

This work addresses the aging of organic solar cells that uses ZnPc/C_{60} heterojunctions as photoelectric active layers. The next chapter 1 is a general introduction to the physics of organic semiconductors focusing on small molecule solar cells.

The following chapter 2 describe the materials and the experimental setups. One special chapter (chapter 3) is about the experimental setup developed for the lifetime measurements. The measurement results chapters are divided into two, chapter 4 with a conventional Tang like structure [20] and the chapter 5 with an inverted m-i-p bulk heterojunction structure [21].

Chapter 1

Organic semiconductors

The joined efforts of chemists and physicist on studying electronic transfer processes in biological and synthetic molecules allowed considerable progress in understanding carrier transport in molecular solids. The understanding of physicochemical properties of organic molecules and their controlled modification has enabled their successful use in electronic devices. In the last years, the accumulated knowledge on light emitting diodes and solar cells containing organic molecules as optoelectronic active materials has been adopted by the industry. Consumer products are already in the market, e.g. displays made of organic light emitting diodes [22] and solar cells [23]. This chapter presents an overview of the established knowledge about organic semiconductors and organic solar cells.

1.1 Fundamentals of organic semiconductors

1.1.1 Materials with conjugated double bonds

The majority of optically and electronically active compounds used in molecular electronics research are organic conjugated molecules. The conjugation refers to alternating single and double π bonds. They are called organic in the sense that C atoms participate in the conjugation. Due to their typically weak Van der Waals attraction forces, they are also called soft semiconductors.

The ground electronic structure of a carbon atom is $1s^2 2s^2 2p^2$. Its $2p$ orbitals can mix with the $2s$ orbitals to form hybrid sp^2 orbitals. This atom with electronic configuration $1s^2 2sp^{2^1} 2sp^{2^1} 2sp^{2^1} 2p^1$ can make four bonds. The hybrid orbitals are all in the same plane, separated by an angle of 120^o and are all orthogonal to the remaining $2p$ orbital. In a double C=C bond as in the C_2H_4 molecule (See Fig. 1.1.1), a σ C-C bond is formed by a $sp^2 - sp^2$ bond. It is highly overlapping and also called covalent. Each C atom is also bonded to a H atom via σ bond. Another C-C bond is formed by the weaker overlapping of the 2 parallel p orbitals and it is called π bond. The π bond is the weakest; the first electronic transition $\pi - \pi^*$(where π^* is the anti-bonding orbital) has an energy in the range of the visible spectrum ($\sim$ 2 eV).

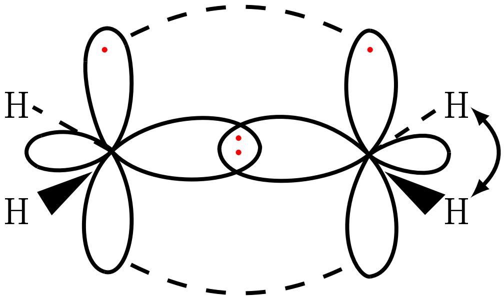

Figure 1.1: Ethylene molecule showing the σ bond formed by the overlap of 2 sp^2 orbitals of the C atoms, and the π orbitals formed with the p orbitals. The remaining 4 p orbitals are bound to the H atoms.

Figure 1.2 shows the effect on the energy levels, when more C atoms are added to the acetylene chain. The carbon-carbon bonds will be alternating between single and double bonds. The carbon p levels are split into binding and anti-binding π orbitals in the C_2H_4 molecule. Adding more carbon atoms will further split the orbitals, and, for a very large number of atoms, there will be a conduction band and a valence band. As a result, very large conjugated chains like semiconducting polymers show very high intra chain charge carrier mobility [24].

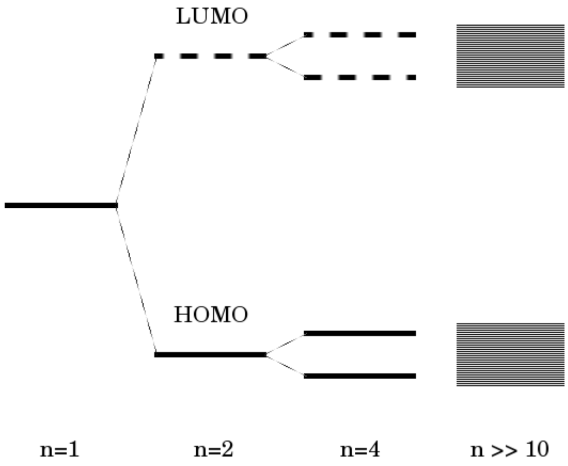

Figure 1.2: Formation and splitting of the highest occupied orbitals (HOMO) and the lowest unoccupied orbital (LUMO) of a linear carbon chain (polyacetylene). The orbitals form a band-like structure for very large chains.

In some conjugated systems, such as benzene in Fig. 1.4, there is no vibronic state related to two hypothetical conjugated electronic configurations of the π-conjugated system[1]. Instead, the π electrons are completely delocalized over all 6 C atoms (see fig. 1.3).

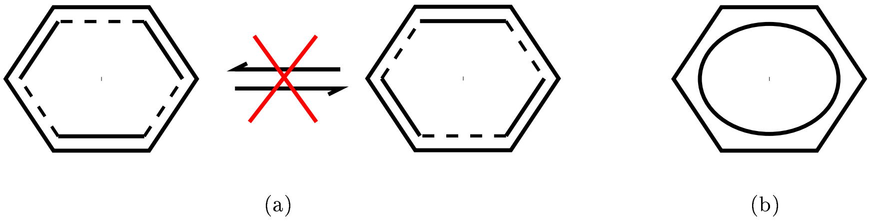

Figure 1.3: (a): Schematic showing that the representation of the bonds in the benzene molecule as alternated bonds is not realistic. (b): is a more convenient representation of the aromatic character of benzene.

Those molecules are called aromatic compounds. This delocalization gives the benzene an extra energy of 36 kcal / mol, called resonance energy, which makes benzene more stable against reactions, compared to e.g. alkenes. Contrary to benzene, the closed 8 carbon molecule 1,3,5,7-Cyclooctatetren (annulene) is not aromatic due to its non-planar geometry [25].

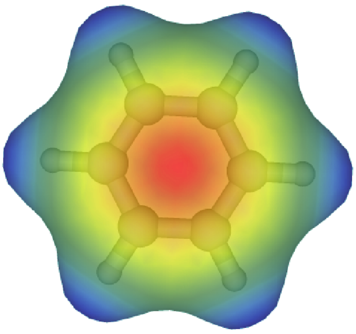

Figure 1.4: Benzene molecule. The colors depict the electrostatic potential, red (inner part) means a higher electron density and blue (outer part) a lower one.

Conjugated molecules have useful optical properties since their electronic (π-π^*) gap is in the UV - vis range. Many classes of compounds have been studied for their optoelectronic properties, some of the most important being benzene derivatives [26], thiophenes [27], triphenylamines [28], fullerenes [29], porphyrins and phtalocyanines [30, 31], and metal complexes [32–34]. Polymers such as polyacetylene [35], polyanilines [36, 37], polythiophenes [38], polyfluorenes [39], and others are also very important. The study of conducting polymers even led to the Nobel prize in chemistry in 2000 to Heeger, MacDiarmid, and Shirakawa [40].

---

[1] see for example, Atkins, Physikalische Chemie, sec. 14.3.1, Benzol und die aromatische Stabilität, pg 467

1.1.2 Optoelectronic transitions - relaxation processes

The energy state of a molecule is a defined quantum state n with wave function $\mid \psi_n >$ whose eigenvalues E can be determined from Schrödinger equation:

$$H \mid \psi_n >= E_n \mid \psi_n > \tag{1.1}$$

where H is the Hamiltonian. The wave function $\mid \psi_n >$ can be split into electronic and vibronic states using the Born-Oppenheimer approximation and the internal coordinates [41]:

$$\mid \psi_{j\nu} >=\mid \varphi_j >\mid \chi_{j\nu} > \tag{1.2}$$

Each electronic state E split into vibrational sublevels and the total energy of a stationary state of a molecule can be separated into two terms [42]:

$$E = E^{(el)} + E^{(vib)} \tag{1.3}$$

The same way, the energy of an electronic excitation can be written as:

$$\Delta E = \Delta E^{(el)} + \Delta E^{(vib)} \tag{1.4}$$

In a similar way, if external coordinates are used, the total energy can be separated in 4 terms:

$$E = E^{(el)} + E^{(vib)} + E^{(rot)} + E^{(trans)} \tag{1.5}$$

In the solid state, the distribution of allowed vibrational energy states of the molecules tends to make the absorption spectrum very broad.

Absorption of light can occur via direct promotion of a singlet electron (in state S$_x$) to a higher singlet state (S$_y$) during absorption of the photon energy $h\nu$. Because this process is adiabatic, an electronic transition into a different vibronic state (S_y^{+vib}) whose wave functions do better overlap [43, 44] is likely to occur.

$$S_x + h\nu^{abs} + E^{(vib)_a} \rightarrow S_y^{+vib} \tag{1.6}$$

The vibronic relaxation period is about 10^{-14} s. Because the density of vibronic levels increases with higher energy, the overlapping of the wave function between the different vibronic levels is greater for higher excited states and the excited state can decay faster. The decay of the excited state through the vibronic levels to the first excited singlet state (S_1) is called internal conversion. The whole process typically takes place in $\sim 10^{-12}$ s.

$$S_y^{+vib} \rightarrow S_y + E^{(vib)_b} \rightarrow S_1 + E^{(vib)c} \tag{1.7}$$

The process is graphically showed in the energy diagram of Fig. 1.5.

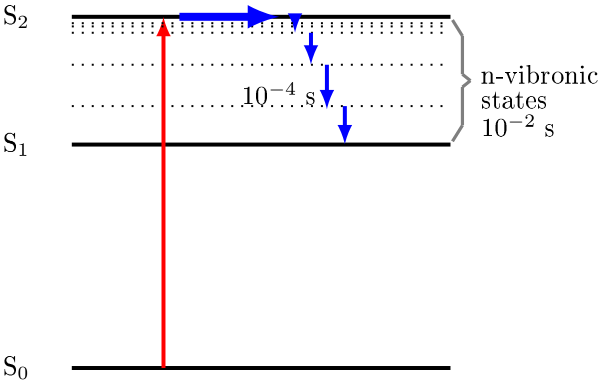

Figure 1.5: Diagram showing the absorption of a photon with high energy promoting an electron to a highly excited energy state. The fast internal conversion to the lowest excited state is shown by the small arrows. The internal conversion occurs on the vibrational energy states (dotted lines).

This state is typically stable for $\sim 10^{-9}$ s and can decay via a thermal deactivation or photon emission. A transfer into a lower state in another molecule can also occur, or a forbidden transition to a triplet state. The transition to a triplet state $S_1 \rightsquigarrow T_1$ (or vice versa $T_1 \rightsquigarrow S_1$) a so-called intersystem crossing (ISC) is only possible by a spin inversion. The rate for ISC (k_{ST} and k_{TS}) is strongly influenced by the spin-orbit coupling [45] and it can be large if the final state has a different orbital type (El Sayed rule [46]). The ISC can be $S_1 \rightsquigarrow T_1$ or $S_1 \rightsquigarrow T_n$, followed by $T_n \rightsquigarrow T_1$, where T_n is an intermediate triplet state ($n > 1$).

The triplet state can further have another ISC back to a singlet state and decay emitting a photon (Kasha's rule [48]). The triplet state has a very low probability of direct radiative decay. The direct transition from a triplet state to the singlet ground state with photon emission is called phosphorescence [49]. It can also deactivate thermally. If an energy transfer of the triplet state to another molecule occurs and it then decays via phosphorescence, it is called delayed phosphorescence. A singlet excited state can be transferred to another molecule via phonon-induced tunneling known as hopping, this process occurs

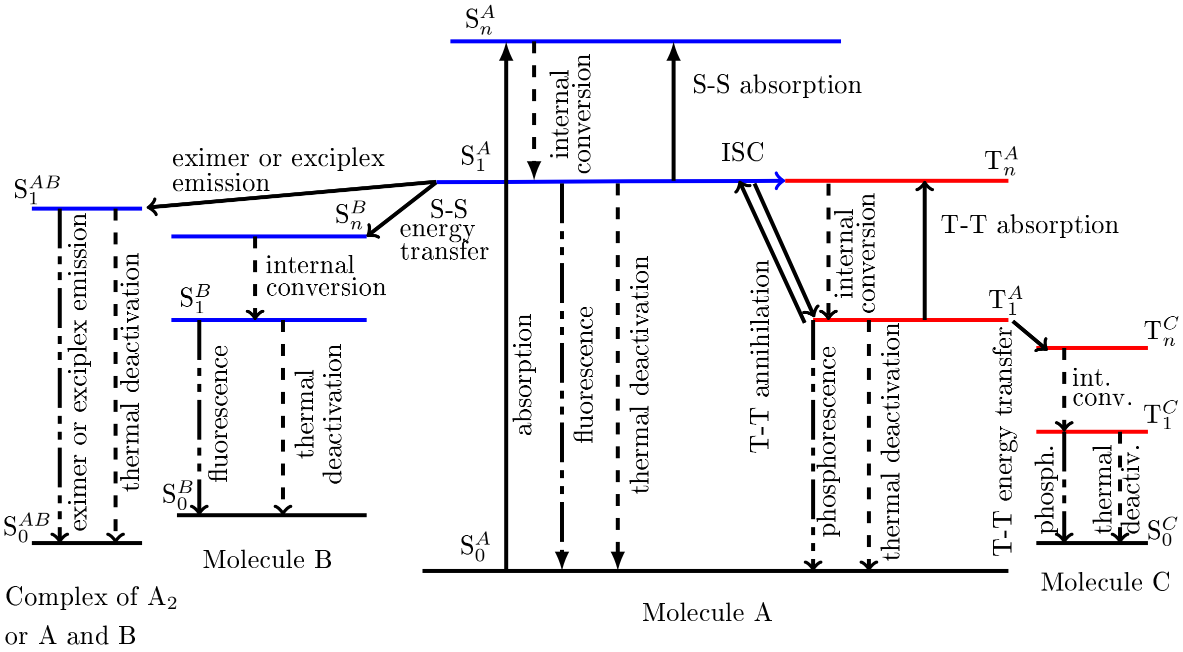

Figure 1.6: Schematic of the possible photochemical and photophysical processes of a molecule. Adapted from [47]. After absorbing a photon and promoting an electron to an excited singlet state in molecule A, the electron will relax to S_1 level by internal conversion. There are only few vibronic states between S_0 and S_1, making the electron stay for a longer time in this state (on the order of ns). It can decay by photoluminescence, be transferred to another molecule (B), or convert to a triplet state (T_1^A) by intersystem crossing. Triplet states are longer living, they can recombine by phosphorescence, thermal deactivation, or be transferred to another molecule (e.g. Molecule C) where they may further decay and recombine. The state S_1^A can be transferred by charge transfer or by energy transfer to another molecule (B). It can even be a state shared by A and B that can lead to excimer or exciplex emission.

in weakly coupled molecules on a time scale of about $\sim 10^{-9}$ s and will be further discussed in section 1.1.4 regarding transport.

Figure 1.6 shows the most important optoelectronic transitions after Horie et al [47]. This is a simplified picture, in organic molecules many of those states are relaxed due to redistribution of the electronic cloud and structural deformation. The absorption of a photon will create a bound electron-hole state called exciton, which will be discussed in the following section.

1.1.3 Excitons

An exciton is a bound pair of a hole and an electron. This bound state has lower energy than the unbound state. Its electrical charge is zero and it has integer spin.

There are two known limits. The Mott-Wannier exciton is delocalized over several lattice units in materials with large dielectric constant. If the exciton is strongly localized in one unitary cell or in

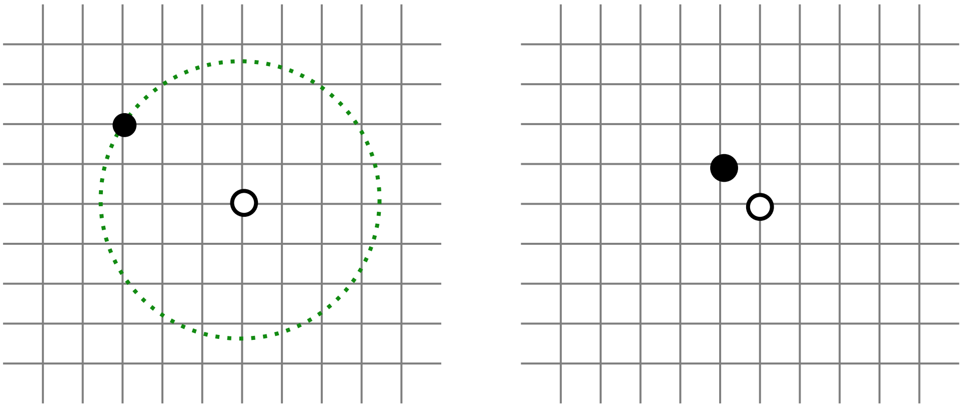

Figure 1.7: The scheme on the left side represents a Mott-Wannier exciton, and the scheme on the right side represents a Frenkel type exciton. The grid represents a crystal lattice, the full circles an electron and the open circles a hole. The dotted circle is used to show that the Mott-Wannier exciton is highly delocalized.

one molecule, it is called Frenkel exciton. The Frenkel exciton can also be composed of a charge transfer (C-T) exciton. This bound state has a lower energy than the particles (e-h) without spin correlation. The correlation can be with parallel spin (singlet excitons) or anti-parallel spin (triplet excitons). An illustrative picture to differentiate a CT exciton from an e-h pair are adjacent charged donor-acceptor (D^+A^-) molecules that need to gain vibrational energy (phonon) to release that charge. [50]. For the CT exciton, one can write [50]:

$$E_{EX} = IP_D - E_A + \Delta_C + P - \vec{\mu_\sigma}\vec{\mathrm{F}} \tag{1.8}$$

where E_{EX} is the vertical excitation energy, IP_D ionization potential of the donor, E_a is the electron affinity of the acceptor, Δ_C is the Coulomb interaction between adjacent ions (D^+A^-), P is the lattice polarization energy, $\vec{\mu_\sigma}$ the static dipole moment of the excited state (D^+A^-), and $\vec{\mathrm{F}}$ is the applied field.

Mott-Wannier excitons normally occur in covalent solids where the charges are strongly delocalized. Frenkel type excitons are more easily detected in ionic crystals like NaCl. Charge transfer excitons are typical for Van der Waals solids as in organic donor-acceptor blends.

Exciton formation

In a molecule, an exciton can be formed directly by absorbing a photon, or by the encounter of positive and negative charge carriers on the same or neighboring molecules. The deactivation to the ground state can be avoided if there is no spatial overlap of the wave functions if, for example, an excited state

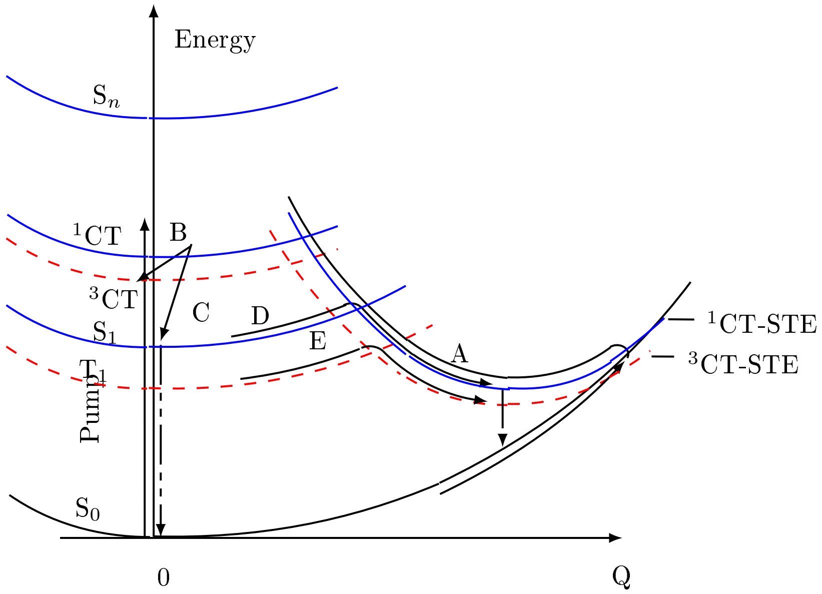

Figure 1.8: Energy versus configurational space showing the relaxation pathways in solid C_{60}, adapted from [51]. S are the singlet exciton states, T_1 is the lowest triplet exciton state, CT are the transfer-charge exciton states and CT-STE the self trapped exciton states. Triplet states are shown in red (dashed lines), singlet states are shown in blue (solid lines).

$S_1 + E^{(vib)}$ cannot relax to its fundamental electronic state j:

$$S_1 + E^{(vib)} \quad \not\rightarrow \quad S_1 \tag{1.9}$$

Figure 1.8 shows a proposed diagram of the energy levels in solid C_{60} with the possible pathways for relaxation of an excited state [51]. In case of C_{60}, photoexcitation directly creates charge-transfer (CT) singlet exciton. It relaxes to its self trapped exciton (STE) and further relax to the ground state in approximately $1.3 \cdot 10^{-12}$ s. Triplet excitons ^{3}CT are created by intersystem crossing from singlet excitons ^{1}CT. Their formation rate (path B) is very low due to the very fast relaxation trough pathway A. The rest of the singlet excitations relax into the singlet excitons S_1. Singlet self trapped CT excitons have a short lifetime (10^{-9} s) compared to triplet CT-STE (10^{-2} s). They can decay radiatively to the ground state, decay non-radiatively to the ground state via a thermally activated process or decay to a triplet CT-STE via ISC.

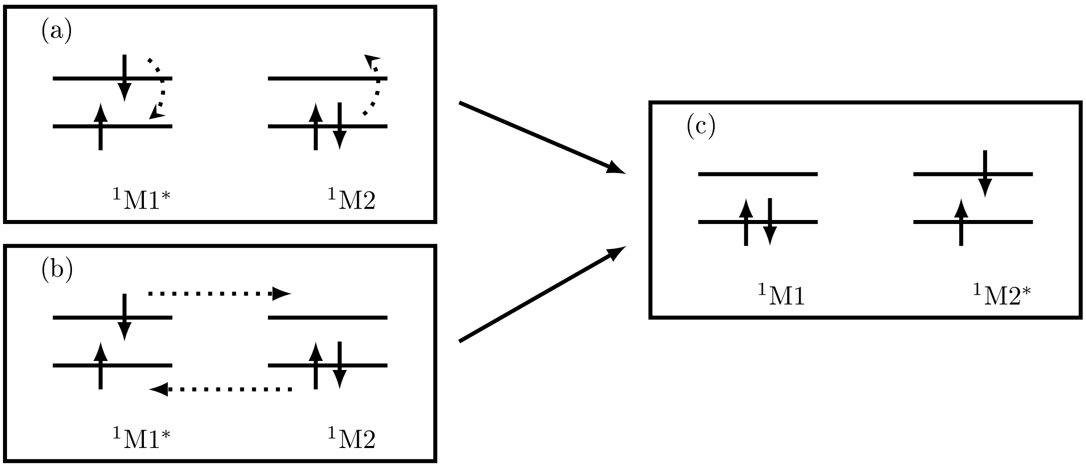

Figure 1.9: Schematic showing the Förster (a) and the Dexter (b) energy transfer mechanism in singlet states from molecule D to molecule A. (c) is the final state, with D in its ground configuration and a singlet exciton in A. (Adapted from [52])

Exciton diffusion

Exciton transfer between two molecules is a non-radiative transfer. For singlet excitons it can be dipole-dipole transfer, also known as Förster transfer. The exchange interaction or Dexter transfer is also allowed for triplet excitons. Figure 1.9 illustrates the two mechanism for singlet state. During the Förster energy transfer one excited state goes back to its ground state and another molecule gets excited in resonance. The Förster mechanism is a short range, non radiative transfer and requires the conservation of the spin of exciton donor and exciton acceptor individually. For practical purposes, the transfer is possible for distances between 1.5 nm and 10 nm. For shorter distances, the overlap of exciton donor and exciton acceptor sites favors their charge exchange and the total spin is conserved. Many theories of energy transfer are discussed by Powel et al in [53]. Migration of excitons in organic materials is typically treated as diffusion [53, 54], with a typical diffusion length of several nanometers [55].

Exciton separation

An exciton can be separated into electron and hole if the charge carriers have enough energy to overcome the excitonic binding energy. Inorganic semiconductors like crystalline Si have excitonic binding energies smaller than the thermal energy, and the photogenerated charges are created with sufficient kinetic energy to be free in their bands.

Organic semiconductors have a low dielectric constant, therefore, excitons in organic molecules usually have large binding energy and have a very low probability of being separated at room temperature.

However, they can be separated by an electric field [56]. An exciton can also be separated by a donor-acceptor heterojunction if the donor's exciton binding energy (ξ_{XD}) is lower or equal to LUMO$_A$ - LUMO$_D$. The condition for an exciton in the acceptor material be separated by a donor-acceptor heterojunction is: $\xi_{XA} <$ HOMO$_A$ - HOMO$_D$. Depending on the energy levels of the excitonic band in a heterojunction, an excitonic transfer from one material to another with a lower excitonic band-gap may take place instead of charge separation [57].

1.1.4 Charge carrier transport

It was stated before that the organic molecules are held together by the weak inter-molecular Van der Waal force. An important implication of the weak interactions between molecules is that a charge on the molecule forces a nuclear rearrangement of the molecule and its nearest neighbors, forming a so called polaron [58, 59], instead of distributing the charge over the lattice. Polarons also exists in polymers and they can be localized by chemically interrupting the conjugation as in co-polymers [60, 61].

Charge carrier mobility

This high localization of the charges causes a relatively low mobility of the charge carriers. The mobility and diffusion coefficient are related by the Einstein relation [62]. Consequently, the diffusion coefficient is also low. The Einstein relation in its original form is valid at low charge carrier concentration and room temperature [56, 63]. Typical room temperature mobility values are in the range 10^{-10} to 1 cm$^2/Vs$ for holes and for electrons. In many materials, the mobility for electrons is measured to be many orders of magnitude lower than for holes, this is also attributed to impurities that usually act as acceptor and trap for negative charge carriers [64].

Variable range hopping successfully explains the transport in many organic compounds. Hopping is a thermally activated process. It may take place without any change in energy, in a two step process, according to Simon [65]:

$$A^-A \rightleftharpoons [A^-A] \overset{k_{ET}}{\rightleftharpoons} [AA^-] \rightleftharpoons AA^- \tag{1.10}$$

Here, k_{ET} is the electron transfer rate. The species [ ] are thermally activated by an energy δE_a. One can define a hopping frequency (ν_h) that is directly related to the molecular structure and the position between two adjacent molecules. It can be written as function of the resonance integral (γ), the atomic integral (β) and the overlap between the π orbitals of adjacent molecules (α) [66]:

$$\nu_h = \frac{2}{h}\frac{|\gamma - \alpha\beta|}{1 - \alpha^2} \tag{1.11}$$

The thermally activated hopping probability (P_h) becomes:

$$P_h = \nu_h exp\left(- \frac{\Delta E_{ac}}{kT}\right) \tag{1.12}$$

The expression for the mobility follows from substituting the diffusion coefficient (with $D_h = P_h a_c^2$, a_c being the lattice constant) in the Einstein relation.

$$\mu = \frac{ea_c^2}{kT}\nu_h exp\left(- \frac{\Delta E_a}{kT}\right) \tag{1.13}$$

The energy barrier between two hopping sites can be deformed by applying a high external electric field in a similar way to the Schottky effect [67–70], this will increase the mobility as follows:

$$\mu = \mu(0) exp\left(\frac{q}{kT}\beta\sqrt{F}\right) \tag{1.14}$$

Transport equations

A simple drift-diffusion model can be used to describe the unipolar transport in a single layer:

$$J_n = \mu_n n q \mathrm{F} + \mathrm{qDn}\frac{\mathrm{dn}}{\mathrm{dx}} \tag{1.15}$$

The ohmic transport (expressed by the first term of equation 1.15) is valid only for small fields and constant temperature. The μ is field dependent and also temperature dependent. If a current is passing through an organic semiconductor layer, and the mobility is very small, the material will be charged at high fields, i.e. more charge will be injected than the material can transport. The limit is expressed by the Child's [71] law J$\propto$ V^2 [72]:

$$\mathrm{J_{SCLC}} = \frac{9}{8}\mu_\mathrm{n}\epsilon\epsilon_0\frac{\mathrm{V}^2}{\mathrm{d}^3} \tag{1.16}$$

The modeling of the space charge limited current can be further improved taking into consideration the distribution of trap states [73]. The transport theories for disordered media emphasizes the importance of the charge carrier mobility. Organic semiconducting materials are usually classified using the order of magnitude of its majority charge carrier mobility. Many different techniques were developed to measure the mobility, time of flight (TOF) of an optically generated pulse of charge is used in [74, 75]. Charge extraction by linearly increasing voltage (CELIV) can be applied directly on devices [76]. Statical measurements of mobility can be performed using the drift current equation on electrochemical contacts [77]. The mobility can also be determined from FET [78–80], SCLC [81, 82], and injection limited current [83] measurements. Other methods are Hall [84], Seebeck [85], holographic TOF [86], electrical impedance [87], microwave conductivity [88], transient of electroluminescence [89], absorption transient [90, 91], and electric pulse [92, 93].

The most direct measurement of the mobility is TOF, however it requires thick layers and a material with a high absorption coefficient to confine the charge generation to a very narrow region and measure its drift due to an applied bias. The method is useful for material characterization but is not a good parameter for real applications due to the necessity of very thick layers and high electric fields. SCLC mobility is used to measure a field independent mobility in the range of fields that exists in OLEDs and organic solar cells. A field dependent theory for SCLC can be used when the I *vs.*V curves do not exactly follow Child's law, and ohmic contacts are still given [94]. Seebeck is very convenient if one has doped layers and consequently it is difficult to reach SCLC condition.

In the Seebeck measurement, a layer of the semiconductor material is deposited over a planar substrate. A temperature gradient is applied in the direction of the layer surface. A voltage (thermovoltage) is measured on the same direction as the temperature gradient [95]. The Seebeck coefficient ($\mathrm{S}_{\mathrm{Seebeck}}$) is defined as a function of the thermovoltage (V_{12}), the absolute temperature (T), and the temperature difference (ΔT):

$$\mathrm{S}_{\mathrm{Seebeck}}(\mathrm{T}) = \lim_{\Delta\mathrm{T}\to 0}\frac{\mathrm{V}_{12}(\mathrm{T},\Delta\mathrm{T})}{\Delta\mathrm{T}} \tag{1.17}$$

For unipolar charge carriers and one transport level the Seebeck coefficient is related to the Fermi level (ξ), the transport level (E_σ), and the absolute temperature as follows [96]:

$$\mathrm{S}_{\mathrm{Seebeck}}(\mathrm{T}) = \frac{\xi(\mathrm{T}) - \mathrm{E}_\sigma}{\mathrm{qT}} \tag{1.18}$$

where q is the charge. The equation above can be easily associated with the Fermi distribution, here using the Maxwell-Boltzmann approximation, since $|\xi - \mathrm{E}_\sigma| \gg \mathrm{k_B T}$:

$$n_h = \mathrm{n}_\mu \mathrm{exp}\left(\xi(\mathrm{T}) - \frac{\mathrm{E}_\sigma}{\mathrm{k_B T}}\right) = \mathrm{n}_\mu \mathrm{exp}\left(-\mathrm{q}\frac{\mathrm{S_{Seebeck}}}{\mathrm{k_B}}\right) \tag{1.19}$$

where n_h is the density of holes, n_μ is the effective density of states, and $\mathrm{k_B}$ is the Boltzmann constant. The Seebeck mobility (μ_S) is obtained from the conductivity equation:

$$\sigma = \mathrm{qn_h}\mu_\mathrm{S} \tag{1.20}$$

It is of great importance to know the charge carrier mobility of the organic materials because the mobility is one important limiting factor of performance in devices such as field effect transistors (in the high frequency regime) and especially organic solar cells.

Metal - semiconductor interface

Metal-semiconductor interfaces usually have a large energetic barrier. Charges can tunnel through it or jump over it if they have enough energy. The barrier can be lowered by an external electric field (see dashed red line in figure 1.10). The barrier can be further lowered by a Schottky effect, where a charge at the distance x from the interface induces a mirror charge with opposite sign at distance $-x$ from the interface. This reduction is depicted in figure 1.10. If the barrier is low enough and the charge carriers have sufficient thermal energy, the transport can be described as limited by thermionic injection [97]. For low mobility semiconductors, the Richardson-Schottky equation must be modified to include diffusion [98]:

$$\mathrm{J} = \frac{4\pi\mathrm{em(kT)}^2}{\mathrm{h}^3}\mathrm{exp}\left(-\frac{\phi_\mathrm{Bn}}{\mathrm{kT}}\right)\mathrm{exp}\left[\left(\frac{\mathrm{q}^3}{4\pi\epsilon_0\epsilon_\mathrm{r}}\mathrm{F}\right)^{1/2}/\mathrm{k_B T}\right] \tag{1.21}$$

The first exponential describes the static barrier seen by the charge carrier, the barrier height is ϕ_{Bn}. The second exponential describes the lowering of the barrier by an applied electric field (F). Here, m, ϵ_0, ϵ_r, are, respectively, the free electron mass, the permittivity of vacuum, and the optical dielectric constant.

If the temperature is low, the charge carriers may not have enough energy to overcome the barrier. For high applied fields, the shape of the barrier is distorted in a way to increase tunneling

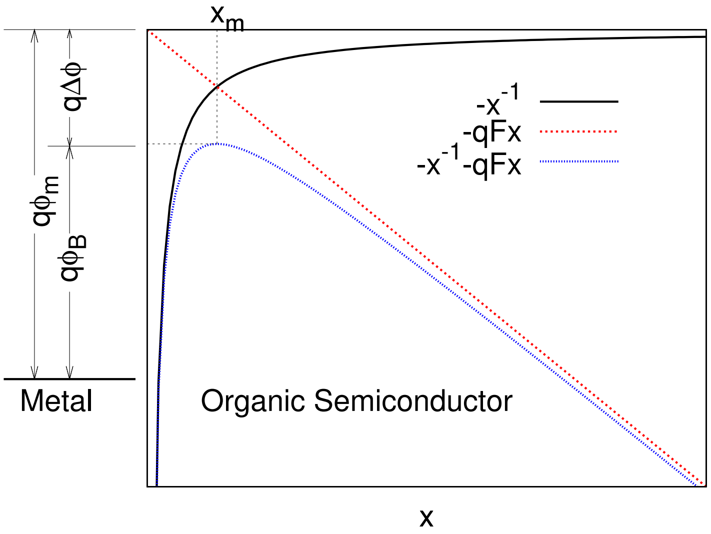

Figure 1.10: Energy interface between metal and semiconductor. The Schottky barrier (Blue) is composed by the barrier itself (red) minus the lowering caused by the image force (black).

probability. Under these conditions the tunneling current becomes dominant. The energy barrier under high fields through a triangular barrier is given by the Fowler-Nordheim expression [99]. A correction for the triangular shape was developed by Koehler et al [100] taking into consideration the Fermi distribution in the semiconductor. The equation then becomes:

$$j_{FNK}(T) = \frac{q^2 \mathrm{k_B} T \pi}{h} \left(\frac{m^*}{2\phi} \right)^{1/2} \mathrm{Fexp}\left[- \frac{4(2\mathrm{m}^*)^{1/2}\phi^{3/2}}{3\mathrm{Fq}\hbar} \right] \frac{1}{\sin[\beta \mathrm{k_B T}\pi]} \tag{1.22}$$

Here, ϕ is the barrier height, m^* is the charge carrier effective mass, h the Planck constant, $\mathrm{k_B}$ is the Boltzmann constant, T the absolute temperature, and $\beta = (2(2m^*)^{1/2}\phi^{1/2})/(Fq\hbar)$.

For materials with very low mobility, the space charge can extend to the entire region, from the position where the charges tunnel into the organic semiconductor, up to the opposite electrode, so that the current becomes mobility dependent (see Gepperd et al [101, 102]).

The picture described until now considers ideal metal-semiconductor interfaces and can, to some extent, be applied to organic semiconductors. If there are surface states on the semiconductors surface, they will be filled up to E_F; and if the surface DOS is large enough, it will screen the field over it. The barrier height will be independent from the metal work function and be only determined by the surface of the semiconductor [103].

A method to influence the barrier and provide ohmic contacts between an organic semiconductor and a metal is to change the Fermi level on the semiconductor. This can be accomplished with doping.

Doping of organic materials

Kearns did report an increased conductivity in phthalocyanine doped with ortho-chloranile in 1960 [104]. The first study about electrical doping of organic materials was probably done in 1963 by Bolto et al [105]. Further experiments about intentional doping of small molecules were reported around 1980 [106–108]. It is also worth to mention the work of Shirakawa et al in 1976 with the doping of polyacetylene [109, 110]. Other polymers are doped with ions supplied by inorganic salts, organic salts, acids, and even polymeric acids. The doping is usually performed in solution or by an electrochemical red-ox process [111]. Most common examples are polyaniline doped with camphorsulfonic acid or poly(3,4-ethylenedioxythiophene) (PEDOT) doped with poly(styrenesuflonic) acid.

The doping process is a partial or complete charge transfer from a dopant to a semiconductor material (matrix or host), such that the host becomes charged positively of negatively. In organic small molecules, the charge transfer for p-doping is an electron transfer from the matrix HOMO to a dopant LUMO. The transfer can be effective if the HOMO of the matrix is higher or at a similar energy level to the electron affinity of the dopant, in this relation, the dopant is a strong acceptor and the matrix is composed of strong donor material. In a complementary way, to create charge carriers in the conduction band, the dopant has to have an ionization potential with a similar or higher energy level than the electron affinity of the matrix. This charge transfer has to occur without creating a covalent bond between dopant and matrix.

In this simple picture, a doped molecule is equivalent to its ionic form. The doping can be detected by spectroscopic methods, such as photoelectron spectroscopy (XPS) or infra-red spectrometry, or also in the visible, since the anionic molecules have different absorption spectra compared to the neutral forms [2].

Phthalocyanines are the model molecules used to study the doping of organic semiconductors [104, 106, 112]. Pfeiffer et al investigated the controlled doping of phthalocyanines [85]. Using Seebeck measurements, they found a positive Seebeck coefficient that decreases with increasing doping concentration. The Seebeck coefficient (s) is positive for p-type transport. Knowing the transport level (E_σ), they determined the position of the Fermi Level (ξ), concluding that, similarly to the inorganic crystals, the Fermi level shifts towards the valence level on increasing doping concentration.

---

[2] The electrical doping process implies in a charge transfer but does not constitute a chemical reaction between dopant and semiconductor matrix.

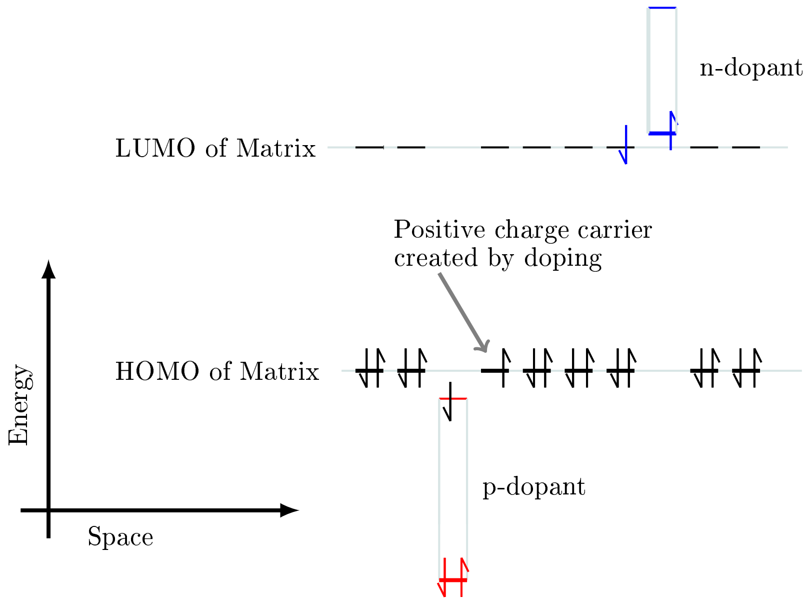

Figure 1.11: Schematic of the red-ox doping of organic semiconductors. The p-dopant (in red) is an acceptor molecule that, on doping, will be ionized receiving an electron from the HOMO of the matrix. The matrix will then have a free positive charge carrier (hole). The n-doping is performed in a correspondent way, where the n-dopant (blue) is a donor for the matrix. In this case, the electron is transferred to the LUMO of the matrix, where it is a negative charge carrier (electron).

There is, however, a big difference to conventional doping of inorganic semiconductors: the mobility rises supra-linearly with the doping concentration. In conventional semiconductors, the density of free charge carriers is, at best, proportional to the concentration of dopants. In organic semiconductors, the dopants also create charge carriers that will populate the deepest traps in the matrix before they populate the available free states. The filled level will define the mobility edge in the semiconductor. The explanation for the supra-linear increase in the mobility is that the distribution of the density of states has an exponential like tail. In devices, the dopants are used in transport layers to improve their conductivity, the doped layers are preferentially wide gap (so called window materials) so that light is only absorbed in the photoactive areas. The doped layers produce a space charge that forms a ohmic contact to the electrodes. In addition, or as alternative solution, the injection and extraction of charge carriers can be improved by using a neat dopant layer between the electrode and the transport layer.

Currently, p- and n-type doping of organic semiconductors is a well established procedure in small molecules as well as in polymers [113]. For p-doping, strong organic acceptors like F_4-TCNQ (2,3,5,6 -Tetrafluoro -7,7,8,8- tetracyanoquinodimethane) [85], HATNA (Hexaazatrinaphthylene), F_2-HCNQ (3,6-difluoro-2,5,7,7,8,8-hexacyanoquinodimethane) [114], and industrial NDP2 (Novaled AG) [27] are used.

On heavily doped contacts, as is the case for F_4-TCNQ 2% doped Zinc Phthalocyanine (zinc phthalocyanine), [115] the alignment of the Fermi level of the semiconductor with the metal creates a very narrow depletion layer. This thin barrier enables the efficient injection by tunneling.

The implementation of n-type doping is more complex because the dopants are easily oxidized by atmospheric oxygen. Therefore the dopants need to be synthesized and stored in inert atmosphere. Another option is to use precursors, for example compounds containing alkaline metals. In this case, the dopants are released during the doping process from thermal evaporation sources containing metal salts or metal-organic compounds, which are stable in air. However, organic semiconducting layers doped with metal ions may have unstable electrical properties, since the ions are small and may diffuse. Organic donors for n-type doping found in the literature are Liq (8-hydroxy-quinolinato lithium) [116], Pyronin B [117], AOB (3,6-bis (dimethylamino) acridine), and [118], LCV (4,4',4"- methylidynestris (N,N-dimethylaniline)) [119], cobaltocene (bis(cyclopentadienyl)cobalt(II)) [120]. An industrial strong organic n-dopant is NDN-1 (Novaled AG).

1.2 Organic solar cells

1.2.1 Comparison between inorganic and organic solar cells

There are some similarities between organic and inorganic solar cells. In this section, we will focus on the different microscopic aspects of the photoelectric conversion and adapt the physics of inorganic semiconductors to explain the macroscopic behavior of organic solar cells.

In a simple picture, a solar cell[3] is a device that absorbs light, converts it into electricity and charge itself. The charges generate the potential to drive an electrical current. Under reverse bias (i.e. applying a bias that is in opposite direction to the internal charge) one can extract all the photogenerated charges. This current (the saturation current) is proportional to the incident light intensity (within a defined light spectrum); more precisely, it is proportional to the number of absorbed photons. In good solar cells, the maximum photocurrent one can get out of the device, the reverse bias saturation current, is almost equal to the short circuit current I_{SC}.

The quantum efficiency of the photoelectric conversion is calculated by dividing the generated photoelectric current (I_{SC}) by the incident photon flux The basic energy diagram of an inorganic solar cell is a p-n junction, as depicted in figure 1.12. The different type of doping on the left (n-doped) and right (p-doped) implies a difference in the Fermi level. The p and n side have their Fermi level shifted,

---

[3] also known as solar battery or photovoltaic device

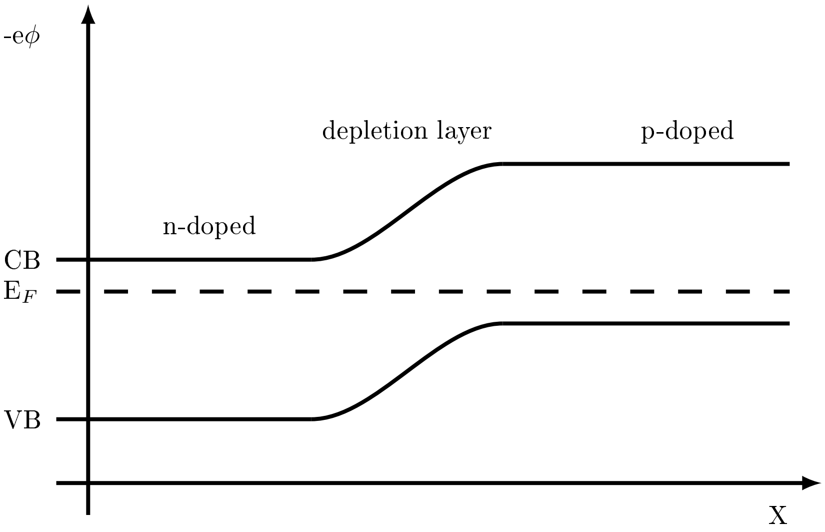

Figure 1.12: Energy diagram of a p-n junction. The left side is n-type doped and the right side p-type. The Fermi energy is aligned in equilibrium.

downwards on the p side and upwards on the n side. The charges generated by the doping compensate each other forming a neutral (depletion) zone. The difference in the Fermi level is responsible for the separation of the photogenerated charges.

If this p-n junction is illuminated, photons are absorbed creating pairs of holes and electrons. In silicon, the electrons and holes have sufficient kinetic energy to be separated (no correlation between their wave functions). The free charges will follow the electric potential until the Fermi level align. If the contacts (p and n) are shorted by ohmic contacts, then the device will discharge, and generate a constant current if continuously illuminated.

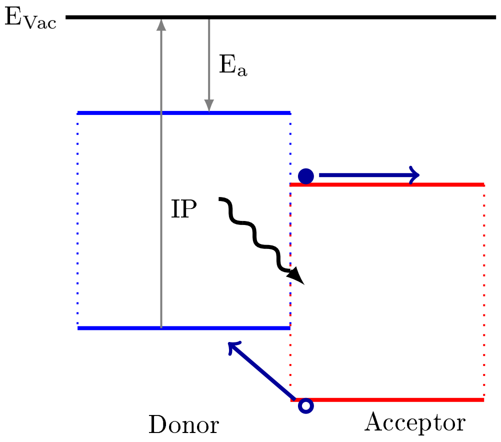

Figure 1.13: Simplified energy diagram of a donor acceptor heterojunction. IP *is the ionization potential and* $\mathrm{E_a}$ *the electron affinity of the semiconductor.* $\mathrm{E_{Vac}}$ *is the vacuum energy level.*

Contrary to inorganic semiconductors, only excitons and not free charge carriers are created in organic semiconductors by absorption of a photon (see sec. 1.1.3). Organic p-n junctions made of the same material (homojunctions) do not work efficiently as solar cells [56]. This is due to the fact that upon absorption of photons, Frenkel excitons with a high binding energy are created in the organic semiconductor. The excitons can be separated using a heterojunction formed by two type of materials, one being an electron acceptor and the other an electron donor (in relation to each other). A simple picture of an organic solar cell can be seen in figure 1.13. A photon is absorbed near the donor-acceptor interface creating an exciton. The exciton can be separated at the interface, and the separated charges can be transported by drift-diffusion to the contacts.

1.2.2 Types of organic solar cells

Organic semiconductors are direct band gap absorbers and can be easily tuned to emit or absorb a desired wavelength. As discussed in section 1.1.3, contrary to covalent crystals like Si and III-V semiconductors, the absorption directly generates an exciton.

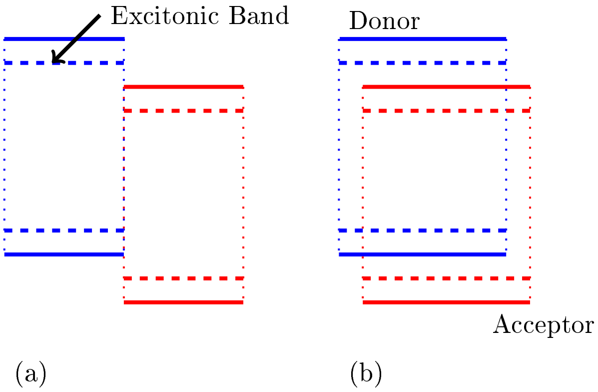

Figure 1.14: Basic solar cell structures involving organic layers. (a) simple flat junction between a donor and an acceptor layer, or Tang's cell. (b) Bulk D-A heterojunction.

Figure 1.14 shows a simplified energy diagram of the main types of solar cells involving organic molecules. (a) is the flat junction between a donor material (D) and an acceptor material (A). This junction is called flat D-A heterojunction or simply flat heterojunction (FHJ). In this device, one or both materials (donor and acceptor) can convert photons into excitons. If the excitons reach the D-A interface they will dissociate, at the same time the D (A) layer will serve as transport layer for holes (electrons). Each layer at the FHJ also has the function of a blocking layer for the opposite charge carrier type. (b) depicts a simplified diagram of a Bulk D-A Heterojunction (BHJ). Here, the exciton separation into charge carriers will occur in the bulk because the interface between D and A is drastically increased as compared to the FHJ. The transport of electrons and holes occurs on the LUMO of the acceptor and on the HOMO of the donor, respectively.

There are several approaches for high efficiency organic solar cells. It has to be taken into consideration that the charge carrier mobility is very low in organic semiconductors. This is partially compensated by the very high absorption coefficients (e.g., the extinction coefficient (ε) of Zinc Phthalocyanine is $\propto 10^5 M^{-1} cm^{-1}$) that enables the use of very thin active layers. Nevertheless, the excitonic diffusion length is not very large, limiting the maximum distance between absorption center and dissociation interface between $\sim$ 5 nm and $\sim$ 40 nm [121]. One approach to use thicker layers is to make a donor-acceptor blend in form of a BHJ solar cell [122]. In the BHJ, the distance that an exciton has to pass until it encounters a D-A interface is smaller. The transport of charge carriers will occur int the transport paths that exist in a non-homogeneous structure. A simple picture describing the morphology of the active layer of a small molecule BHJ solar cells is a blend formed by two types of clusters. This concept also works well in some polymer or hybrid devices such as polymer+PCBM blend cells [123]. Another approach is to make the absorption layer only a few monolayers thick. In this extreme case, such as in dye sensitized solar cells (DSSC), the absorption is caused by a very large surface area of a porous TiO_2 layer covered by an organic dye and immersed into an ionic conductor (which can also be solid state semiconductor [124]).

This work focuses on solar cells with small molecules. BHJ have higher I_{SC} compared to FHJ due to increased excitonic separation. A drawback is the lower availability of energetically favorable percolation paths used to transport the charge carriers to the electrodes, increasing the bimolecular recombination rate and consequently decreasing the performance. The limitation on the layer thickness to get the highest efficiency can be overcome by making tandem solar cells, which can be thin as required and separated by transparent wide gap transport materials. High efficiency solar cells with small molecules usually have a complex layer structure [16] (see fig 1.15).

1.2.3 Transfer curve (I *vs.*V)

The electrical transfer curve (I *vs.*V curve) of an organic solar cell can be used to extract performance information. Without illumination, it resembles a diode curve. Under illumination, a photocurrent that flows against the applied field is added to the curve. This addition is only linear in a first approximation.

Figure 1.16 shows a I *vs.*V curve from a typical organic solar cell. Some characteristic points are

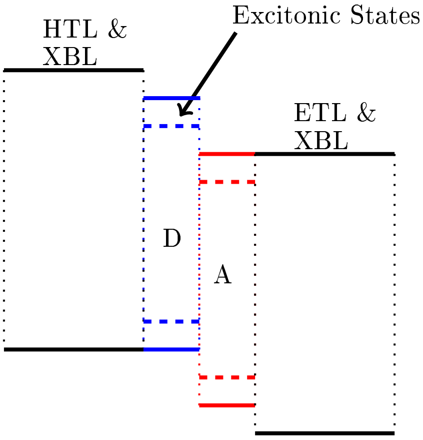

Figure 1.15: Flat heterojunction solar cell with exciton blocking layers (XBL) that are also wide gap hole (HTL) and electron transport layers (ETL) on the right side.

used to describe its normal behavior. These points are the open circuit voltage ($\mathrm{V_{OC}}$), the short circuit current ($\mathrm{I_{SC}}$), the maximum power point (MPP), and the fill factor (FF).

The maximum power point is defined as the point where the power, the product $-\mathrm{V} \times \mathrm{I}$ is at a maximum in the fourth quadrant. This point has the coordinates ($\mathrm{V_{MPP}}$, $\mathrm{I_{MPP}}$).

The fill factor is defined as the ratio between the maximum power and the product $\mathrm{V_{OC}} \times \mathrm{I_{SC}}$. It defines the ratio (also represented as a percentage) of the useful power in relation to the limitation given by $\mathrm{V_{OC}}$ and $\mathrm{I_{SC}}$ (area of small rectangle divided by area of the larger rectangle in 1.16):

$$\mathrm{FF} = \frac{\mathrm{V_{MPP}I_{MPP}}}{\mathrm{V_{OC}I_{SC}}} \tag{1.23}$$

Furthermore, the reverse saturation ratio (S) is defined as the ratio between the short circuit current and the light current at -1 V ($\mathrm{I_L}$) subtracted from the dark current at -1 V ($\mathrm{I_D}$):

$$S = \frac{\mathrm{I_{SC}}}{\mathrm{I_L}(-1) - \mathrm{I_D}(-1)} \tag{1.24}$$

A set of coupled equations must be numerically solved for a complete modeling of a solar cell's I *vs.*V curve [125, 126]. In essence, the continuity equations (Eq. 1.25), the Poisson equations (Eq. 1.26) and the drift-diffusion transport equations (Eq. 1.15) must be solved, taking into account the boundary conditions [127]:

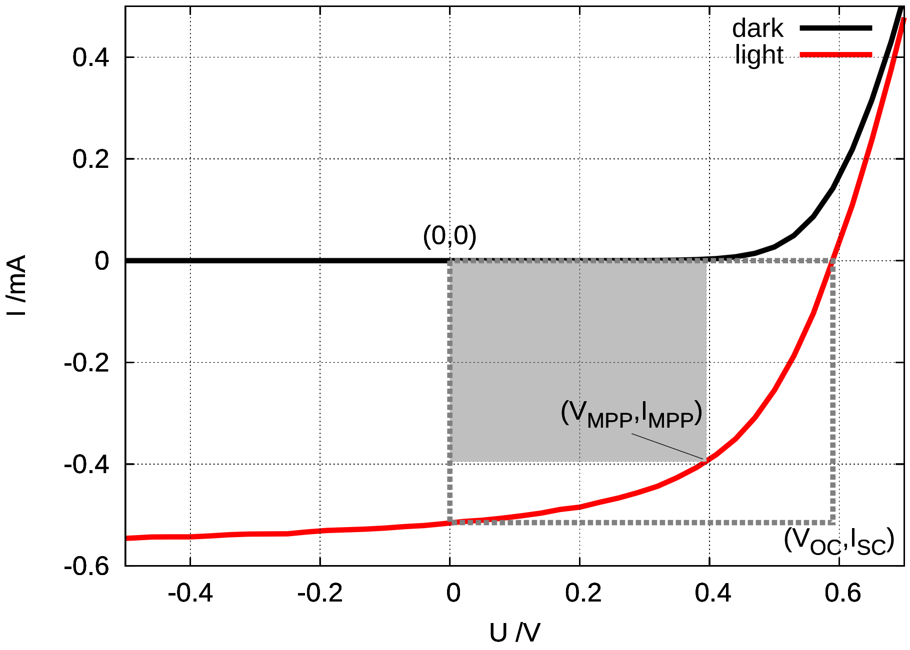

Figure 1.16: Typical I *vs.*V *curve of an organic solar cell in dark (black) and under simulated AM1.5 illumination (red). The characteristic parameters are shown* $\mathrm{V_{OC}}$*,* $\mathrm{I_{SC}}$*, and* MPP *(*MPP = *(*V_{MPP}*,*I_{MPP}*)).*

$$\frac{\partial n,p}{\partial t} = G - R\frac{1}{q}\frac{\partial J_{n,p}}{\partial x} \tag{1.25}$$

$$\Phi(x) = -\int_0^x \mathrm{Fdx} \tag{1.26}$$

The gradient of the field is calculated using the electron and hole densities (n and p), the respective trap density (N_{nT}, and N_{pT}), and the density of donors (N_D) and acceptors (N_A).

$$\frac{\partial \mathrm{F}}{\partial x} = \frac{e}{\epsilon_0\epsilon_r}(p - n + N_D - N_A + N_{pT} - N_{nT}) \tag{1.27}$$

In Eq. 1.25, G is the generation rate, q the elementary charge, and R is the recombination rate. The recombination (R) is given by the bimolecular (Langevin) recombination model [126], or by the geminate (Onsager) recombination model [128, 129].

The opto-electric transfer curve (I *vs.*V curve under illumination) can be simulated with this basic set of equations. The simulation needs as input the incident light spectra to determine the exciton generation profile. In general, the simulation can give results with good agreement to experiment, however the large set of free parameters leads to many possible solutions for the same I *vs.*V curve. Some of the parameters have a large influence on the result and some can only be easily accessed experimentally in specially constructed devices that are not solar cells (for example, the charge carrier mobility). In view of this, the results of this work will be discussed focusing more on the physical effects and less on the quantitative values.

Photocurrent and Saturation current

The photocurrent is in a first approximation linearly dependent on the light intensity. Under very high light intensities, the absorber molecules may be saturated either with excitons or with charges. Effects such as exciton-exciton recombination may also take place. A reverse applied electric field on a solar cell will assist the extraction of charges and eventually the separation of excitons. The best approximation for the photocurrent is the saturation current (I(−1V)). In good solar cells, the photocurrent can also be roughly approximated to $\mathrm{I_{SC}}$, which means that almost all generated charges can be transported out of the device under short circuit. In such a device, the charge separation is easily achieved and is almost independent from the external applied bias. In an equivalent circuit picture, this implies in a very high shunt resistance.

In flat heterojunctions, it is reasonable to assume that exciton recombination (R_X) takes place since the excitons need to travel a relatively long distance compared to their diffusion length before they reach the interface where they can be separated. The exciton recombination is the main recombination loss in flat heterojunctions solar cells [81]. It can be classified in geminate recombination (R_G) and bimolecular recombination. On the other hand, due to the well defined D-A interface, the electron-hole (R_{e-h}) recombination, or also the exciplex recombination, is strongly reduced at short-circuit condition and can therefore be neglected. According to Pope [81], the excitons have a high initial recombination rate due to the strong Coulomb attraction between the e-h pair.

In bulk heterojunctions, R_G can be neglected since the dissociation is very fast; in this case, the bimolecular recombination is dominant [130]. The mobility of the slowest charge carrier and the density of traps strongly influences the bimolecular recombination rate [130].

In homojunction organic solar cells, both processes take place and the photocurrent can only be efficiently extracted at high reverse fields.

R_G is a function of the free electron density (n), the free hole density (p), the intrinsic electron (n_{int}) and hole (p_{int}) densities, and the Langevin recombination factor [130].

$$R = \gamma(np - n_{int}p_{int}) \tag{1.28}$$

where γ is given by:

$$\gamma = \frac{q}{\epsilon}(\mu_e + \mu_h) \tag{1.29}$$

Open circuit voltage

In a picture proposed by Peter Würfel, the internal or maximum open circuit voltage that a system can deliver is given by the difference of the quasi-Fermi levels from holes and electrons in the junction, at open circuit condition [131]. The position of the quasi-Fermi levels is calculated from the Fermi distribution (Boltzmann approximation):

$$n_e = N_C exp\left(- \frac{\mathrm{C_B} - \xi_\mathrm{e}}{kT}\right) \tag{1.30}$$

$$n_h = N_V exp\left(- \frac{\xi_h - \mathrm{V_B}}{kT}\right) \tag{1.31}$$

These equations are used to determine the density of electrons (n_e) and the density of holes (n_h). The density of electrons is calculated knowing the energy difference of the quasi-Fermi level for electrons (ξ_e) to the conduction band (C_B), the temperature (T), and density of states (N_C). In the same way the density of holes is calculated with the quasi-Fermi energy for holes (ξ_h), conduction band energy (V_B), the temperature (T), and density of states (N_V). Now, V_{OC} can be written as:

$$\mathrm{V_{OC}} \leq \xi_\mathrm{h} - \xi_\mathrm{h} = \mathrm{V_B} - \mathrm{C_B} - \mathrm{kT}\ \ln\left(- \frac{\mathrm{N_C N_V}}{\mathrm{n_e n_h}}\right) \tag{1.32}$$

This is the upper limit, it holds if it is granted that electrons can go only to one side, and holes to the other (semipermeable membranes, compare fig. 1.15 to fig. 1.17). The effect of the semipermeable membranes can be due to a transport energy level offset between two different materials, for example, in a heterojunction. For each charge carrier type, one material can have a more favorable energy level compared to the other material, which has a less favorable level or is even an energy barrier.

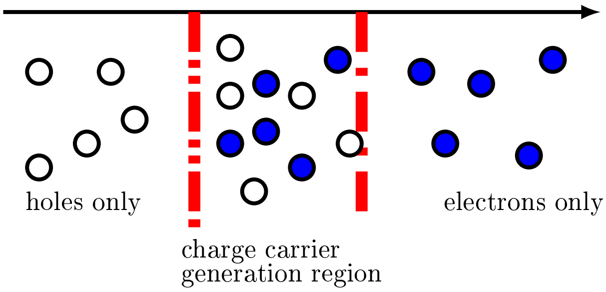

Figure 1.17: Organic solar cell in a semipermeable membrane picture: the generated charge carriers can only move out of the generation region in opposite directions.

If the anisotropy of the current is not granted by such semipermeable membranes, then V_{OC} can be lower and limited to the built in-voltage [132].

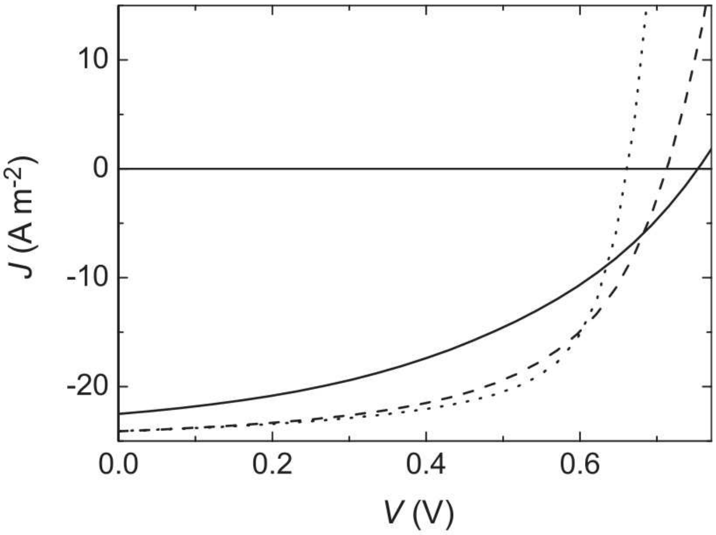

Figure 1.18: Simulated J vs. V curve (J is the current density) to fit measured data of a bulk heterojunction solar cell. The solid line is the result with $\mu_{h0} = 5.5 \times 10^{-10} m^2 V^{-1} s^{-1}$ *and* $\mu_{e0} = 3.7 \times 10^{-9} m^2 V^{-1} s^{-1}$*. The dashed line has the hole mobility increased to* $\mu_{h0} = 2.0 \times 10^{-8} m^2 V^{-1} s^{-1}$*. The dotted line is the simulation using the increased hole mobility and also an electron mobility increase to* $\mu_{e0} = 2.0 \times 10^{-7} m^2 V^{-1} s^{-1}$ *(adapted from [1]).*

Fill factor

The fill factor defines the ratio of the useful power related to the total internal power produced by the device. It is defined as the power at the maximum-power point (MPP) divided by the product $V_{OC} \times I_{SC}$. Simulating the I *vs.*V characteristics of a bulk heterojunction solar cell, one can show that there is a clear dependence of the fill factor on the recombination rate. The FF is smaller for devices with stronger recombination (larger Langevin recombination constant) [130, 133].

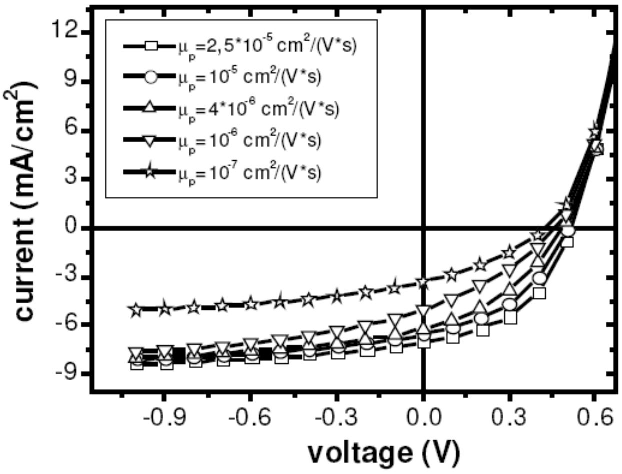

Figure 1.19: Simulated I *vs.*V *curves of bulk heterojunction devices for various hole mobilities, the electron mobility is fixed at* $5{\times}10^{-5}$ *cm*^{2}*/Vs (adapted from [2])*

Equivalent circuit

Solar cells are diodes and their dark I *vs.*V curve can be described by the Shockley equation [103]. A simple model is depicted in Fig. 1.20, the photocurrent is generated by a constant current source (I_L) in parallel with a diode (D1), a parallel resistance (R_{sh}^{int}), and in series with a resistance (R_S) [52, 134, 135].

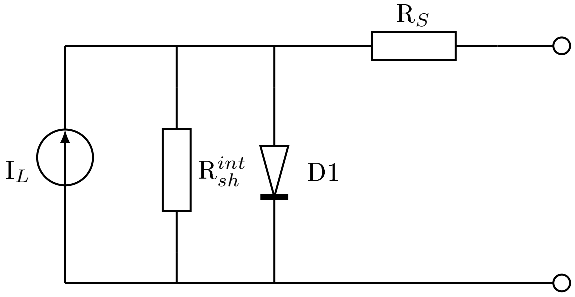

Figure 1.20: Equivalent circuit for a solar cell, showing a constant current source (I_L) *in parallel with a diode (D1), a parallel resistance* (R_{sh}^{int})*, and a series resistance* (R_S)*.*

The equation for a simple model with one diode in parallel with a constant current source and one resistance in series is given by Eq. 1.33.

$$\mathrm{I} = \mathrm{I_0}\left(\exp\left\{\frac{\mathrm{q(V - IR_s)}}{\mathrm{nkT}}\right\} - 1\right) - \mathrm{I_L} - \frac{\mathrm{V - R_sI}}{\mathrm{R_{sh}^{int}}} \tag{1.33}$$

By fitting with this equation one can obtain the series and parallel resistance of the devices. More details about the fitting procedure is given in section 2.4.

1.2.4 Absorption and responsivity

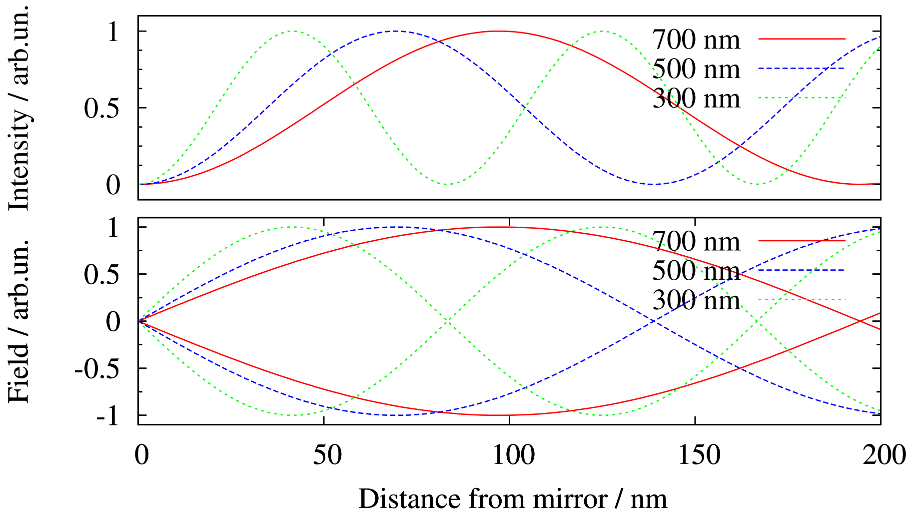

Figure 1.21: Representation of electric field and its intensity of light with 3 different wavelengths in a medium with $n = 1.8$ inciding from the left and being reflected at distance = 0 nm. Bottom: Standing waves with a node on 0 nm and wavelengths of 300 nm, 500 nm, and 700 nm represented by the electric field. Upper part: the corresponding intensity. The vertical units are arbitrary.

Organic optoelectronic devices are very thin, the active layers of the solar cell have a total thickness of about 100 nm. Optical interference effects have to be considered when designing the device; these effects become important due to the scale of the layer thicknesses, which are on the scale of the visible light wavelength. Figure 1.21 shows standing waves (electric field in the bottom part) caused by interference of light incident from the right and reflected by a mirror on the left. The corresponding irradiance of the wave ($\propto |\mathrm{F}|^2$) is shown by the upper part of the figure. The irradiance (or intensity) is defined as $I_{irr} = \epsilon \upsilon \langle \mathrm{F}^2 \rangle_\mathrm{T}$ (where ϵ is the permittivity, υ is the speed, and $\langle \mathrm{F}^2 \rangle_\mathrm{T}$ is the time average of the optical field) [136]. It is clear that different wavelengths have their maximum at different distances from the mirror.

The upper electrode (opposite to the substrate) of a conventional organic solar cell is metallic and therefore has a high reflectivity. The optically active layer responsible for light absorption is in between 100 nm of the distance to the reflecting electrode. The absorption profile can be directly related to the exciton generation rate, it is therefore of main importance to know the absorption profile in the active layers. If the absorption layer is thinner than 100 nm, the maximum of the light intensity cannot coincide with the position of the absorption layer for all wavelengths.

Different techniques can be used to obtain a large absorption over the spectrum. One solution is

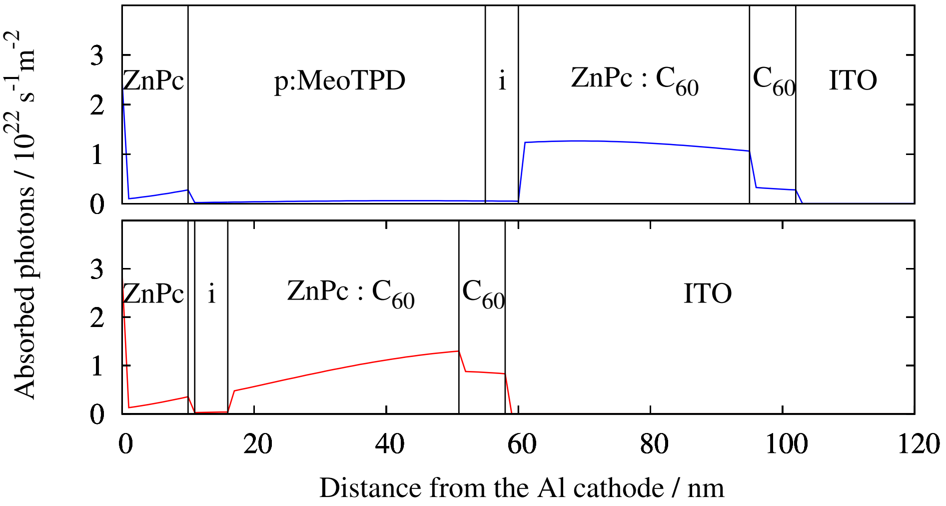

Figure 1.22: Distribution of the photon absorption in two m-i-p organic solar cells within the layer structure: Al (100 nm) / p:ZnPc (10 nm) / p:MeoTPD (x) / i:MeoTPD / ZnPc:C_{60} (2:1, 35 nm) / C_{60} (7 nm) / ITO (132 nm) / glass substrate. Sun spectra AM 1.5 is inciding from the left. Top: $x = 45$ nm; bottom: $x = 1$ nm.

to use an absorption layer which is at least 100 nm thick; this is the case for common polymer solar cells (for example in [123]). Small molecule solar cells can use double or triple absorption layers, where each single layer has a material which absorbs in a different spectral region. Another alternative is the use of tandem solar cells; each individual cell has its own absorption layer placed on a maximum of the light intensity, which is not necessarily the first maximum.

These approaches cannot be implemented in a straightforward manner. Thick layers may compromise the electrical properties of the device, tandem structures can be difficult to produce due to the large number of required layers, and double or triplet absorption layers require materials with the correct electrical and optical properties which are not always available.

The transmission, absorption, and field distribution in a device can be calculated using the transfer matrix method; knowing the optical constants n and k and the incident solar light spectrum [137, 138]. Any variation of the layer structure will cause a change in the light intensity distribution. Figure 1.22 shows the absorption profile of two organic solar cells which are identical except for one transparent hole transport layer (p:MeoTPD). The p:MeoTPD layer has a thickness of 45 nm in the upper device and 1 nm in the lower device. The different absorption profile leads to a lower integrated absorption in the photo-active layers (ZnPc:C_{60} / C_{60}) of the bottom device.

Optimizing a single junction solar cell to work in the first optical node results in a device where the short wavelength absorber is close to the reflective contact and the long wavelength absorber further away from it [139]. The absorbers are made as thick as their excitonic diffusion lengths and wide gap transport materials are used as optical spacers. The choice in material layer sequence is now limited. C_{60} is widely used as acceptor and absorbs around 450 nm; it is preferably placed close to the metallic electrode, and it is necessary to place a donor adjacent to it, which absorbs light in a complementary spectral region. This procedure can be applied to tandem solar cells. Optimized tandem ZnPc/ C_{60} p-i-n solar cells have power efficiencies as high as 3.8% [139].

1.3 Stability

The main challenges in organic solar cell research are currently efficiency and lifetime [16]. There are a number of reports showing that organic solar cells can be comparatively stable. For instance, some dye sensitized solar cells (DSSC) exhibited no visible degradation operating at 75 ºC over 7 000 h [140], or very small changes even after 13 000 h under 400 Wm^{-2} [141]. A polymer solar cell using proprietary materials showed only a minor I_{SC} degradation after 2000 h [142]. Still, a standard polythiophene / fullerene derivative cell had an efficiency drop of 80% after operating for 1 000 h [143]. Small molecule based solar cells offer greater structural flexibility over polymer and dye sensitized solar cells due to the easier deposition of multiple layers, but lifetime data for complete encapsulated devices are still rare. In 1987 Manabe et al produced a very stable solar cell based on small molecules [144], the cell even had an improvement on I_{SC} over more than 600 h. Wang et al compared different C_{60} / CuPc solar cells and showed that the devices live longer if C_{60} is far from the Al electrode, leading to a shelf lifetime to half of its initial efficiency of 950 h [145]. High efficiency tandem solar cells were shown to be very stable with less than 3% of decrease in power conversion efficiency over 1 000 h at 50 ºC [11].

A more detailed investigation of CuPc / C_{60} devices showed a very high thermal activation energy (E_A) effect on the degradation of $I(-1V)$ [18]. This E_A is calculated from the ideality factor of the I *vs.*V curves and is based on an equivalent circuit model for inorganic solar cells [146]. The non-encapsulated devices live only for a few minutes in air, in contrast to vacuum where they are stable for at least several hours. Their results indicate a strong degradation effect from oxygen and light assisted diffusion of oxygen.

One of the main degradation processes for non-encapsulated devices is the quenching of excitons caused by anionic oxygen molecules associated with C_{60} [147]. Molecular oxygen can diffuse through the whole device, and the usual evaporated Al and Ag electrodes are only weak barriers [148–150]. Oxygen causes a strong reduction of the electron mobility in C_{60} [151]. Modified electrodes and also the shift of C_{60} layer further away from the Al electrode does improve device stability [143, 145].

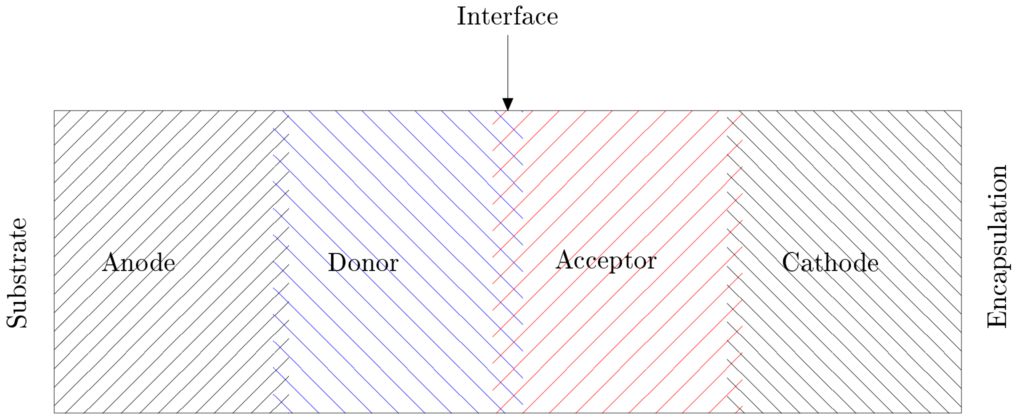

Figure 1.23: Example of a layer structure of a flat donor-acceptor heterojunction solar cell.

Fig. 1.23 shows the layer structure of a simplified donor-acceptor flat heterojunction solar cell. Besides the substrate and the encapsulation, the stability of the bulk of each layer and their interfaces can be analyzed separately.

Bottom electrode, TCO, and the interface TCO / organic

The most frequently used transparent bottom electrode of an organic solar cell or an OLED is made of indium-tin oxide. Sometimes tin oxide, fluorine doped tin oxide, or other degenerated transparent conducting oxides (TCO) are used. These materials are typically processed under temperatures between 200 °C and 500 °C for tuning their optical and electrical properties. However it is known that the layers, especially their surface, are not stable at room or typical operation temperatures (for a comprehensive overview on TCOs see chapter 6 of [152]).It was observed that their surface tends to absorb oxygen, water, and carbon contamination [153–155]. The large amount of literature devoted to the surface treatment of TCOs shows how important this surface and its interface to organic semiconductors are for electronic devices.

The electronic barrier of simple interfaces between metal or TCOs and organic semiconductors can not be correctly described by the difference of the workfunction of the conductor and the conduction (or valence) band of the organic semiconductor. The physical or chemical absorption properties of the organic semiconducting molecules on the conductor can change dramatically the electronic properties [156, 157].

Good electronic injection properties have been achieved by surface treatment of the TCO. The surface treatment consists of a modification of the surface composition by oxidation, by removing excess of oxygen atoms, or by chemically binding another substance to the surface (SAM, acids, etc). Modifications like oxygen plasma treatment are partially reversible and not fully reproducible, e.g. ITOs made by different methods or with different deposition parameters have different compositions [153, 158]. In cases where the TCO is the anode, an oxygen treatment can improve the positive charge carrier injection into the organic semiconductor by completely oxidizing its surface and modifying its workfunction. This modification may introduce physisorbed oxygen on the surface which, if released in the organic layer, can in certain cases work as p-dopant and improve the injection.

When the TCO is a cathode, it must not release oxygen into the acceptor layer, because the acceptor may be oxidized, or it may be p-doped, or the effect of an n-dopant may be compensated.

Oxygen and metal diffusion from the TCO into the organic layer does contribute to unintentional electrical doping, quenching effects in the optically active layers, and even to short circuits [148, 149, 159–161]. It is particularly necessary to avoid contact of the organic material with oxygen, therefore it should be avoided that oxygen impurities are introduced trough the TCO interface.

Another technique to achieve reproducible, and relatively low energy barriers at the TCO - organic interface is the use of buffer layers. Most of the electronic interface effects between TCOs and organic semiconductors can be screened-out by using an insulating layer or a heavily doped organic semiconductor. Typical insulating layers are e.g. SiOx, polytetrafluoroethylene. The insulating layer tends to be very stable, however the tunnel junction increases the operating voltage in an OLED and is probably not viable in a solar cell. The use of a doped layer for the injection is a good solution provided that the dopants do not diffuse into other layers. Doping with metals has a serious stability problem [161] whereas doping with larger organic dopants seems to be a viable solution for long term stability. Typical highly doped layers are PEDOT:PSS (poly(3,4-ethylenedioxythiophene) poly(styrenesulfonate)), F_4-TCNQ: m-MTDATA (4,4',4"-tris-(3-methylphenylphenylamino)triphenylamine m-MTDATA), polyaniline, etc..

Organic Bulk layer(s)

The morphology of the optical active layer plays a very important role in solar cells. For instance, in polymer bulk heterojunctions devices, the thermal treatment is essential to achieve the highest efficiency [162].

The morphology of small molecule donor-acceptor bulk heterojunction layer is also an important factor for the device efficiency. The direct observation of the morphology is difficult, very specific techniques have to be employed for the in-situ observation of the device's morphology. However, targeted modifications during deposition have been performed to determine the optimum conditions [163–165].

What polymer, small molecule, bulk or flat heterojunctions optical active layers have in common is its sensitivity towards contamination. It is necessary that the materials used in these layers do not contain oxidized species. The oxidized species can generate charge carrier traps lowering the mobility and acting as a recombination center for excitons. The optically excited molecules are highly sensitive to oxidation. Although some effects may benefit from oxygen contamination [166–168]. While some effects may be desired, they are not stable because of the diffusion of gases in crystalline organic materials is very fast (given the very thin layers). This general conclusion holds for solar cells and for OLEDs as well. The devices require an encapsulation with gas and moisture barrier and a gas and moisture getter located inside the encapsulated device.

Organic / Metal interface

Similar to the TCO / organic interface, the electronic properties of organic-metal interfaces are very complex and can usually not simply described by the energy levels of the two materials. The group of Kahn and Seki have elucidated several different metal / organic interfaces [169–171]. The general conclusion is that energy level alignment will depend on the molecule and how it is absorbed on the metal surface.

It is difficult to control the interface properties, because the interface is very sensitive even to a monolayer of contaminant. Here again, buffer layers or doped layers are used to achieve reproducible results.

A special situation is the deposition of a metal layer on an organic layer. Because of the small size, and high temperature (high energy) during deposition, the metals tend to diffuse into the organic layers, sometimes even creating short-circuits [172]. Because different organic materials interact differently with different metals, it was proposed to use buffer layers to avoid diffusion. Another problem is that some reactive metals may carry contaminants like oxygen to the organic layers (e.g. Al and oxygen).

The electronic metal-organic interface may also be influenced by a slow oxidation, and hydroxilation of the metal surface. These reactions with oxygen and water in defect regions are the cause of the "bubbles" and so called dark-spots in OLEDs [173–176].

However, the reaction of a metal with an organic layer may also have positive effects, such as improving the injection [177].

Those several different aspects of a device, which can cause instability, offer a large spectrum of investigation and optimization possibilities towards an improved andhighly stable organic solar cell.

1.4 Comparison to the stability of OLEDs

The research and technical development of organic light emitting diodes (OLEDs) is more intense than for organic solar cells, especially before the year 2000. After 2000, a strong increase in government funding and subsidies has strengthened the interest for the development of organic solar cells, when first OLED displays were available in the market (Pioneer in 1998, Kodak in 2003 [152]).

First, the main mechanism of degradation of OLEDs was found to be the crystallization of the small molecule layers and the appearing of "black-spots". The black spots did originate from local heating caused by non-uniform current densities trough the device; this process was also assisted by oxidation and delamination of the electrodes.

All devices have to be protected from oxygen and water, which can react with charged or excited species in the device. The common method is to seal the device, which is made on a glass substrate, using a glass cover, and a getter material inside the cover. Other technologies have been developed, like multilayer polymer / ceramic stacks to enable flexible OLEDs.

The improvement of the lifetime of multilayer small molecule OLED devices was first concentrated in finding (or creating) new transport materials (see chapter 3 [152]) and improving current injection and transport. The best known material used in the electron transport layer and in the emitter layer (as host material) was Alq_3 (Aluminum tris(quinolin-8-olate) CAS Nr. 2085-33-8), which is still largely used. This electron transport material has a rather good stability, therefore the research was focused on increasing the glass transition temperature of the hole transport materials.

It was found that some materials, in solid state, are relatively unstable in ionized form. It was found that the cationic form of Alq_3 is not stable in presence of water [178], consequently Alq_3 is preferably used only as electron transport material and not as emitter host.

The investigations on doping of transport materials and the, to some extent parallel, research on the modification of the effective work function of the electrodes by using thin "injection layers" led to very stable devices.

The efficiency and the lifetime are closely correlated quantities. The excess of applied field necessary to drive the transport in inefficient charge transport layers is transformed into heat. The chemical and energetic interfaces between different materials, specially layers of different materials, should be selected to avoid stress of the materials, such as the creation of exciplexes or radical states which may trigger a chemical reaction. The molecules which perform the conversion between charge carriers and/or excitons into photons must realize this process with a high quantum efficiency, all excitons which are not converted into photons will either quickly decay to the ground state generating heat or decay into a metastable energy level. This metastable energy level can trigger chemical reactions before further decaying into heat. The heat generated in the device can be responsible for morphological changes in the organic layers and also assist in chemical reactions.

Having once solved the initial technical issues, it was found that red emitting OLEDs are very stable [179]. However, devices emitting blue light still degrade faster than desirable for most applications. The transport of charge carriers in OLEDs is already highly optimized, minimizing the stress in the transport layers. Nowadays, the key issue in OLED stability is the stability of the emitter material. It is necessary but not sufficient, that the materials for emitter layers have a very high purity.

The emitter materials suffer the largest stress due to the high rates of charge carrier recombination, excitation, and emission (or non-radiative decay). The higher the energy of the exciton, the lower the stability of the molecule. Triplet excitons introduce an inherent instability, they live longer giving the molecule more chances to fragment or react with other molecules. The non-radiative decay density of triplet excitons can be lowered by mixing phosphorescent emitters in the emitting layer. Some optimized phosphorescent emitters have very low excitonic lifetime [180]. These phosphorescent emitters will also increase the efficiency [181]. Yet, there is no blue triplet emitter with high stability available.

OLEDs with only fully fluorescent emitters have the longest lifetime, however they are limited to around 25% of quantum efficiency due to spin-statistics; 75% of the excitons are created as triplet excitons, which are not allowed to directly recombine emitting light. The total maximum efficiency is slightly higher than 25% because the high triplet exciton density favors the TTA (triplet-triplet annihilation). The TTA between two molecules, each one in a triplet state, can result in one molecule in neutral state and another excited above the first excited singlet level. The high excitation can relax to a singlet state, which can emit light. However, this molecule is very susceptible to fragmentation or reaction due to the high energy of the excitation.

A general conclusion is that the improvement of emission efficiency naturally leads to longer lifetimes, also for the same operating current density. If most of the charge carriers recombine very fast and efficiently, followed by a fast and efficient exciton recombination with light emission, then the stress that the molecules are exposed to is the lowest and the lifetime of the device can potentially be the longest.

Chapter 2

Materials and methods

This chapter includes a description of the materials used in this work and their properties. It also describes the methods used to construct and characterize the solar cells.

2.1 Materials

Conjugated molecules have an extra stability if they are flat, this allows for the highest binding energy on the σ bonds; torsions will lead to lower binding energies. All π electrons must be accommodated in binding orbitals, leading to a high delocalization of the π cloud in flat molecules. The best examples for stable molecules are the aromatic molecules like benzene [182], anthracene, thiophene, etc. Zinc Phthalocyanine (ZnPc) has these characteristics, it is highly planar, and has a high delocalization of the π electrons on the -N=C-N= chain. Even being non planar and having a very low aromaticity, C_{60} can accommodate 6 electrons in its lower unoccupied molecular orbitals without decomposing because its first 6 lower unoccupied orbitals are all symmetric [183].

2.1.1 Fullerene C_{60}

C_{60} and its derivatives are used in many different kinds of organic solar cells as acceptor. These fullerenes have a high intersystem crossing of the self trapped exciton, the excitons are readily transformed into triplet excitons (See section 1.1.3). The triplet excitons have a relatively high diffusion length of about 40 nm [184]. The high diffusion length, associated with high electric mobility and the low LUMO that turns C_{60} (and its derivative [6,6]-phenyl-C61-butyric acid, or PCBM) into a good acceptor are the main reasons for the dominance of the fullerenes in organic solar cells.

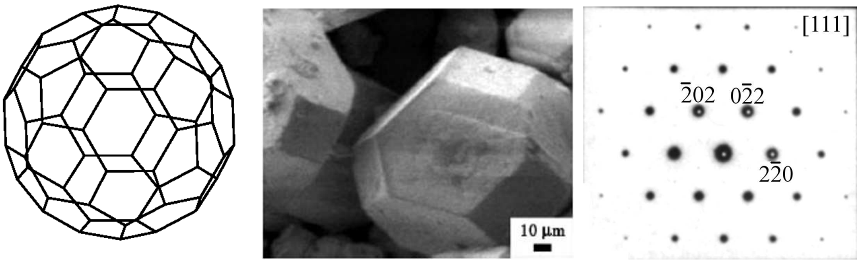

Figure 2.1: (a) Chemical structure of a C_{60} molecule. (b) Scanning electronic micrograph of a C_{60} crystal (Adapted from [185]). (c) X-ray diffraction pattern of a fcc C_{60} crystal along the 111 zone (Adapted from [186]).

The Fullerene C_{60} is a molecule composed only of carbon (Fig. 2.1). It is a symmetric icosahedron, also called buckyball. It forms well defined crystals, they are in simple cubic (sc) phase below 249 K, and fcc (face-centered cubic) above [186]. The molecule rotates freely in a crystal at 300 K [187] with a frequency of 10^{10} Hz [188]. Oxygenated and epoxied C_{60} have the same crystaline phase transitions as pure C_{60} at a slightly higher temperature [189, 190].

The physico-chemical properties of C_{60} are well understood and can be found in books and conference proceedings especially devoted to fullerenes. A compilation of its properties is shown in table 2.1 [191–196]. C_{60} can be reduced by several different compounds, forming CT complexes [195]. The n-doping of C_{60} films was demonstrated with Crystal Violet Radical (CV) [119], Acridine Orange Base (AOB) [118], and other dopants. Li et al. propose that a light activated reaction between AOB and C_{60} occurs, where C_{60} oxidizes the excited AOB and the two molecules form a dyad that acts as a dopant [118].

In thin films, the electronic band gap of C_{60} is close to the optical band gap [193]. However, the first singlet absorption has a very low probability, because a dipole excitation is not allowed due to the high spherical symmetry of the molecule. The first strong absorption peak is below 500 nm.

Optical Properties

Figure 2.2 shows the electronic energy level structure for a C_{60} crystal in the fcc phase [3]. The HOMO-LUMO gap of the fcc C_{60} phase is about 2 eV. The first optical transition is symmetry forbidden and the lowest experimentally observed peaks are at 2.7, 3.6, 4.7, and 5.6 eV [197]. This makes C_{60} a *quasi*-transparent wide-gap semiconductor.

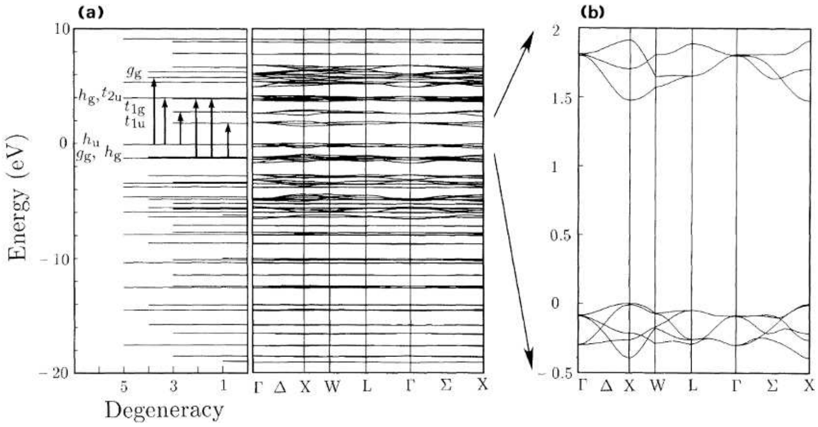

Figure 2.2: (a) Electronic energy levels of the fcc C_{60} crystal and band structure (b). The arows indicate the allowed optical transitions below 6 eV. The HOMO corresponds to the h_u level and the LUMO corresponds to the t_{1u} level. Adapted from [3].

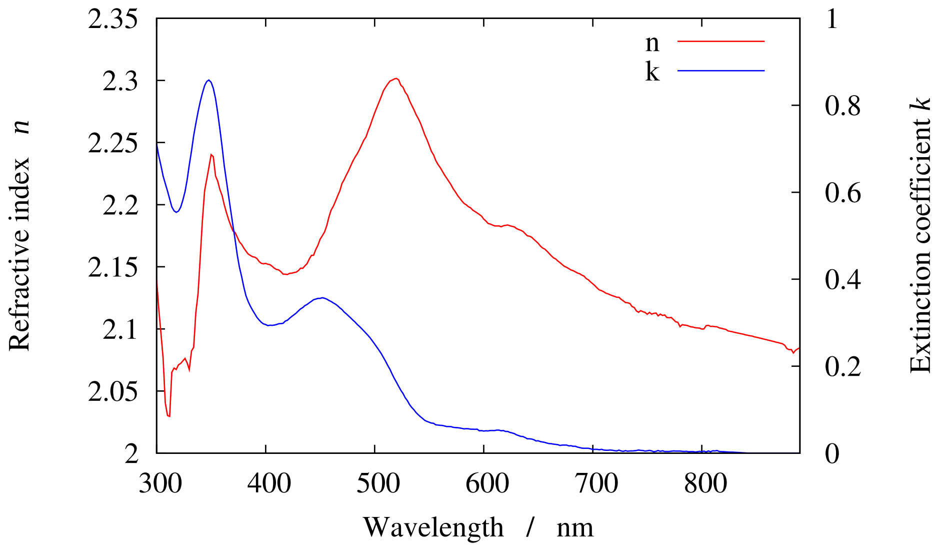

Figure 2.3: Optical constants of C_{60}.

The triplet exciton in C_{60} causes a small Jahn-Teller distortion of about 0.089 eV and 0.040 eV (0.02 Å). The latter one is for the solid state as calculated by [198].

Electronic Properties

C_{60} has up to six reversible oxidation/reduction states [199, 200]. Its LUMO (in the solid state) is relatively low lying, at about -4.0 eV, and its HOMO is located around -6.3 eV [201, 202]. Thus, electrical contacts with metals to the conduction band of C_{60} layers are easily established. The electron mobility is as high as 1 $cm^2V^{-1}s^{-1}$ and the hole mobility is around 10^{-4} $cm^2V^{-1}s^{-1}$ [151]. Due to its high mobility, it is used in many applications, such as solar cells [21], field effect transistors [203], and diodes [204].

Stability

Since its rings are not flat, C_{60} does not have the extra stability of the aromatic compounds, and it is susceptible to some chemical reactions, especially with oxygen. The study of interactions between C_{60} and oxygen is of fundamental importance because oxygen is a very efficient quencher of triplet excitations on C_{60}. The bimolecular quenching constant is 1.6 10^9 $M^{-1}s{-}1$ (see Kadish, chapter 5 [193]). Oxygen is a stronger acceptor than C_{60}, leading to a p-compensation or p-doping of C_{60}.

Könenkamp et al have shown that the electron and hole mobility of C_{60} are highly sensitive to oxygen; μ_e drops from 10^0 to 10^{-5} $cm^2V^{-1}s^{-1}$ and μ_h changes from 10^{-4} to 10^{-5} $cm^2V^{-1}s^{-1}$ after an uptake of O_2 for 100 h [151, 205].

Gases like O_2, N_2, CO_2, CO, Ar easily diffuse into the C_{60} crystal lattice [206]. It is suggested that, in the dark and at room temperature, the chemical interaction with those gases in the C_{60} lattice is very weak and controlled mainly by Van der Waals forces. O_2 will occupy 8 positions in one unit cell, the tetrahedral and octahedral voids. In the dark and at room temperature, O_2 hardly dissociates, and it probably will not form a chemical bond with solid C_{60}. However, there will be a reaction induced by light when low energy electrons from excited C_{60} are transferred to oxygen forming the reactive ${O_2}^-$ species. This oxygen binds to the carbon π bounds forming >C=O. CO_2 and CO are also created even at temperatures as low as 20 K [207, 208]. At 20 K, the reaction saturates due to a surface passivation. The activation temperature for C_{60} oxidation in the dark is 575 K (~302 °C) [206], when it probably forms triads like C_{60}-O-C_{60}, C_{120} and C_{119} [200, 209–211]. In thin films, the following reaction can occur under illumination (see Kadish, pp. 239, and pp. 253 [193]):

$$ {C_{60}}^{1*} \xrightarrow{ISC} {C_{60}}^{3*} + O_2 \rightarrow C_{60} + {}^1O_2({}^1\Delta) \rightarrow C_{60}O \tag{2.1} $$

Hayashi et al have shown that AOB + C_{60} is stable against oxygen when deposited under ultra high vacuum (UHV) [212].

It has been shown that the reaction 2.1 can be avoided by using TiO_2 clusters. The energy

Singlet energy	E (singlet)	= 1.99 eV
Triplet energy	E (triplet)	= 1.57 eV
Singlet excitation	λ_{max} (singlet)	= 920 nm
Triplet excitation	λ_{max} (triplet)	= 747 nm
Lifetime of singlet state	ε (triplet)	= 20 000 $M^{-1}cm^{-1}$
Lifetime of triplet state	τ (singlet)	= 1.3 ns
Exctinction coefficient	τ (triplet)	= 135 μs
Oxidation potential	$E_{1/2}(^{1*}C_{60}/C_{60}^{\cdot-})$	= 1.44 V *vs.* SCE
Reduction potential	$E_{1/2}(^{3*}C_{60}/C_{60}^{\cdot-})$	= 1.01 V *vs.* SCE
Fluorescent quantum yield	Φ (fluorescence)	= 1.0 $\times 10^{-4}$
Phosphorescent quantum yield	Φ (triplet)	= 0.96
Molecular quenching constant by oxygen	k_q (oxygen)	= 1.6 $\times 10^{9}$ $M^{-1}cm^{-1}$
Molecular quenching constant by biphenyl	k_q (biphenyl)	= 1.7 $\times 10^{10}$ $M^{-1}cm^{-1}$
Lowest unoccupied molecular orbital	LUMO	= -4.0 ± 0.1
Highest occupied molecular orbital	HOMO	= -6.3 [201][202]
Electron mobility	μ_e	= 1 $cm^2V^{-1}s^{-1}$ [151]
Hole mobility	μ_h	= 10^{-4} $cm^2V^{-1}s^{-1}$ [151]

Table 2.1: Opto-electronic properties of solid C_{60}. Adapted from Kadish (chap.1 and chap.5) [193]

transfer from TiO_2 triplet leaves a C_{60} anion that is more energetically stable against oxidation (see Kadish pp. 239 [193]).

Non reacted C_{60} can be emptied of oxygen by heating under vacuum at temperatures below 575 K. Part of the oxygen will degas and the other part will react, eventually forming CO/CO_2, partly destroying the fullerenes [206]. The intermediary smaller products of the oxidation have even numbers of carbon atoms [213].

2.1.2 Zinc Phthalocyanine

Phthalocyanines are economically very important. They are mainly used as pigments, due to their high absorption coefficient (up to 10^5 $M^{-1}cm^{-1}$ at around 620 nm) and high stability. They can be produced in large quantity and with high purity, the simplest synthetic route consists in only one step and has a high yield. There are many books and even a society is devoted to the study of phthalocyanines (Society of Porphyrins and Phthalocyanines) [214–216].

ZnPc is, together with CuPc, one of the most stable forms of phthalocyanine. It can be easily n- and p- doped by organic molecules such as $Ru(terpy)_2$ and F_4-TCNQ [56], forming ohmic contacts with usual electrodes such as Au, Al, and ITO. The sublimation temperature is relatively high (around 330 °C), and it forms very thermally stable films. Figure 2.4 shows the chemical structure of the planar, aromatic compound.

Optical Properties

Solid films of ZnPc deposited at low or room temperature with thermal or flash evaporation are a mixture of the metastable α phase and the stable β phase. Deposition on a substrate under higher temperatures will lead to an increased portion of the material crystallizing in the β phase. The phase transition itself occurs at 538 K. The β phase has a slightly lower gap, and the mixture of the two phases forms the typical absorption shape of solid ZnPc between 550 and 800 nm. The absorption and the optical constants can be seen in figure 2.5 [217, 218].

The main optical properties of ZnPc are listed in table 2.2. Comparing the exciton energy with the HOMO-LUMO gap, one can estimate the exciton binding energy to be 0.11 eV for the singlet exciton and 0.81 eV for the triplet exciton.

Electronic Properties

The LUMO of Zinc Phthalocyanine is at -3.34 eV and the HOMO is around -5.28 eV. It can be efficiently p- and n-doped by organic dopants such as F_4-TCNQ and Ru(terpy)$_2$, respectively. The hole mobility is around 1×10^{-3} cm^{2}V^{-1}s^{-1} [222].

The transport activation energy decreases with increased doping ratio, from 0.32 eV (undoped [223]) to 0.21 eV (for a ratio 1:50 of F_4-TCNQ:Zinc Phthalocyanine [85]). Zhou and Gould found that the activation energy of CuPc increases after heating by more than 0.4 eV [224]. Kerb and van Faassen found a transport activation energy in ZnPc of 0.23 eV attributed to oxygen doping [166]. They found that samples exposed to air may be unintentionally oxygen doped. A several nanometer thick film of ZnPc exposed to air will be saturated with oxygen in a few minutes. Reducing a ZnPc film by heating in an H_2 atmosphere leads to a near intrinsic condition with an activation energy of 1.07 eV [225].

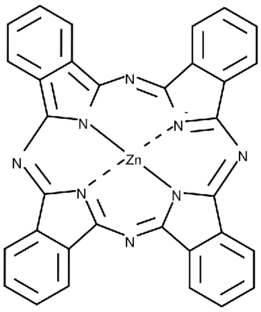

Figure 2.4: Chemical structure of a ZnPc molecule.

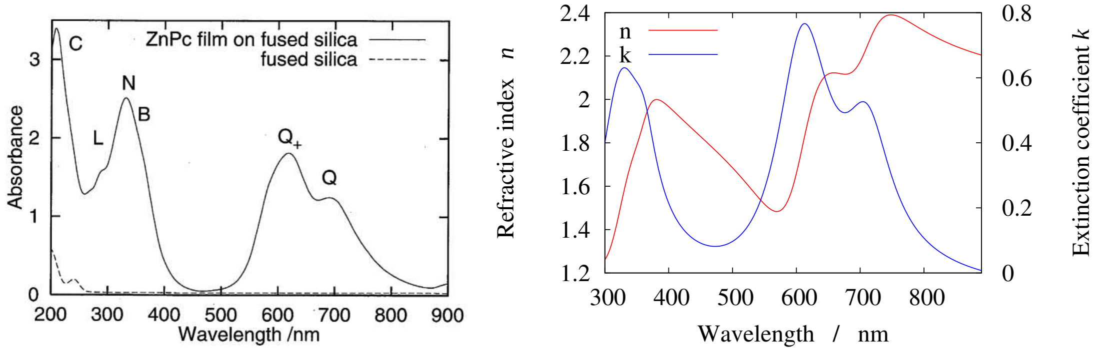

Figure 2.5: Left: Absorbance of ZnPc. [218]. Right: Optical constants of ZnPc (this work).

Singlet energy	E (singlet)	= 1.83 eV
Triplet energy	E (triplet)	= 1.13 eV
Singlet excitation	λ_{max} (singlet)	= 672 nm
Triplet excitation	λ_{max} (triplet)	= 1.1 μm
Exctinction coefficient	ε	= 346736 $M^{-1}cm^{-1}$
Lifetime of singlet state	τ (singlet)	= 3.8 ns
Lifetime of triplet state	τ (triplet)	= 1.1 ms (77 K)
Oxidation potential	$E_{1/2}(^{1*}C_{60}/C_{60}^{\cdot-}$ E(p+/P)	= +0.92 eV vs NHE
Reduction potential	$E_{1/2}(^{3*}C_{60}/C_{60}^{\cdot-}$ E(p/P-)	= -0.65 eV NHE
Fluorescent quantum yield	Φ (fluorescence)	= 0.3
Phosphorescent quantum yield	Φ (triplet)	= 0.98 ± 0.18 [219]
Molecular quenching constant by oxygen	k_q (oxygen)	= $\times 10^{9} M^{-1} s^{-1}$
Molecular quenching constant by biphenyl	k_q (biphenyl)	= $\times 10^{10} M^{-1} s^{-1}$
Lowest unocupied molecular orbital	$LUMO$	= -3.34 eV [220]
Highest occupied molecular orbital	$HOMO$	= -5.28 eV [220]
Dielectric constant	ε_r	= 3.0
Seebeck coefficient at 340 K	S_{Seebeck} at $340K$	= +285 $\mu V K^{-1}$ [221]
Activation energy	E_{at}	= 0.31 eV [221]
Hole mobility	1 $10^{-3}\mu_h$	= $\mathrm{cm^2V^{-1}s^{-1}}$

Table 2.2: Optical and electronic properties of ZnPc [31].

Stability

Phthalocyanines are very stable against oxidation and decomposition under UV light. They are much more stable in the solid state than in solution. ZnPc as well as other porphyrins decompose in solution, the decomposition rate is enhanced by illumination and also by the presence of oxygen [226].

ZnPc is strongly doped by molecular oxygen. Oxygen acts as an acceptor, p-doping (or compensating), the molecule. Oxygen also affects the lifetime of the triplet state, the lifetime for thermal deactivation of triplet excitons is lowered from 75 μs to 7 μs in presence of oxygen for ZnPc in solution [219].

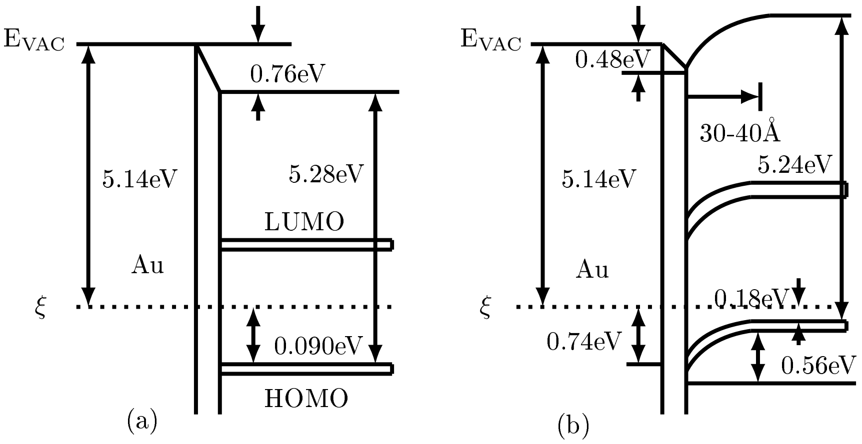

Figure 2.6: Energy levels of the interface between ZnPc and Au with (a) undoped ZnPc and (b) ZnPc doped with 3% F_4-TCNQ (adapted from [220]).

Oxygen doping is not wanted in a solar cell, because of its inherent instability. Oxygen can easily diffuse to an unwanted position in the device or lead to chemical reactions. The effects of oxygen on phthalocyanine films are not fully understood. It is not clear how low concentrations of oxygen affect the opto-electronic properties in a solid ZnPc layer. According to Barbon et al., singlet excitons in ZnPc have a long lifetime, and a diffusion length of up to 30 nm. The generation of triplet excitons is mediated by oxygen as it can only be detected if oxygen is present in the film [227]. Experiments in thin film FHJ organic solar cells have shown an optimum layer thickness of around 15 nm. Many parameters, other than the exciton diffusion length, can be responsible for this optimum layer. A possible explanation for the discrepancy between the optimum thickness and the exciton diffusion length is that unintended oxygen doping in the photo-active ZnPc layer reduces the exciton diffusion length either by trapping it or by recombining the charge carriers.

2.2 Other materials

Other materials used in this work are listed in table 2.3. MeoTPD, MeNPB, DiNPB are used as hole transport layers, either in their intrinsic or doped form. The triphenyl derivatives are known for their relatively high hole mobility, compared to other small molecules. MeoTPD has mobility in the order of 10^{-3} $cm^2V^{-1}s^{-1}$ [228], DiNPB has a hole mobility of about 10^{-4} $cm^2V^{-1}s^{-1}$ [229]. MeoTPD and MeNPB have their HOMO of around -5.2 eV and can be successfully doped with F_4-TCNQ (2,3,5,6 -Tetrafluoro -7,7,8,8- tetracyanoquinodimethane). A stronger acceptor is needed to dope DiNPB because DiNPB has a deep lying HOMO around -5.4 eV. Therefore, we use a commercial molecular dopant (NDP2,

MeoTPD	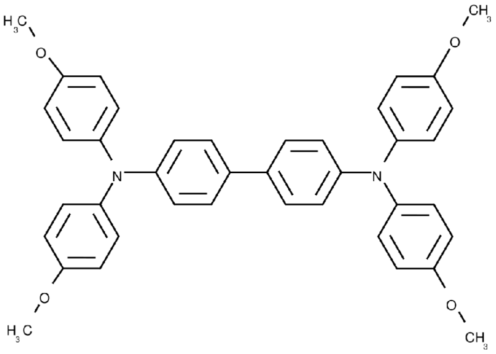 N,N,N',N'-Tetrakis(4-methoxyphenyl)-benzidine CAS Nr. 122738-21-0
MeNPB	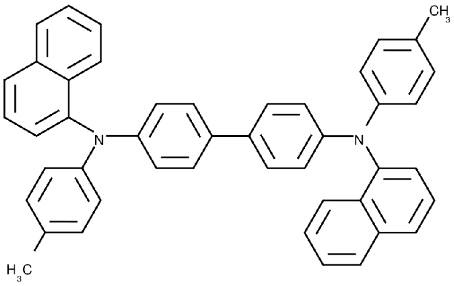 [1,1'-Biphenyl]-4,4'-diamine,N,N'-bis(4-methylphenyl)-N,N'-di-1-naphthalenyl CAS Nr. 244260-36-4
DiNPB	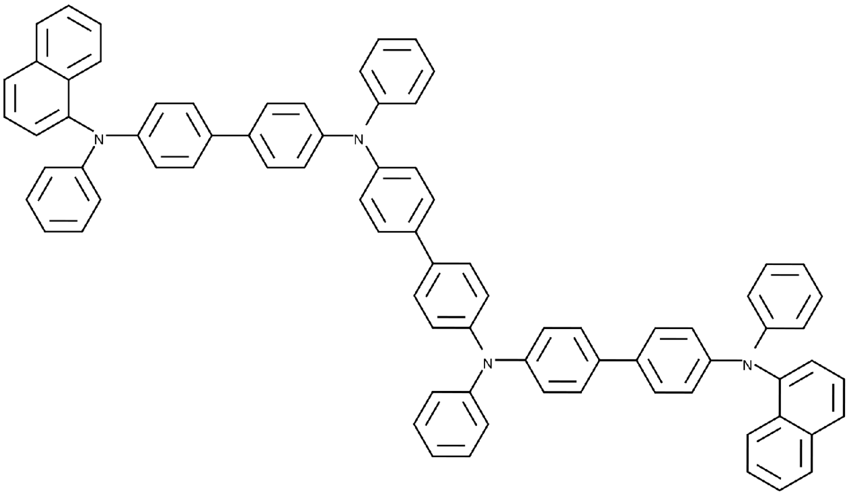 N,N'-Diphenyl-N,N'-bis(4'-(N,N-bis(naphth-1-yl)-amino)-biphenyl-4-yl)-benzidine CAS Nr. 292827-46-4
AOB	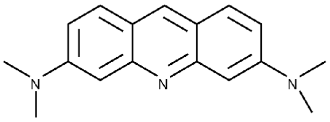 3,6-bis (dimethylamino) acridine

Table 2.3: Other materials used in this work. MeoTPD, MeNPB, DiNPB are used as hole transport layers, intrinsic or doped with a commercial molecular dopant (NDP2, from Novaled AG). AOB is used as n-dopant for C_{60}.

from Novaled AG). AOB is used as n-dopant for C_{60}. The triphenyl derivatives used in this work have a high lying LUMO so that they are all wide gap materials, being transparent for practical purposes.

2.3 Fabrication of devices

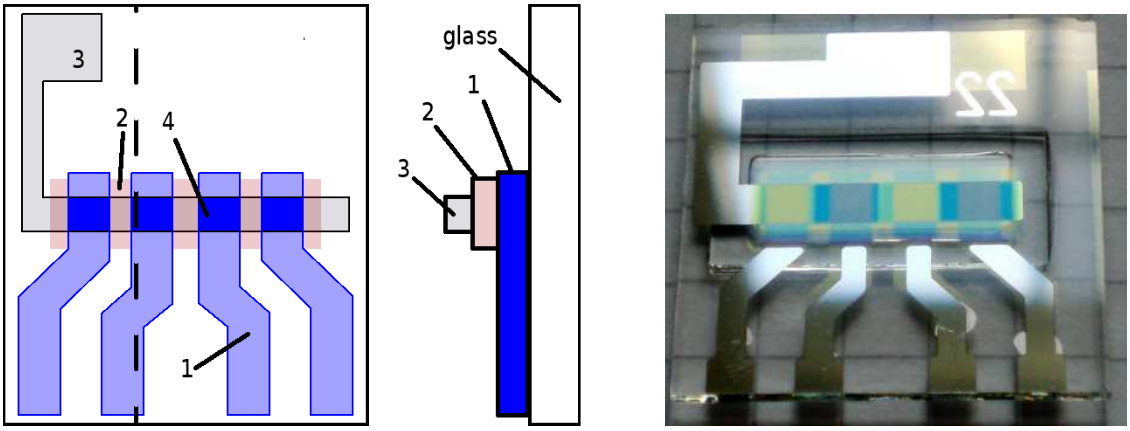

(a) (b) (c)

Figure 2.7: Sample structure (not to scale): (a) bottom view through the glass substrate, and (b) side cut on the dashed line. The different organic layers (2) are deposited over the ITO (1), the metal electrode (3) follows on top. The device active area (4) is defined by the superposition of the ITO with the metal electrode (6.3 mm^2). An Al layer is deposited over the ITO layer that is used for wiring. This provides a mechanical reinforcement of the Al connection and a electrical reinforcement of the ITO connection. The reinforcements are not shown in the drawing to maintain its clarity. (c) is a corresponding photo of the drawing (a).

Figure 2.7 schematically shows the sample structure in (a) and (b) and an image of a sample in (c). Devices are cut from a single larger glass wafer. The wafer contains 36 samples, arranged into 6 rows and 6 columns. Expect for some special cases, only the 16 central samples are normally used.

The glass with patterned indium-tin oxide (ITO) layer is provided by TFD (Thin Film Devices, Inc). Before going into the glove box, the wafer is cleaned in ultra sonic bath for 10 minutes each in: ethanol, acetone, and isopropanol. The substrate is further heated to 150 ^{o}C in low vacuum in the load chamber of the glove box for about 1 h. The loading into the vacuum chamber was made before the substrate's temperature reached room temperature. After loading into the deposition chamber, the wafer is further degassed in ultra high vacuum (UHV, pressure $< 5\times10^{-6}$ Pa) overnight.

All organic and metal layers are deposited in the vacuum chamber without breaking the vacuum. Organic layers were deposited at a rate of 0.5 Å/s at a pressure below 5×10^{-6} Pa and Al at 15 Å/s and a pressure below $1{\times}10^{-4}$ Pa. The organic dopant is deposited at a rate of 0.02 Å/s. The thickness is measured with independent calibrated quartz crystal monitors (QCM). For doped layers, 2 sources with independent QCMs are used to adjust the rates for each material. The molecular vapor is blocked by a shutter which is only opened when all rates are stable.

The encapsulation is done on the wafer with a glass cover that has a cavity with a getter inside. The cover is glued to the glass substrate with a light curing sealant XNR5516 (Nagase GmbH) using an automatic dispenser. A metal shadow mask protects the sample during UV exposure. The encapsulation is performed in the nitrogen flooded glove box. After encapsulation, the wafer is cut into the samples, this procedure is done in air. The samples are then stored into a glove box until they are further characterized.

2.4 Processing of I *vs*.V data

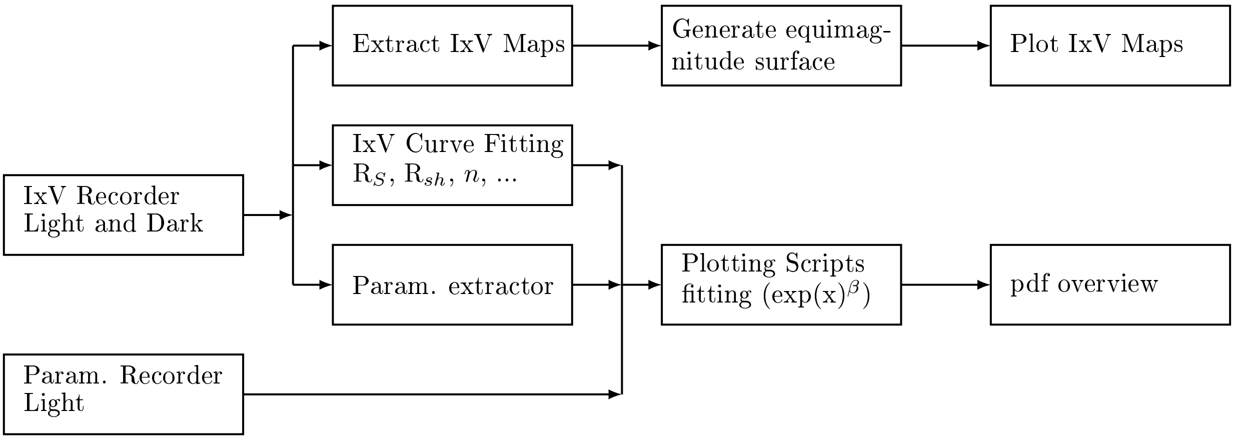

Figure 2.8: Overview of the semi-automated data treatment tools.

The characterization of aging of the solar cells is made by analyzing the I *vs*.V curves vs. time. The solar cell is aged under constant illumination and constant temperature. From time to time, the setup records the characteristic parameters V_{OC}, I_{SC}, FF, and also the full I *vs*.V curve. Electrical measurements were done with a Keithley source measure unit 2400.

This section describes the data management of the measured I *vs*.V curves. Almost all graphics were made with gnuplot scripts [230], which are to some extent automatically created by self written python scripts [231]. Fitting of data is made with gnuplot or qtiplot. Figure 2.8 highlights the automated or semi-automated data processing steps. The I *vs*.V and parametric acquisition is either fully automated or executed by calling a specific script.

The section further explains the fitting procedure using the Shockley equation. The equation is modified or rewritten to facilitate the extraction of some macroscopic parameters. The following part explains the method for extraction of series resistance developed by Kaminski et al [232]. Finally, the fitting procedure for the stretched exponential is detailed in the last part.

2.4.1 Three-dimensional overview of the transfer curve aging

To represent the dynamics of aging of a solar cell, one can use several kinds of graphical representations. The variation of the maximum power over time is the most important parameter but still it does not deliver much information.

The characteristic parameters FF, V_{OC}, and I_{SC} can also be plotted over time. This increased number of plots will make the overview for a large number of samples more complicated. One solution is to normalize all the parameters, dividing the parameter X(t) by the first value X(t=0), where t is the time relative to the start of the measurement.

The comparison of the first and last I *vs.*V is a much more complete way of showing the changes of the solar cells conversion characteristics. A way to plot all the I *vs.*V curves on one and the same plot is on a 3-dimensional plot where the coordinates of one {x,y,z} point are { t (time), V (voltage), I (current) }. This was accomplished in this work by plotting in a semi-log way {t, V, log(|I|)}. The semi-log plot makes the comparison between photocurrent region (reverse bias) and the forward current easier because the magnitude of the forward current is much higher due to its (in first approximation) exponential nature.

The three-dimensional plot in figure 2.11 contains all I *vs.*V curves taken during one aging experiment. One of these I *vs.*V curves is shown in figure 2.10 as a semi-log plot, and in figure 2.9 with linear axis. The applied voltage makes the ordinate, and the time makes the abscissa in this planar projection of a three-dimensional view of I *vs.*V *vs.* t. The current magnitude is represented by the color, with its Δt determined by the frequency of I *vs.*V curve measurements.

Equimagnitude lines are plotted in form of dotted lines to further assist the data interpretation (see Fig. 2.12). Voltage values separated by a defined ΔV interval from the first I *vs.*V data set are taken as reference points.

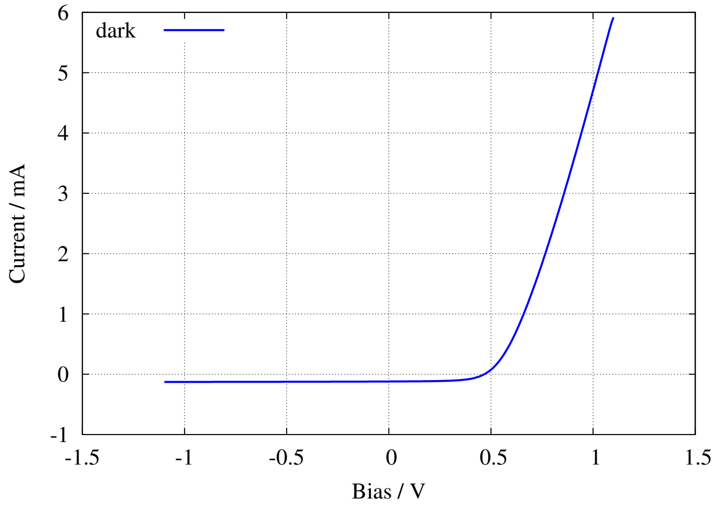

Figure 2.9: Typical I *vs.*V *curve of an illuminated organic solar cell in a linear plot.*

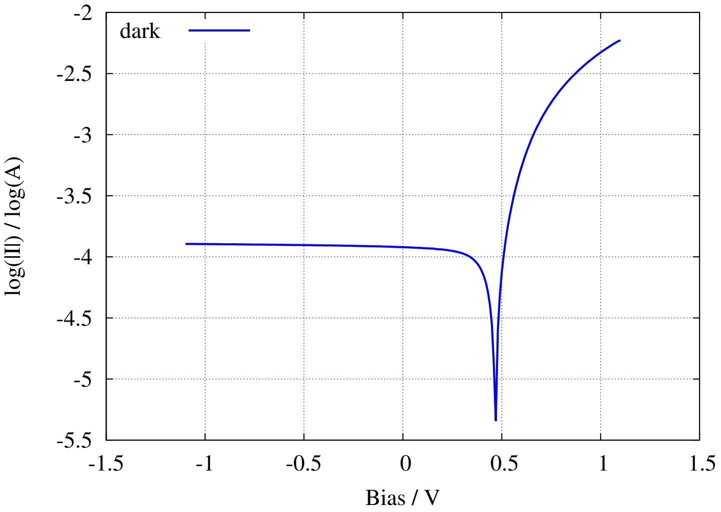

Figure 2.10: Typical I *vs.*V *curve of an illuminated organic solar cell a semilogarithmic plot. The comparison between photocurrent region and the forward current is easier because the forward current is an exponential function of the applied voltage.*

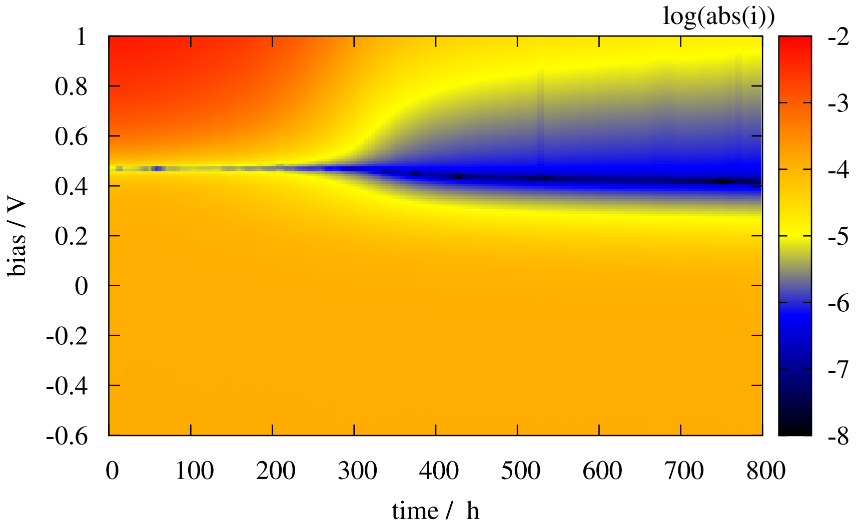

Figure 2.11: This planar projection of a three-dimensional plot shows the current magnitude in color. The applied voltage is the ordinate and the time the abscissa.

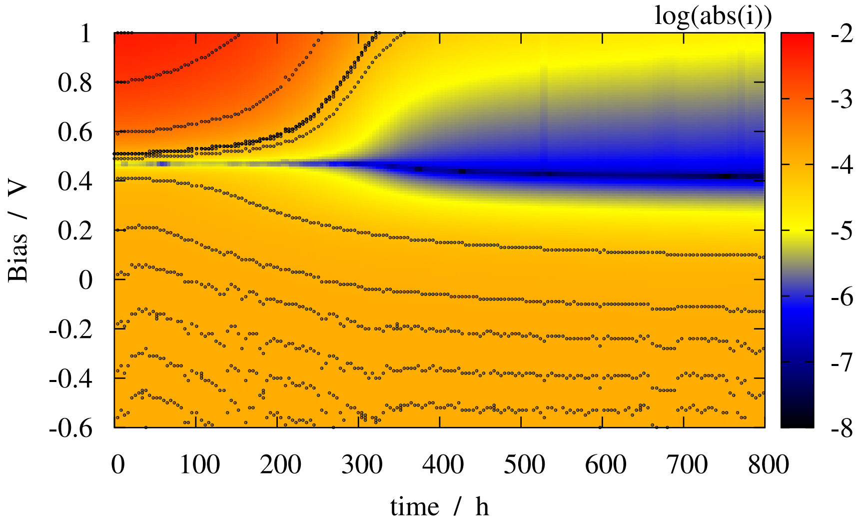

Figure 2.12: Three-dimensional I *vs.*V *vs.time plot showing equimagnitude lines (dotted lines). They are included to further assist the data interpretation.*

2.4.2 Fitting of I *vs.*V curve with the Shockley equation

A straightforward fit of the I *vs.*V data can be done with the Shockley equation. It can be modified to include the macroscopic components of the parallel and the series resistance of a simple equivalent circuit. The Shockley equation for a pn diode is:

$$\mathrm{I} = \mathrm{I_0}\left(\exp\left(\frac{\mathrm{qV}}{\mathrm{nkT}}\right) - 1\right) \tag{2.2}$$

where n is the ideality factor, I the current, $\mathrm{I_0}$ the reverse bias saturation current, $\mathrm{I_{PH}}$ the photo current and V is the voltage.

If we include the photocurrent, the equation becomes:

$$\mathrm{I} = \mathrm{I_0}\left(\exp\left(\frac{\mathrm{qV}}{\mathrm{nkT}}\right) - 1\right) - \mathrm{I_{PH}} \tag{2.3}$$

Considering the current loss through a parallel resistor R_{sh} :

$$\mathrm{I} = \mathrm{I_0}\left(\exp\left(\frac{\mathrm{qV}}{\mathrm{nkT}}\right) - 1\right) - \mathrm{I_{PH}} - \frac{\mathrm{V}}{\mathrm{R_{sh}}} \tag{2.4}$$

We can also consider the voltage loss over a series resistor R_S, then the equivalent equation is [233]:

$$\mathrm{I} = \mathrm{I_0}\left(\exp\left(\frac{\mathrm{q(V - IR_S)}}{\mathrm{nkT}}\right) - 1\right) - \mathrm{I_{PH}} - \frac{\mathrm{V - IR_S}}{\mathrm{R_{sh}}} \tag{2.5}$$

2.4.3 Fitting of forward direction

For high forward currents, we can assume that the parallel resistance is ∞ (in Eq. 2.5), we can neglect the last term, and rewrite the equation such that V and I are fully separated:

$$\mathrm{V} = \ln\left(\frac{\mathrm{I - I_{PH}}}{\mathrm{I_0}} + 1\right)\frac{\mathrm{nkT}}{\mathrm{q}} + \mathrm{IR_S} \tag{2.6}$$

There is a change in sign on the photo current ($\mathrm{I_{PH}}$), because on the forward direction the photo current mainly contributes positively to the current. To simplify the calculation procedure, $\mathrm{I_{PH}}$ is considered as constant over V and the approximation $\mathrm{I_{PH}} \sim \mathrm{I_{SC}}$ is made (similar as in Sze [234], and in [233]). More accurate fits are obtained from the dark I *vs*.V curve, where there is no influence from $\mathrm{I_{PH}}$.

Variable	meaning	typical range for initial guess
I	current	independent variable
V	voltage	dependent variable
$\mathrm{I_0}$	reverse bias saturation current	$[5.10^{-8}$ A, $2.10^{-6}]$ A
$\mathrm{I_{PH}}$	photo current	fixed, measured value
n	ideality factor	$[1.7, 2.5]$
R_S	series resistance	$[10, 200]\ \Omega$
R_{sh}	shunt resistance	$1.10^4\ \Omega$

Table 2.4: Initial guess for the parameters used in automated fitting of I *vs*.V curves. The fitting is limited to 10 000 iterations with a tolerance in between iterations of 1.10^{-4}.

Equation 2.6 is used on the first quadrant (forward current) mainly to determine the series resistance. The solver used is the Levenberg-Marquardt algorithm from the GSL (Gnu Scientific Library [235]). The initial guess for the parameters used in automated fitting of I *vs*.V curves is given in Tab. 2.4. The fitting runs until the convergence with a tolerance of 1.10^{-4} is reached or 1000 iterations are done. The initial Jacobian is given by $J(i,j) = \frac{df_i}{dx_j}$ which, for eq. 2.6 is :

$$\frac{d\mathrm{V}}{d\mathrm{I_0}} = -\frac{nkT}{q(\mathrm{I} - \mathrm{I_{PH}} + \mathrm{I_0})} \tag{2.7}$$

$$\frac{d\mathrm{V}}{d\mathrm{R}_S} = \mathrm{I} \tag{2.8}$$

$$\frac{d\mathrm{V}}{dn} = -\frac{kT}{q}\ln\left(\frac{\mathrm{I} - \mathrm{I_{PH}}}{\mathrm{I_0}} + 1\right) \tag{2.9}$$

2.4.4 Extraction of the series resistance

It is very important to know the series resistance of a solar cell, because the performance of the device drops drastically for relatively small increases in the R_S. The R_S is an effective value of the total resistance that a current sees when passing trough the device. R_S is obtained by fitting the equation of an equivalent circuit (section 1.2.3) to the measured I *vs*.V data of the device. One way to determine R_S is to fit the Eq 2.5 or Eq. 2.6 as explained before. Another more simple approach to extract the value of the series resistance is to fit a line to the data points of very high forward current (see Fig. 2.13). The following mathematical deduction shows that this approximation is reasonable. Starting with the Shockley equation:

$$\mathrm{I} = \mathrm{I}_0 \left(\exp\left\{ \frac{\mathrm{q(V - IR_s)}}{\mathrm{nkT}} \right\} - 1 \right) \tag{2.10}$$

The expansion of the exponential term of the Shockley equation into power series can be approximated to a linear equation if terms with the power of 2 and higher are neglected (Eq. 2.11).

$$\frac{\mathrm{I}}{I_0} = 1 + \left(\frac{q(\mathrm{V - IR_s})}{nkT} \right) + \left(\frac{q(\mathrm{V - IR_s})}{nkT} \right)^2 /2! \; \ldots \; - 1 \approx \left(\frac{q(\mathrm{V - IR_s})}{nkT} \right) \tag{2.11}$$

$$\frac{nkT}{qI_0} \approx \frac{(\mathrm{V - IR_S})}{I} \tag{2.12}$$

$$\frac{I}{I_0} \frac{nkT}{q} = \mathrm{V - IR_S} \tag{2.13}$$

$$-\frac{nkT}{qI_0} + \frac{\mathrm{V}}{\mathrm{I}} = \mathrm{R}_S \tag{2.14}$$

Equation 2.14 can be further simplified, the term $\frac{qI_0}{nkT}$ is very small.

$$\frac{\mathrm{V}}{\mathrm{I}} \approx \mathrm{R}_S \tag{2.15}$$

The result of the simplification is an Ohmic law. Because the line does no start on V=0, a constant must be included by hand:

$$\frac{\mathrm{V + V_1}}{\mathrm{I}} = \mathrm{R}_S \tag{2.16}$$

According to equation 2.16, R_S is the slope of a line fitted on the high forward current region of an I *vs*.V plot. This equation is only valid for higher currents and is more accurate for I *vs*.V curves which are more strongly limited by an higher R_S (i.e. more linear).

Fig. 2.13 shows a linear and a diode equation fit on the same I *vs*.V curve. In this case both fits achieve very close values for the series resistance because its value is high, meaning that the I *vs*.V curve is highly limited by the R_S. Experiments show that the linear fit is not accurate enough. For I *vs*.V curves with lower R_S, it should be accurate only for very high forward currents. However, in a

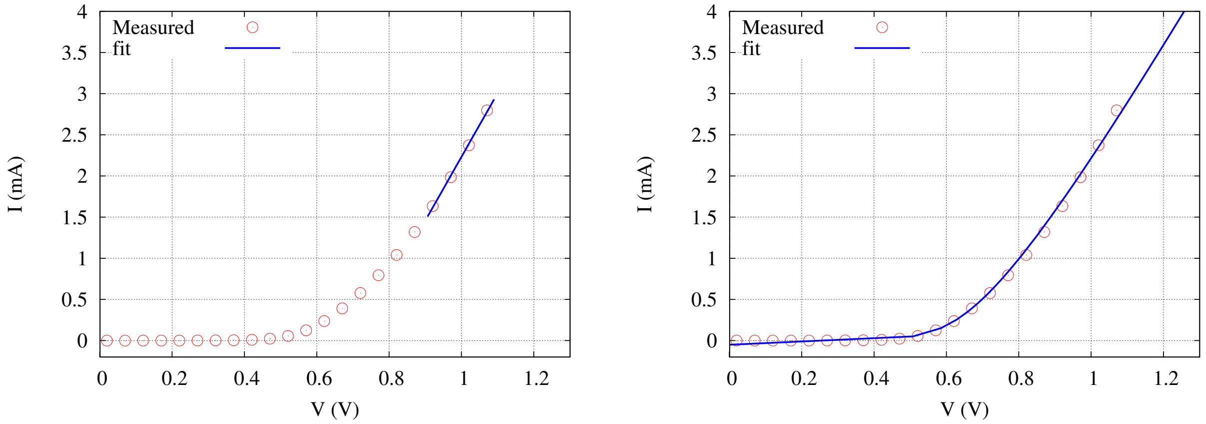

Figure 2.13: Left: Linear fit of the points within the current range 1.5 10^{-3}A to 3 10^{-3}A. The range is chosen manually. The linear function is $I = (V - V1)/R_S$, where R_S =129.1 Ω and V1=0.71 V. Right: Fit of the equation 2.6 with R_S=124.7 Ω, n=2.27, and I_o=1 10^{-8} A.

high current density region, other effects will take place, such as space charge limited current, making the linear approximation no longer valid.

Kaminski et al [232] have shown a better solution for extracting the value of R_S from a measured I *vs*.V curve. In this method, the Shockley equation is approximated for high currents to:

$$\mathrm{I} = \mathrm{I}_0 \left(\exp\left\{ \text{₵}\,(\mathrm{V} - \mathrm{IR}_\mathrm{S}) \right\} \right) \tag{2.17}$$

with ₵ being $\frac{q}{nkT}$. Equation 2.17 is equivalent to:

$$ln(\mathrm{I}) - \ln(\mathrm{I}_0) = \text{₵}\,(\mathrm{V} - \mathrm{IR}_\mathrm{S}) \tag{2.18}$$

The variables in the equation are subtracted from a point $\{\mathrm{V}_\mathrm{x}, \mathrm{I}_\mathrm{x}\}$ of the measured dataset:

$$ln(\mathrm{I}) - \ln(\mathrm{I}_\mathrm{x}) = \text{₵}\,(\mathrm{V} - \mathrm{IR}_\mathrm{S}) - \text{₵}\,(\mathrm{V}_\mathrm{x} - \mathrm{I}_\mathrm{x}\mathrm{R}_\mathrm{S}) \tag{2.19}$$

$$\frac{ln(\mathrm{I}/\mathrm{I}_0)}{\mathrm{I} - \mathrm{I}_0} = -\,\text{₵}\,\mathrm{R}_S + \text{₵}\,\frac{\mathrm{V} - \mathrm{V}_\mathrm{x}}{\mathrm{I} - \mathrm{I}_\mathrm{x}} \tag{2.20}$$

The authors rewrite the equation 2.19 in 2.20. This corresponds to a straight line making:

$$X = \frac{\mathrm{V} - \mathrm{V_x}}{\mathrm{I} - \mathrm{I_x}} \tag{2.21}$$

$$Y = \frac{ln(\mathrm{I}/\mathrm{I_0})}{\mathrm{I} - \mathrm{I_0}} \tag{2.22}$$

The dataset $\{X, Y\}$ is constructed by taking the the first $\{\mathrm{V_x}, \mathrm{I_x}\}$ point of the range until the last one, repeating the operation for the second point $\{\mathrm{V_{x+1}}, \mathrm{I_{x+1}}\}$ and so on, until the point before the last. This procedure gives higher weight to the higher current values, improving the approximation 2.17.

2.4.5 Fitting of the shunt resistance

Equation 2.23 is used on the third quadrant (saturation current), also determining the shunt resistance. In this case, Eq. 2.5 is simplified by making $\mathrm{R}_S \rightarrow 0$.

$$\mathrm{I} = \mathrm{I_0}\big(\mathrm{e}^{\frac{\mathrm{qV}}{\mathrm{nkT}}} - 1\big) - \mathrm{I_{PH}} + \frac{\mathrm{V}}{\mathrm{R_{sh}}} \tag{2.23}$$

Again, the Levenberg-Marquardt solver is used for the fit. The initial Jacobian used is given by $J(i,j) = \frac{df_i}{dx_j}$ which, for eq. 2.6 is :

$$\frac{d\mathrm{I}}{dn} = -\mathrm{I_0}\frac{\mathrm{qV}}{\mathrm{n^2kT}}\mathrm{e}^{\frac{\mathrm{qV}}{\mathrm{nkT}}} \tag{2.24}$$

$$\frac{d\mathrm{I}}{d\mathrm{R}_{sh}} = -\frac{\mathrm{V}}{\mathrm{R}_{sh}{}^2} \tag{2.25}$$

Fitting with equations 2.6 and 2.23 is implemented in the data extraction software (sceval, see appendix 8.3.1). The validation of the code was done by making the same fit with the software developed here and Qtiplot.

2.5 Fitting of decay curves: activation energy and acceleration factor

The equation used to fit the transient measurements is a stretched exponential of type $A = A_0 exp[-(t/\tau)^\beta]$ [236], where A is the measured quantity, A_0 is the initial value at time $t_0 = 0$, t is the time (abscissa), τ is the decay constant, and β is a factor related to distribution of τ in the ensemble [236].

The stretched exponential, also called Kohlrausch function [237–239] is the most simple way to describe the decay of a complex statistical distribution [240]. This function can be used to obtain good fits to the I_{SC} decay curve and adds only one additional parameter to the normal exponential decay.

The most straightforward value fitting procedure is the fitting of I(−1V) and I_{SC} because of their direct relation to the generated charge. The stretched exponential is changed by applying the natural logarithm on equation 2.5. Now it is possible to isolate the parameter t (Eq. 2.5).

$$\mathrm{I_{SC}(t)} = \mathrm{I_{SC}(t_0)exp}\left(-(\mathrm{t}/\tau)^{\beta}\right) \tag{2.26}$$

$$-\tau ln\left(\frac{\mathrm{I_{SC}(t)}}{\mathrm{I_{SC}(t_0)}}\right)^{1/\beta} = t \tag{2.27}$$

The time for the I_{SC} decay to a certain value can be calculated by using 50 % of its initial value, as follows:

$$t_{\mathrm{H}} = t(\mathrm{I_{SC}} = 0.5\mathrm{I_{SC}(t_0)}) = -\tau\mathrm{ln}\left(\frac{\mathrm{I_{SC}(t_0)/2}}{\mathrm{I_{SC}(t_0)}}\right)^{1/\beta} \tag{2.28}$$

$$t_{\mathrm{H}} = \tau\left(-ln(0.5)\right)^{1/\beta} \tag{2.29}$$

25^{o}C is the standard temperature used for solar cell characterization according to standard reporting conditions [241]. Using t_{H} as time to half of the initial value, the acceleration factor at a given temperature T is given by:

$$k(T) = \frac{t_{\mathrm{H}}(25^o\mathrm{C})}{t_{\mathrm{H}}(T)} \tag{2.30}$$

Since a stretched exponential is used for the transient fits, τ cannot be used directly to determine the acceleration factor. However, the following procedure can take the stretching exponent β into account: The activation energy is defined as:

$$E_{\mathrm{A}} \equiv -\mathrm{R}\frac{\partial\mathrm{ln(k)}}{\partial(1/\mathrm{T})} \tag{2.31}$$

R is the ideal gas constant. This can also be written as (See Appendix 8.1 for more details):

$$k = Aexp(-E_{\mathrm{A}}/RT) \tag{2.32}$$

substituting 2.30 in 2.32

$$\frac{t_{\mathrm{H}}(25^{o}C)}{t_{\mathrm{H}}(T)} = Aexp(-E_{\mathrm{A}}/RT) \tag{2.33}$$

making $A' = A/t_{\mathrm{H}}(25^{o}C)$, one can write

$$t_{\mathrm{H}}(T)^{-1} = A'exp(-E_{\mathrm{A}}/RT) \tag{2.34}$$

For temperature accelerated measurements, one can calculate the activation energy with equation 2.35.

$$E_{\mathrm{A}} = -\mathrm{R}\frac{\partial \mathrm{ln}(\mathrm{t}_{\mathrm{H}}^{-1}(\mathrm{T}))}{\partial (1/\mathrm{T})} \tag{2.35}$$

The stretched exponential is used to fit the measured quantities and determine the t_{H} of I_{SC} and I(−1V). An Arrhenius plot using equation 2.35 is used to determine the activation energy E_{A}.

2.6 Derivations from spectrum

The spectral responsivity (R(λ)) and, consequently, the wavelength resolved external quantum efficiency (EQE) are important parameters in solar cell characterization. The EQE shows which part of the incident irradiance is converted into electric current and how efficient this process is. It is of major importance to distinguish the photon flux ($\partial\Phi$) derivated from $\partial\Phi/\partial E$ from the photon flux derivated from $\partial\Phi/\partial\lambda$, as the measured quantity normally follows in wavelength (λ) but integration in the energy (E) spectra is sometimes needed. The conversion is given by equation 2.36.

$$\frac{\partial\Phi}{\partial E} = \frac{\partial\lambda}{\partial E}\frac{\partial\Phi}{\partial\lambda} \tag{2.36}$$

2.6.1 External Quantum Efficiency

The external quantum efficiency (EQE) is measured against a calibrated photodiode. The short circuit photocurrent of the sample for each wavelength, $\mathrm{I_{SC}}(\lambda)$, and the short circuit current of the photodiode $\mathrm{I_d}(\lambda)$ are measured in parallel. The responsivity R of the photodiode is known.

Using irradiance $Irr(\lambda) = \mathrm{I_d}(\lambda)/R(\lambda)$, the photon energy $\mathrm{E_{ph}} = \mathrm{hc}/\lambda$, and the responsivity of the photodiode $R(\lambda)$, the number of photons (per time) can be defined as:

$$\mathrm{Nr_{ph}} = \frac{\mathrm{I_d/R}(\lambda)}{\mathrm{E_{ph}}} \tag{2.37}$$

Being the number of electrons (per time):

$$\mathrm{Nr_{el}} = \frac{\mathrm{I_{SC}}}{\mathrm{q}} \tag{2.38}$$

The EQE is:

$$EQE(\lambda) = \frac{\mathrm{Nr_{el}}}{\mathrm{Nr_{ph}}} = \frac{\mathrm{I_{SC}}(\lambda)/q}{\frac{\mathrm{I_d}(\lambda)/R(\lambda)}{\mathrm{E_{ph}}}} = \frac{\mathrm{E_{ph}}}{\mathrm{I_d}(\lambda)/\mathrm{R}}\frac{\mathrm{I_{SC}}(\lambda)}{q} = \frac{R\mathrm{E_{ph}}}{\mathrm{I_d}(\lambda)}\frac{\mathrm{I_{SC}}(\lambda)}{q} \tag{2.39}$$

for each wavelength:

$$EQE(\lambda) = \frac{\mathrm{I_d}(\lambda)\mathrm{q}}{R(\lambda)\mathrm{E_{ph}}(\lambda)\mathrm{I_{SC}}(\lambda)} = \frac{\mathrm{I_d}(\lambda)\mathrm{q}\lambda}{R(\lambda)\mathrm{I_{SC}}(\lambda)\mathrm{hc}} \tag{2.40}$$

For the total efficiency measured under the Sun simulator, one has to keep in mind that the simulated spectra do not match the standard spectra (e.g. AM1.5) and a correction of the short circuit current must be made by a mismatch factor [242, 243].

2.7 Impedance equations

The equations used to convert complex electric quantities are shown in table 2.7. The measurements were done by an HP4284A LCR meter, R (Resistance) and X (Reactance) are used as primitives for simplicity only, the measurement itself is done in an angular space.

The equivalent circuit of one capacitor in series with one resistor is used to extract the capacitance

Symbol	Name	Definition
R	electrical resistance	primitive (measured value)
X	electrical reactance	primitive (measured value)
Z	electrical impedance	$\mathrm{Z} = \mathrm{R} + i\mathrm{X}$
$\lvert\mathrm{Z}\rvert$	Module of impedance	$\lvert\mathrm{Z}\rvert = (\mathrm{R}^2 + \mathrm{X}^2)^{1/2}$
θ	phase of Impedance	$\theta = arctan(\lvert\mathrm{X}\rvert/\mathrm{R})$
Y	electrical admitance	$\mathrm{Y} = 1/\mathrm{Z} = \mathrm{G} + i\mathrm{B}$
G	electrical conductance	$\mathrm{G} = \mathrm{R}/(\mathrm{R}^2 + \mathrm{X}^2)$
B	electrical susceptance	$\mathrm{B} = -\mathrm{X}/(\mathrm{R}^2 + \mathrm{X}^2)$
$\lvert\mathrm{Y}\rvert$	Module of Admitance	$\lvert\mathrm{Y}\rvert = (\mathrm{G}^2 + \mathrm{B}^2)^{1/2} = 1/(\mathrm{R}^2 * \mathrm{X}^2)$
ϕ	phase of Admitance	$\phi = -arctan(\lvert\mathrm{X}\rvert/\mathrm{R})$

Table 2.5: Name of variables and mathematical relations used in impedance calculations.

of the device with Eq. 2.41. The parallel resistance is calculated with the equivalent circuit of one resistor and one capacitor in parallel (Eq. 2.42).

$$C_S = \mathrm{Y}/2\pi\nu \tag{2.41}$$

$$\mathrm{R}_{sh} = 1/\mathrm{G} = -(\mathrm{R}^2 + \mathrm{X})/\mathrm{X} \tag{2.42}$$

2.8 Laser desorption/ionization time of flight mass spectrometry

Mass spectroscopy is an important tool for characterization of molecules and impurities. A feature is its high sensitivity for very low concentrations. Its basic function principle is to ionize the molecules from a gas/vapor state and accelerate them by an electromagnetic field. The measurement is done by counting the number of events in a ion/mass analyzer, such as a time of flight analyzer [244].

Laser ablation can be used to create a vapor of non volatile molecules, in this case the method is called laser desorption / ionization time of flight mass spectrometry or simply LDI-TOF. Most comonly is the matrix assisted LDI-TOF or MALDI-TOF. The matrix is composed of a material with large volatility, which will not react chemically with the guest material. This enables the use of lower laser power and consequently less fragmentation of the molecules is caused by the laser shot. The matrix has a high absorption of the laser emission and transfer part of its charge to the guest molecule enabling it to be accelerated for the measurement. Since the charge transfer from the matrix to the guest molecule is different for each molecule, the acceleration for each mass will be different. Consequently, the number of counts cannot be used in a direct quantitative analysis.

In this work, LDI-TOF is used directly to analyze the sample. This tool enables to record a direct fingerprint of the molecules in the sample without any external interference. The drawback is that for some material combinations, the matrix effect is not so efficient, i.e., one of the materials in the sample has to work as a matrix. In this case, higher laser intensities are needed which may fragment the molecules to be analyzed. A measurement of a sample will then always need a comparative measurement of a reference and the analyses of fragments caused by the method itself.

Further details of the technique are available in the work of Scholz et al [244]. The LDI-TOF measurements in this work were performed by Dr. S. Scholz.

Chapter 3

Long time measurement equipment

Solar cells must be robust against Sun irradiation and must withstand relatively high temperatures for many years[1]. The ultimate goal of lifetime measurements of solar cells is to have accelerated measurements that correspond to aging on site and to also have measurements under real conditions, as a reference. Long time measurements under accelerated conditions are required to record the aging behavior of solar cells. Specific laboratory conditions are necessary to facilitate the investigation of the aging dynamics of solar cells such as controlled temperature and irradiance. A high quality set of measured data is needed to enable good fittings of decay equations which in turn also enables the calculation of the lifetime by extrapolation (see section 2.5). This, and the need to measure many solar cells at the same time, motivated the construction of the measurement equipment that will be described in the following text.

A circuitry was developed to provide a stable illumination source, temperature control, and a relay switcher to address all devices on one substrate (see Fig. 3). The word substrate or sample means a glass plate with four individual solar cells on it, also called devices. The analog output of each circuit is either directly connected to the device under test, or it is open circuit. This allows the connection of several circuits in parallel. The measurement itself is carried out by an external source-measure unit (Keithley SMU 2400); the "common to all" measurement equipment is necessary to provide comparative measurements. Nevertheless the developed equipment is called measurement box or just box.

Temperature variations can easily occur by using a solar simulator. The temperature of the sample can be stabilized with a PID (proportional-integral-derivative) temperature controller. The measured

---

[1] A solar cell can easily achieve temperatures as high as 70 ^oC [245].

data will still have oscillations due to changes in the temperature of the sun simulator caused by ambient temperature fluctuations.

All high power control is made with linear circuits. Despite larger heat dissipation, this was chosen on purpose to simplify the circuitry, and since the currents are high, to avoid electromagnetic interference on the measurements. If the light intensity is recorded parallel to the main measurement using a reference diode, one can do small corrections on the solar cells photocurrent. Still, the data cannot be well fitted [142], and the correction of the whole I *vs.*V curve is more complicated.

3.1 Light source

There are short, medium, and long term stability issues with normal Sun simulators. Commercial Sun simulators are usually gas discharge lamps, especially Xe lamps, because they can provide a high temperature spectrum, and consequently better match the solar spectrum. The Sun has approximately a black body spectrum of 5800 K. Normally, gas discharge lamps are operated in AC to avoid electrophoresis of the electrodes[2]. The oscillation of the lamp will not represent a problem in a measurement if the integration time is chosen to be greater than several arc discharge cycles. Sun simulators with passive heating by simple convection (in our case) require some time to stabilize their internal temperature. If a stable ambient temperature is provided, then the sun simulator should have a stable light intensity output after operating for 30 minutes. Due to the high operation temperature, the electrodes slowly evaporate on the glass bulb causing a drop in illumination and a lowering in the discharge current, which is caused by a widening of the electrode gap, the latter can be ignored. The nominal lifetime of a typical 150 W Xe lamp in a sun simulator is about 1000 h.

In the setup constructed for the experiments, light emitting diodes (LED) were chosen as illumination sources. The main advantages are high efficiency and high integrability. The main drawback is that the emission spectra do not resemble a Sun spectrum. The LED emission is very narrow and limited to one color. White LEDs have a broader emission spectra, but still not a black body spectrum, and it is not flat even in the visible range. Figure 3.2 shows the spectra of several LEDs used in this work.

Blue LEDs are used in most experiments, due to their relatively high photon energy (around 2.67 eV). It is expected to more easily activate photochemical processes by using blue rather than red or green

---

[2] this is the case for long time operation, see, for example, the user specification of a Newport Catalog 6035 Hg(Ar) Lamp.

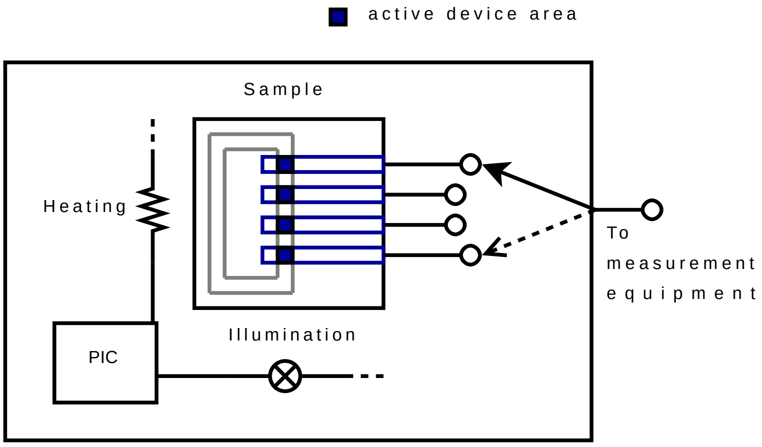

Figure 3.1: Schematic overview of the developed circuitry emphasizing the user requirements, which are: temperature control, illumination control, and the ability to select the device under test. The measurement itself is done by an external source-measure unit.

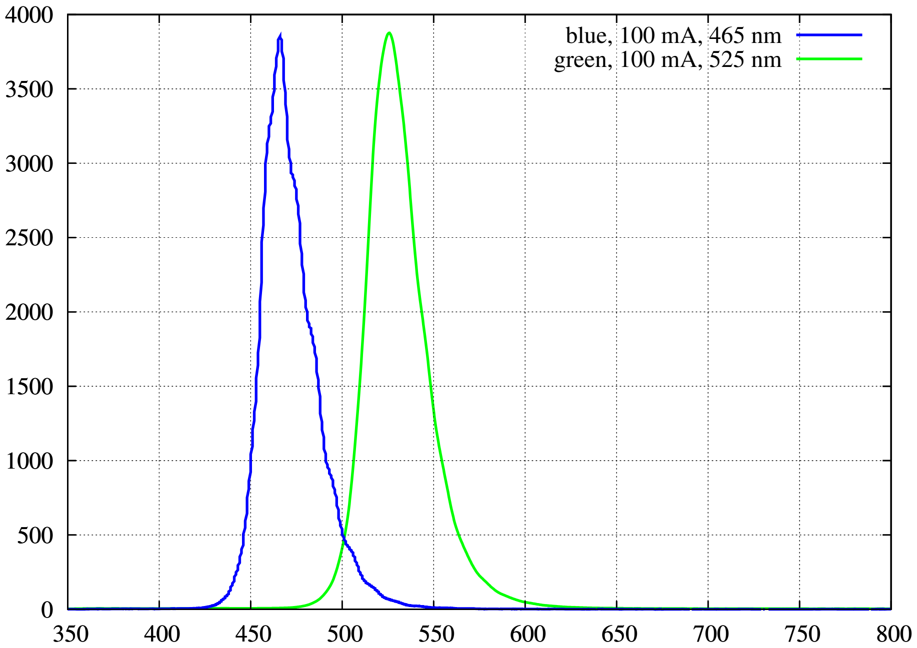

Figure 3.2: Spectrum of the blue LEDs Luxeon LXHL-DB02 used as light source. The green LED LXHL-PM02 is shown for comparison.

LEDs. The emission is also in the absorption range of one of the studied materials (C_{60}). In this work, we try to achieve a photocurrent in the same order of magnitude as we would achieve it under AM1.5 Sun spectra. There must be a compromise between LED irradiance (radiometric power) and LED lifetime. UV LEDs would be preferred, but at the moment commercially available UV LEDs cannot fulfill this compromise.

White LEDs are blue LEDs with a converter layer on top, they may have a shorter lifetime resulting from the phosphorescent converter layer, and they may show a change in spectra upon aging. This depends obviously on the operation conditions. For this reason, in the present work, 1 W LXHL-PB01 Blue (nominal emission peak at 470 nm) high power LEDs were used. They have a junction to case thermal resistance of 15 ^{o}C/W. As soon as available on the market, the 5W LED version was used (Luxeon LXHL-DB02). It has a lower thermal resistance of 8 ^{o}C/W due to its larger active area. The big advantage of using a higher power LEDs is that they can be driven at lower current densities with equal irradiance output as the lower power versions (i.e., they work under lower junction temperature and live longer).

Providing an active cooling of the LEDs (shown in detail in figure 3.3), it was possible to have no significant (in some cases not even measurable) degradation of the blue 5W LEDs during the measurements in this work. It is still necessary to emphasize the importance of the active cooling. It avoids the necessity of any correction of the measured data due to decreasing incident irradiance.

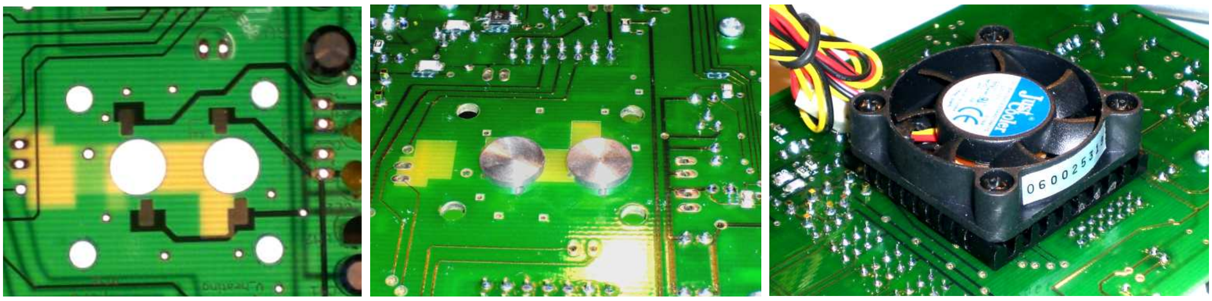

Figure 3.3: From left to right: top view of the connections for the high power LEDs showing the holes for the heat sink cylinders; bottom view with the aluminum cylinders in place; bottom view with the complete heat sink and the ventilator.

To achieve the required irradiance, the light of the LEDs is further concentrated on the sample with a plastic lens[3]. Since the LED + lens set is quite large, only two LEDs are placed under the sample, is such a way that the outer two devices of the four devices get the highest light intensity.

---

[3] Carclo-Optics Nr. 10034. Datasheet available at www.roithner-laser.com (02.2008)

With this setup it was possible to reach the photocurrent of an equivalent to 3 Suns using white or red LEDs in C60:ZnPc organic solar cells. For almost all experiments, a modest intensity of around 10 mW/cm^2 was used with the 1 W Blue LEDs and 60 mW/cm^2 with the 5 W version. The power of the LEDs was measured with a calibrated photometer (Thorlabs PM100), and a metal mask to define the illuminated area.

3.2 Current source for the LEDs

To drive the LEDs, currents between 100 mA to 500 mA were used and three types of power supplies were tried out. A linear, constant voltage power supply with gain feedback from a reference diode was tested. It showed good linearity, but the calibration was very time consuming. Instead a constant current source based on a commercial linear regulator LM317 was used in all experiments. The circuit is basically as in figure 3.4, the current can be set by changing the resistor (R), by I_D=1.25 V / R. The circuit was made with 4 resistors connected, via a dip-switch, in parallel. This way the user can select the appropriate combination of resistors to get the desired current value. On the last circuit version (Fig. 3.5), the power supply was exchanged to a bipolar amplifier and the voltage is controlled by a 16 bit digital to analog converter (DAC). With this digital control it is possible to adjust the output to keep a constant illumination over the entire experiment. Besides it is also possible to dim the light source in order to make light intensity measurements. The transistors and the resistors in series need a metal cooling block to dissipate the generated heat.

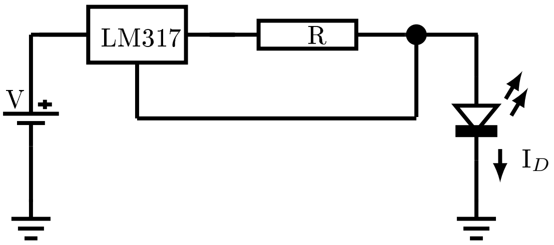

Figure 3.4: Schematic of the constant current source. The current I_D is given by I_D=1.25 V / R. The LM317 will always keep the voltage drop over the adjusting resistor R at 1.25 V.

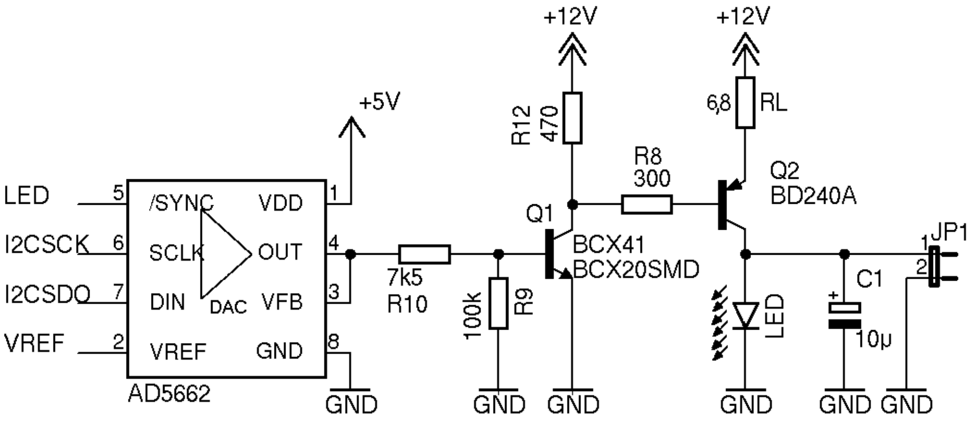

Figure 3.5: Schematic of the digitally controlled power source for the LED. The digital to analog converter ha 16 bits and is the first stage to the linear amplifier constituted by Q1 and Q2. RL is necessary to limit the current, due to the high supply voltage it is rated to a high power. The LED needs about 6 V to operate. JP1 can be used to drive an external light source (in this case the LED has to be removed).

3.3 Temperature control

The temperature control consists of a heater and a thermometer. The heater consists of a linear amplifier that uses a bipolar transistor controlled by a 16 bit DAC. A metal cooling block is absolutely necessary for the bipolar transistor. An ITO coated glass plate is used as a heating element, it is in direct contact with the sample substrate. It is important to choose an ITO coated glass with the correct resistance (about 15 Ω/□ in our case) such that the voltage and the current needed to achieve the necessary power are not too high. The variations in the transistors gain and on the heating element resistance requires an individual calibration for each circuit.

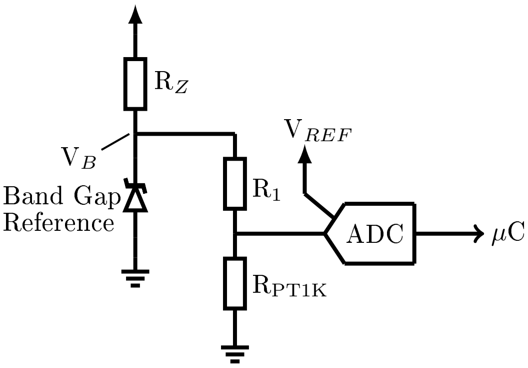

Figure 3.6: Temperature sensor circuit. The resistor divisor is formed by R_1 and the platinum resistor with resistance R_{PT1K}. R_1 is 1 k Ω, and the probe current is aproximately 0.5 mA. The band gap reference (LT1029) guarantees 5 V supply voltage. R_Z is 470 Ω.

The thermometer consists of a 1 kΩ Pt resistor (PT1000[4]) in series with a low thermal coefficient 1 kΩ resistor. The PT1000 is connected to the samples surface as close as possible to the center. The voltage drop over the reference diode is converted by a 24 bit digital to analog converter (DAC), the probe current is given by 5 V / 2 kΩ = 0.5 mA. The Callendar - Van Dusen equation (Eq. 3.1) is used to calculate the temperature from the resistance of the PT1000.

$$\mathrm{T} = \frac{\mathrm{R_0A} + \sqrt{\mathrm{R_0^2A^2} - 4\mathrm{R_0B}(\mathrm{R_0} - \mathrm{R_{Pt1k}})}}{2\mathrm{R_0B}} \tag{3.1}$$

The resistance of the PT1000 ($\mathrm{R_{PT1K}}$) is given by

$$\mathrm{R_{PT1K}} = \frac{\mathrm{V_{ADC}R_1}}{\mathrm{V_B} - \mathrm{V_{ADC}}} \tag{3.2}$$

and the voltage drop over the PT1000 (voltage read by the ADC, $\mathrm{V_{ADC}}$) is:

$$\mathrm{V_{ADC}} = \mathrm{N_{ADC}V_{REF}/C_{ADC}} \tag{3.3}$$

where $\mathrm{V_B}$ is the supply voltage, $\mathrm{R_1}$ is the resistance of the constant resistor in series with PT1000, and $\mathrm{V_{REF}}$ is the reference voltage of the ADC. $\mathrm{N_{ADC}}$ is the number given by the ADC, and $\mathrm{C_{ADC}}$ is the ADC conversion factor defined by the eq. 3.3. Used values are $\mathrm{A} = 3.81 \times 10^{-3}$; $\mathrm{B} = -6.02 \times 10^{-7}$; $\mathrm{V}_B = 5$ V; $\mathrm{V_{REF}} = 5$ V; $\mathrm{R_1} = 1000\ \Omega$; $\mathrm{R_0} = 1000\ \Omega$; a typical value for the $\mathrm{C_{ADC}}$ is 16.67×10^6 considering 24 bits resolution. A very good temperature control was achieved with this setup (see figure 3.7).

3.4 Signal connections

The analog bus could be constructed with solid state switchers or with electromechanical relays. Solid state switchers do not have a high enough linearity and will also have parasitic voltages. An advantage of the solid state analog switchers is the high integration, but due to the many drawbacks, they are only suitable for four point measurements. The analog bus of the measurement boxes was constructed with electromechanical relays. Relays have a small contact resistance, and more important, they have ohmic contacts without any parasitic voltage, absolute necessities for accurate measurements. The bus consists

---

[4] Heraeus Sensor-Nite GmbH, M-FK1020 32208286, DIN EN60751 Class B

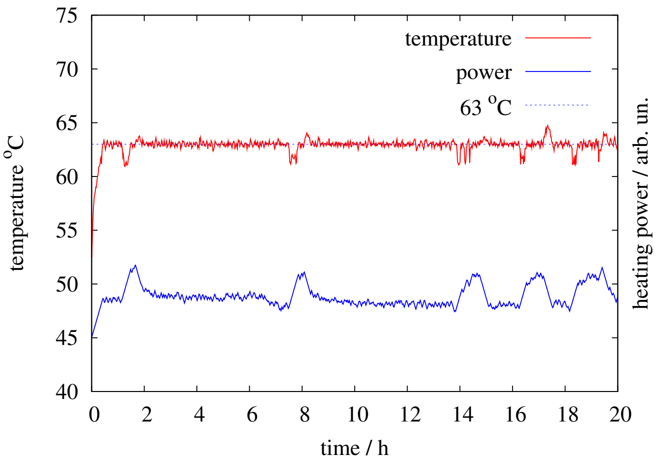

Figure 3.7: Temperature of the sample holder in the measurement circuit without case. Set-point is 63 °C. The blue curve is the heating power. A proportional controller with constant error and a high time constant is implemented in the microcontroller for the temperature control. The peaks in the blue curve corresponds to the time during which the laboratory cooling system is active.

of 6 miniature relays[5] with double switches. Four relays are connected to the 4 devices. The other 2 are for reference photodiodes, each one for each LED. The driver circuit is a TTL demultiplexer (74HC237D) connected to a darlington array (ULN2003AD), granting that only one relay is closed at one time or all are disconnected if the tri-state mode is selected (all relays open).

The normally closed (N.C.) contact of the relays are accessible on jumper pins. They can be used to access the device if it is not under measurement, e.g. to apply a bias on the device.

3.5 Digital I/O and firmware

All digital control of the temperature sensor ADC, heating and lighting DACs, and the relay switcher is done by a microchip 16F628 microcontroller (16F877 on newer versions). The communication with the PC is done with a serial (RS232) to USB interface (FTDI RL232), the RS232 signal is galvanically insulated from the circuit (the used version were still used without the galvanic insulation, see Fig. 3.8). The firmware is written in embedded C (SDCC [246]).

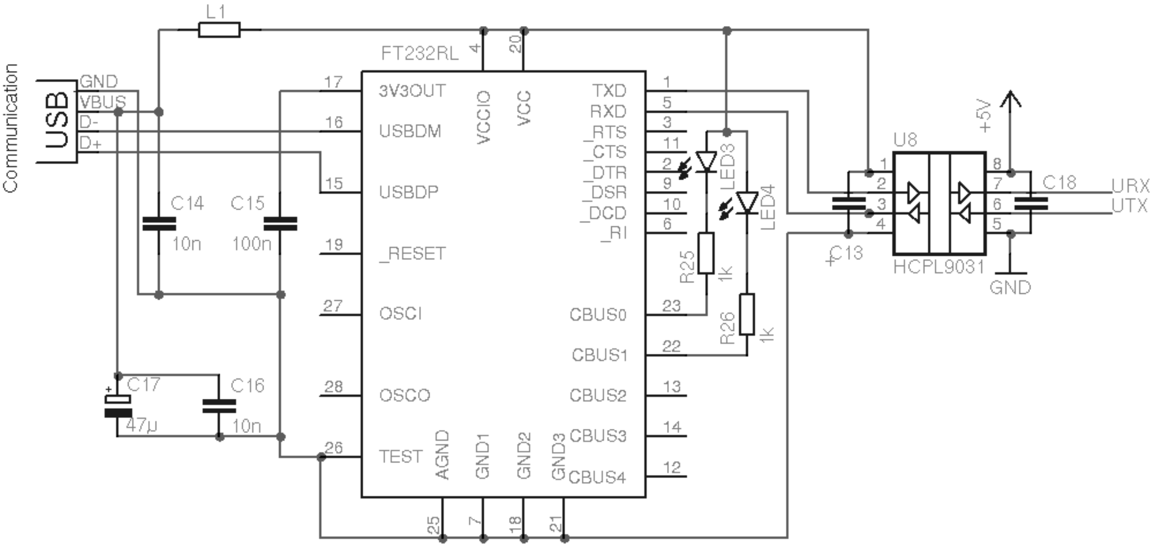

Figure 3.8: Schematic of the galvanically decoupled USB communication interface. The main component, FT232RL is an USB to RS232 logic converter. The signal is galvanically insulated, in both directions, by the HCPL9031. The microcontroller is connected to the signals URX and UTX.

3.6 Software

The software (*scmeas*) is mainly written in C++. An overview of it is given by the flow chart in figure 3.9. The operation consists in cycling through the boxes list, and for each one, select one device after another and do a sequence of measurements (some library names are included for reference). The measurements are implemented in the library *ivmeas* and executed from the file *mainloop*. The communication to the box is implemented in *ltbox*, and the communication to the SMU in the library *instr*.

3.7 Measurement of I *vs.*V transfer curve and tracking parameters

The automatic I *vs.*V data acquisition is configured to read current values for 221 voltage points applied in the range of -1.1 V to +1.1 V, doing an average of 4 measurements and a delay of 1 s. Parameters such as FF, V_{OC}, I_{SC}, and $I(-1V)$ are extracted directly from the I *vs.*V data if found, otherwise the linear interpolation of the two nearest limits is used. Only a few I *vs.*V curves are taken to avoid stress of the device under test caused by the I *vs.*V measurement. A direct measurement of the characteristic parameters is taken with a higher frequency.

---

[5] OMRON, G6K-2P 5V, Latching time < 3 ms; electrical life expectancy $> 10^5$ operations; contact resistance $< 100\ m\Omega$.

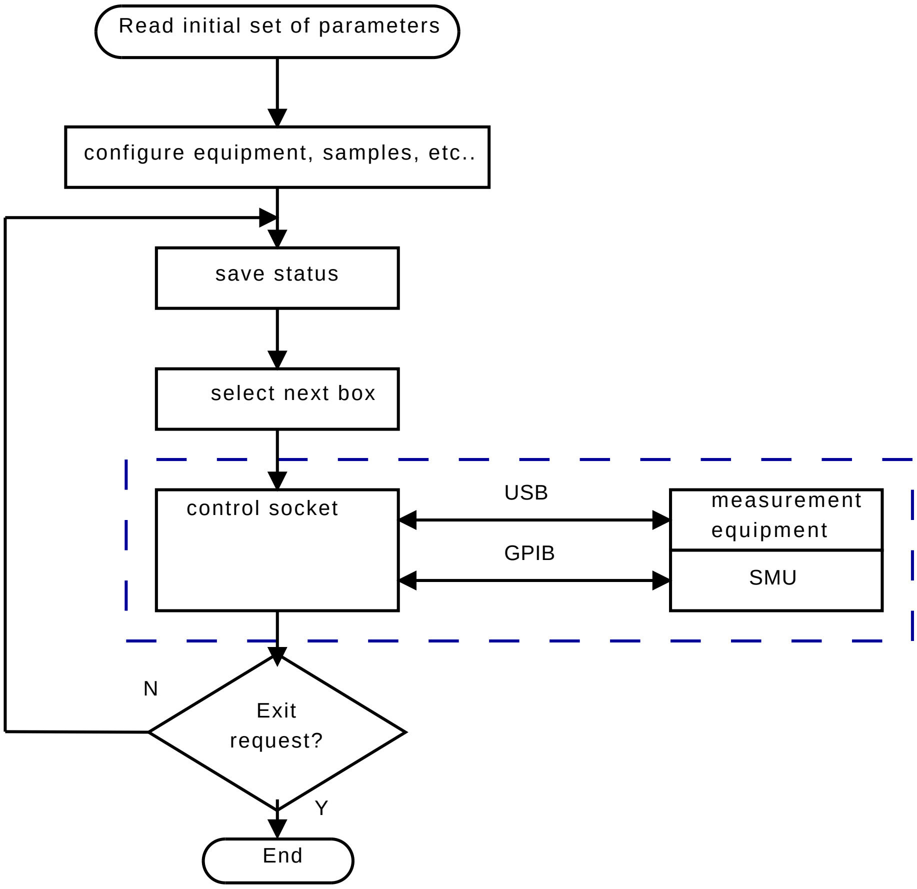

Figure 3.9: Overview flow chart of measurement software (scmeas). The configuration file is read at start, all hardware is configured, one box is selected and the measurement is started. All measurement code is written in the measurement socket (file mainloop.cpp). It uses self written libraries to communicate with the SMU and the developed hardware. After finishing all measurements (all 4 devices of one sample), the next box is selected and measured, after the last box, the first one is measured again, and so on, until the user does an exit request.

The direct measurement of I_{SC}, $I(-1V)$, and V_{OC} is done with the current meter and volt meter options of the SMU. The maximum power point is tracked by a successive approximation algorithm, the starting values are between 0 V and V_{OC}. They are divided into two regions [0;V1] and [V1;V_{OC}] (V1=(V_{OC} +0)/2), the power of the middle point of both regions is compared, the region with the highest power is selected and again divided into 2 regions, and so successively until (Power_n / Power_{n-1} - 1) $<$ 0.0002 or 32 iterations (resolution bits) are achieved.

Figure 3.10 shows the normalized decay of FF, I_{SC}, and V_{OC} of an organic solar cell comparing the values obtained from the I *vs*.V curve with those measured by the alternate method just described. The agreement is very good, as expected.

3.8 Summary and outlook

An equipment was designed and implemented to accomplish the batch measurement of solar cells. This equipment is used to select the device to be measured. In parallel, it controls the aging conditions of the device. The long time measurement equipment is composed basically by a sample holder, a temperature logger and a heating driver, an illumination source with the respective electrical drivers, a microcontroller, the analog channel switchers, and the digital communication interface.

A stable illumination source was achieved with inorganic LEDs driven by a constant current sources, and monitored by photodiodes. The heating was provided by the power dissipated over an ITO coated glass substrate driven by a linear bipolar amplifier. The temperature control was implemented in the microcontroller.

A software package was developed to calibrate the new equipment, to control the parameters of the device aging, to effectively realize the measurement, and finally to manage the acquired data. For this purpose many languages are used in different levels, C++ (GPP), embedded C++ for microcontrollers (SDCC), Python, gnuplot script, and bash. The higher levels are used for the final data processing.

All components were successfully developed until the functional level described in this section. Two systems were integrated with several of the developed equipments, a Keithley source measure unit to execute the measurements, and the software to control the database of the devices in the batch and their respective measurement results.

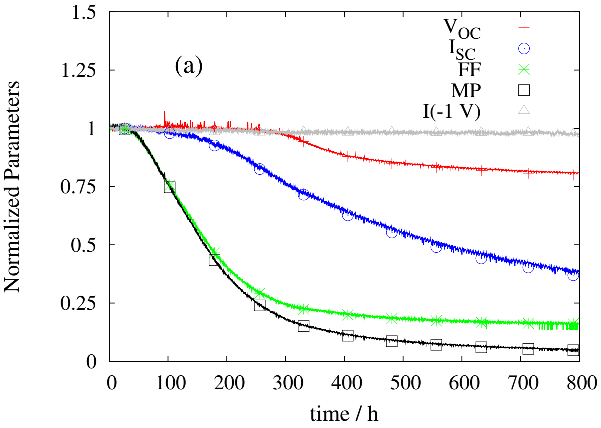

Figure 3.10: Comparison of characteristic electrical parameters of an organic solar cell taken with two different methods: lines are the parameters taken by tracking method, with 880 points per 100 h, the points are data extracted from I *vs.*V *curves, with 18 points per 100 h.*

An optional adapter for measuring EQE under selected wavelengths in situ was projected but not implemented.

For further development, the following issues have to be considered: The linear power sources for the LEDs and the heating should be modified to use MOSFET transistors. The sample socket should be further modified to facilitate its use, i.e. direct connection of the sample by mechanical spring connections and a standard heating transistor to simplify the calibration procedure. The equipment should be constructed on a rack mount to facilitate integration in larger systems. A microcontroller with larger memory will enable more functions to be integrated in it (for example, self calibration), simplifiying the main control software. The software needs a graphical user interface, it was not necessary for the experiments but can easily be written to set the parameters in the existing database.

Chapter 4

Aging of ITO / ZnPc / C_{60} / Al solar cells

Of the so called small molecules solar cells, the most frequently realized by now are those which combine fullerene and phthalocyanines. Fullerene C_{60} is the preferred choice for the acceptor due to its high exciton diffusion length, high electron mobility, low LUMO, relatively high stability, and relatively high absorption in the blue spectral range. The combination with a phthalocyanine is interesting because the relative HOMO / LUMO offset favors the excitonic separation from both materials at their interface. Most of the phthalocyanines have a very high absorption in the visible, and from those, CuPc and ZnPc are the most stable compounds.

The highest photoelectric conversion efficiency values obtained from the small molecule solar cells are from phthalocyanine - C_{60} heterojunction devices. Many different device architectures were shown in literature, for instance: flat heterojunctions, bulk heterojunctions, graded junctions, bulk heterojunctions with controlled morphology [247], and mixed devices with specially controlled interfaces [163].

It is known that the characteristic of bulk heterojunction devices is strongly dependent of the morphology of the blend [123, 248]. There is a strong dependence of the device performance on substrate temperature during deposition. For this reason, a very simple device structure, with the most simple flat heterojunction interface was chosen to study its aging behavior. A device with a two layer donor - acceptor heterojunction deposited between two electrodes is not good enough to perform like a typical solar cell, because the interface between organic and inorganic layers usually does not form ohmic contacts. The electronic interface between the electrodes and the organic materials cannot simply be described by the energy levels of the individual materials.

The first two sections concerns the interfaces between C_{60} and Al, and ITO and ZnPc. Special devices were constructed to analyze these interfaces. After that follows the analysis of the long-term aging behavior of organic solar cells based on flat Zinc Phthalocyanine (ZnPc) / C_{60} heterojunctions under controlled conditions. The studied structure is glass / indium tin oxide (ITO) (120 nm) / buffer / ZnPc (18 nm) / C_{60} (52 nm) / buffer (4 nm) / Al (100 nm). Devices are encapsulated with glass and an UV curable sealant. They are aged under controlled temperature and illumination at 475 nm ($30 \pm 7\ mW/cm^2$), leading to absorption mainly in C_{60}. Other characterization such as spectrally resolved external quantum efficiency and mass spectrometry are used to analyse the sample and find the source of degradation.

4.1 Role of the buffer layer between C_{60} and Al

There is still no common sense on how the interface between Al and C_{60} is chemically and physically composed. An electron transfer of $\sim$0.2 electrons from Al to C_{60} was measured by Owens. This result seems plausible [249] because they have deposited the C_{60} and Al layers under a base pressure of $< 1 \times 10^{-7}$ Pa on a GaAs substrate kept at 60 K. Al diffusion in the C_{60} layer is observed at room temperature. This figure is consistent with a n type compensation of C_{60} by Al atoms, but other research groups have observed an improved hole transport on C_{60}:Al mixed layers. This can be attributed to the higher base pressure used durung Al evaporation, at pressures of 1×10^{-4} Pa the oxygen concentration cannot be neglected. It is known from mass spectroscopy that more oxygen is present in C_{60} near the Al interface [148] than in the C_{60} bulk. The same was shown for Al / PCBM / Al devices using EDX measurements (PCBM is a C_{60} derivative) [250]. Furthermore by evaporating Al over C_{60}, the temperature of the surface of the C_{60} layer is usually higher than 300 K. Also low energy electrons are provided on C_{60} from the charge transfer from Al to C_{60}. Some C_{60} molecules can also be excited by the light from the Al evaporation source. If there is already oxygen available in the C_{60} film, it will react with the excited C_{60} molecules as discussed before Sec. 2.1.1. Oxygen reacts with Al as well, at the end one may expect an interface composed of partially oxidized C_{60} and Al.

Aluminum evaporated under normal device fabrication conditions with a pressure around 1×10^{-4} Pa does not form an ohmic contact to C_{60}. More precisely it does not extract or inject electrons efficiently [251–253]. Nevertheless the contact of Al to a mixed layer of CuPc / C_{60} in a bulk heterojunction organic solar cell works reasonably well, with greater photocurrent than without buffer layer, leading to the conclusion that the Al / C_{60} interface also works as exciton quencher [253].

A buffer layer is typically used to overcome those problems. BCP (2,9-dimethyl-4,7-diphenyl-1,10 phenanthroline, CAS Nr. 4733-39-5) or BPhen (4,7-diphenyl-1,10-phenanthroline, CAS Nr. 68399-83-7) are the common materials used in buffer layers [27, 251, 252, 254]. Since these materials have a wide gap compared to C_{60}, and higher lying LUMO as well as deeper lying HOMO, they should, in principle, not form an ohmic contact but act as a perfect blocker. This is, however, not the case. Peumans proposed the creation of gap states in the BCP layer during deposition of the metal [252]. This was confirmed by Toyoshima who measured interface states between BCP and Al using UPS [255].

Due to their wide gap one might use BCP or BPhen as exciton blocker, the triplet energy of Bphen is with 2.5 eV much higher than the triplet energy level of C_{60} (1.57 eV). [252, 253], however, gap states are needed to promote the charge carrier transport between Al and C_{60}. The gap states in turn could serve as excitons quenchers. The fact that CSix / n-C_{60} / Al works identically in a solar cell as a C_{60} / BPhen / Al layer shows that the buffer layer only inhibits the Aluminum diffusion into the C_{60} layer but does not contribute to an increase of the short circuit current and the overall performance of the device. The limitation for the thickness of the BPhen layer can be overcome by doping [120]. Therefore, the ideal electric contact would be, like for the hole contact, an electron transport layer (ETL) that has a wide HOMO-LUMO gap, is transparent[1], and has the same LUMO level as the acceptor. This ETL should also work as exciton blocking layer, like NTCDA (1,4,5,8-naphthalene-tetracarboxylic-dianhydride, CAS Nr. 81-30-1) [256]. Still, NTCDA is not suitable for application at higher temperatures, due to its low glass transition temperature.

The buffer layer is probably a protection against damage caused by the evaporation, this is further supported by the fact that several different kinds of materials can be used as a buffer without significantly changing the device performance, including CuPc and PBD (2-phenyl-5-(4-phenylphenyl)-1,3,4-oxadiazole, CAS Nr. 852-38-07) [251], and Alq_3 (tris (8-oxoquinoline) aluminum (III), CAS Nr. 2085-33-8) [251, 257]. Figure 4.3 shows solar cells made with 2 and 4 nm ZnPc thick buffer layer. The solar cell has a good performance for this structure with FF = 40 %, $V_{OC} = 0.5$ V and $I_{SC} = 6.3$ mA/cm^2 (4 nm buffer layer). Another way to provide charge transport between C_{60} and Al is to use a so called conversion contact, like a tunnel junction in inorganic tandem solar cells. Instead of extracting electrons from C_{60} to

---

[1] means it will have a low extinction coefficient even if it has an absorption tail extend to the visible

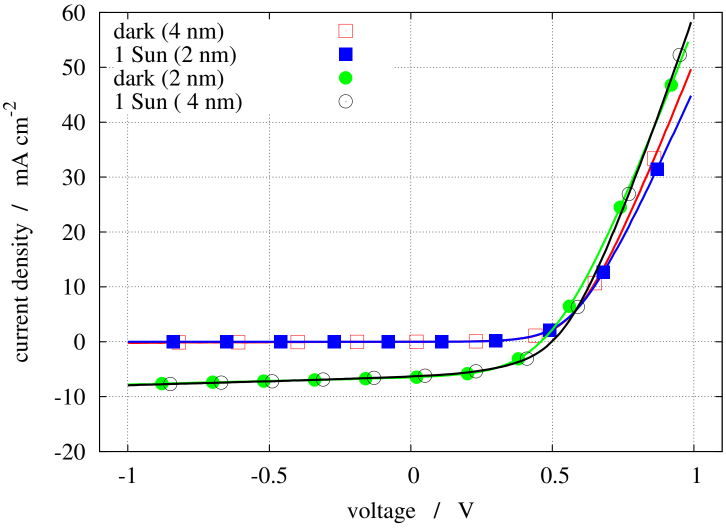

Figure 4.1: Characteristic I *vs.*V *curves of ITO / ZnPc /* C_{60} */ buffer / Al solar cells, using ZnPc as buffer (2 and 4 nm) and ITO treated with oxygen plasma.*

Al, the holes can be injected from Al to another organic material and force an e-h recombination between this material and C_{60} [258, 259].

It is still not fully clear what leads to a blocking contact between C_{60} and Al. Probably several processes are included, the diffusion of Al and the reaction with oxygen. XPS / UPS measurements combined with solar cells measurements with Al deposition in UHV (10^{-9} mbar) and cold substrates can shine some light on this issue.

For the following experiments, ZnPc and AOB:C_{60} fulfill the requirements for providing an ohmic contact between C_{60} and Al in a working solar cell, and ZnPc is thermally stable to temperatures well above 100 °C.

4.2 ITO / ZnPc interface

The ITO used in the experiments does not make an ohmic contact to undoped ZnPc since its work function is as low as 4.4 ±0.1 eV [260]. To create ohmic contacts one can modify the ITO surface by depositing a very thin layer of a strong acceptor. PTCDA (perylene-3,4,9,10-tetracarboxylic-3,4,9,10-dianhydride, CAS Nr. 128-69-8) is a good candidate due to its thermal stability, it works like C_{60} [261], but the effect is not sufficient to provide an efficient ohmic contact between ITO and ZnPc.

Figure 4.2 shows (in red) a I *vs.*V curve of a device with layer structure ITO / ZnPc (20) / C_{60}

(40) / ZnPc (3.5) / Al (100) made with ITO without any further treatment but standard solvent cleaning. As in the Au / ZnPc interface [262], there is a strong dipole layer between ITO / ZnPc forming a barrier for hole injection and extraction. A dipole layer between a HTL and a conductor can be avoided by inserting an acceptor. This was shown in the work with C_{60} [263] and with PTCDA to improve hole injection / extraction between ITO/HTL for OLEDs [264].

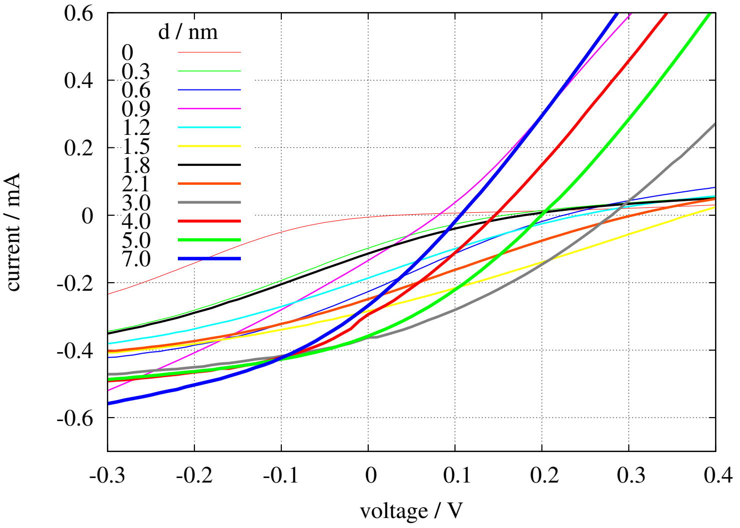

Figure 4.2: Light I *vs.*V *curve of a ZnPc / C_{60} solar cell using PTCDA between ITO and ZnPc to improve the electrical contact. The red curve is the device without PTCDA.*

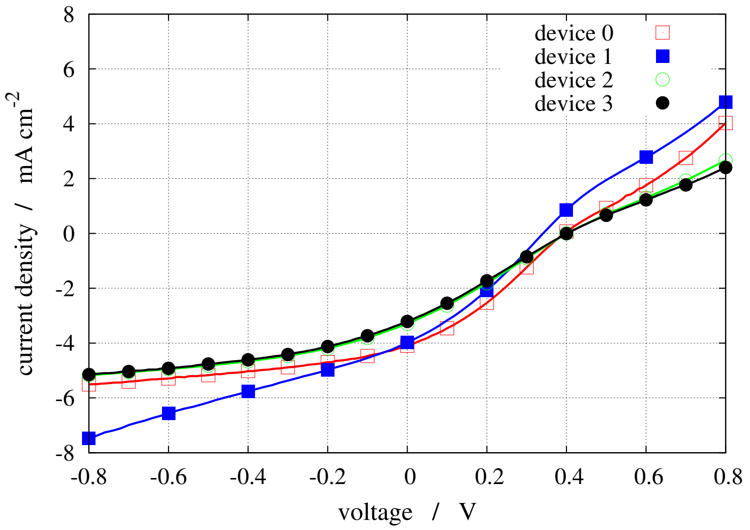

Figure 4.3: ITO / ZnPc / C_{60} / buffer / Al solar cell, using ZnPc as buffer. The ITO is treated with oxygen plasma and further heated in vacuum at 150 °C C for 2 h.

A strong acceptor like F_4-TCNQ between ITO and ZnPc will create a negatively charged layer, by electron transfer from the ITO to the acceptor. The hole in the ZnPc layer can freely recombine with these electrons in the F_4-TCNQ layer or, depending on the field direction, the electrons from the HOMO of the ZnPc can be transferred to the LUMO of the acceptor and to the ITO. The resulting effect is similar as surface states on the conductor, many states in which broad energy levels will favor the charge transport between the conductor and the semiconductor forming an ohmic contact.

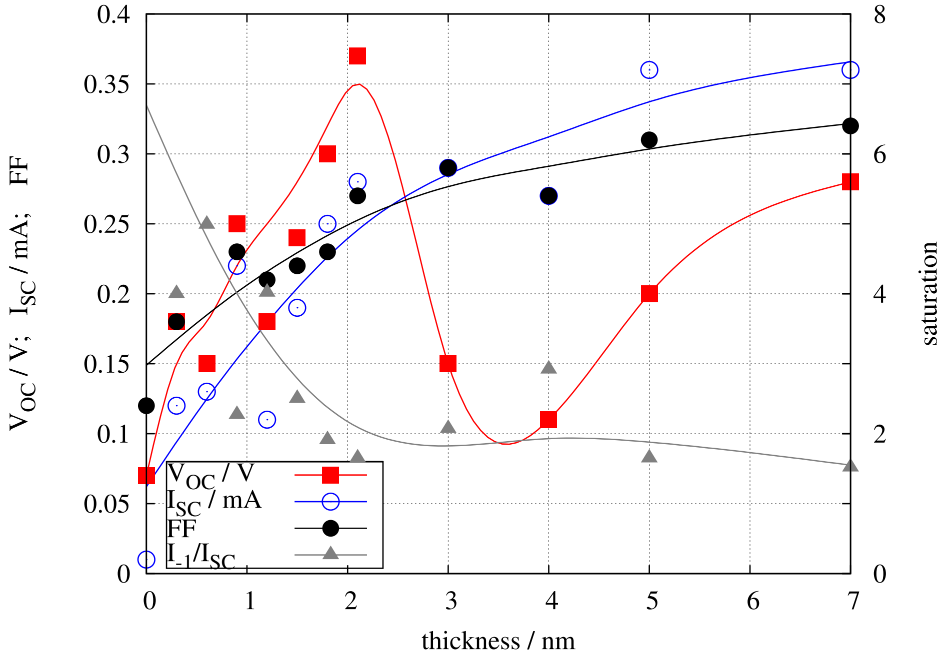

Figure 4.4: Development of solar cell photo-electrical parameters with different thicknesses of PTCDA inserted between ITO (anode) and ZnPc. The lines are guide for the eyes.

The rather low LUMO level of PTCDA [265] is still too high to use it as injection layer (~3.9 to 4.1 eV [266]). Its LUMO is still too high for electrons from the HOMO of ZnPc, at -5.28 eV, to be transferred to the LUMO of PTCDA. The recombination is not high enough, showing only a smaller improvement of the I *vs.*V curve (See Fig. 4.2 and 4.4), still far from the case with stronger acceptors like F_4-TCNQ or NDP2.

Treating the ITO with oxygen plasma also works well as can be seen in figure 4.1. The effect can be partially reversed by heating the substrate in vacuum at 150 °C for 2 h, (Fig. 4.3). The sublimation temperatures around 120 °C for F_4-TCNQ and 160 °C for NDP2. The most stable and stronger acceptor NDP2 was used in the solar cells investigated in this chapter.

Doping the hole transport layer has the same effective effect as using an hole injection layer.

Fig 4.2 shows two I *vs.*V curves of typical p-i-n organic solar cells made with an undoped and a doped hole transport layer, in these samples the ITO surface is not plasma or UV treated.

4.3 Characterization of the ITO / ZnPc / C_{60} / Al samples batch

The aging of several devices, with four modifications of anode and cathode are compared (see table 4.1): using 4 nm ZnPc as a buffer layer (structure A) and using ITO modified with 1 nm Au and 1 nm of the proprietary organic dopant NDP2 [27] (structure B); using 5 nm acridine orange base (AOB) doped C_{60} as a buffer layer (structure C) and using ITO modified with 1 nm Au / and 1 nm NDP2 (structure D). Figure 4.6 shows a general band diagram for the devices and the analyzed structures. These systems were chosen due to their well known standard materials that can lead to reasonable efficiencies [267]. These material sequences are building blocks for p-i-n solar cells, where the thin ZnPc and C_{60} layers are placed into the maximum of the optical field, whose position can be tuned by using transparent transport layers to achieve higher conversion efficiencies [115].

structure	anode	injection	donor	acceptor	buffer	cathode
A	ITO (120)		ZnPc (18)	C_{60} (52)	ZnPc (4)	Al (100)
B	ITO (120)	Au (1)/NDP2(1)	ZnPc (18)	C_{60} (52)	ZnPc (4)	Al (100)
C	ITO (120)		ZnPc (18)	C_{60} (52)	AOB:C_{60} (5)	Al (100)
D	ITO (120)	Au (1)/NDP2(1)	ZnPc (18)	C_{60} (52)	AOB:C_{60} (5)	Al (100)

Table 4.1: List of the four different device structures, the value in brackets is the thickness in nm. The molar concentration of AOB in the AOB:C_{60} layer is 2%.

Figures 4.8, 4.9, 4.10, and 4.11 show the I *vs.*V curves under simulated Sun spectra AM1.5. The characteristic values of all samples can be seen in figure 4.7. Obviously the n-C_{60} layer is not working to its best potential. It was made as thin as the ZnPc layer to enable comparison of the layer thicknesses between the different devices. Either the doping concentration is too low or the layer is too thin. The ZnPc buffer layer is working as expected, giving a FF between 0.4 and 0.52. The ITO surface modification with Au/NDP2 works as well as only using UV treated ITO, the FF is slightly smaller with Au/NDP2 but the I_{SC} and the V_{OC} are higher. The samples with Au/NDP2 also have a better saturation current as shown in the table 4.3:

The origin of the performance difference between devices with (B and D) and without Au/NDP2 (A and C) layer is the contact to the ZnPc layer. An ITO/ZnPc interface where the ITO does not have an oxygen plasma treatment is a blocking contact. After plasma treatment it should work as well as with NDP2.

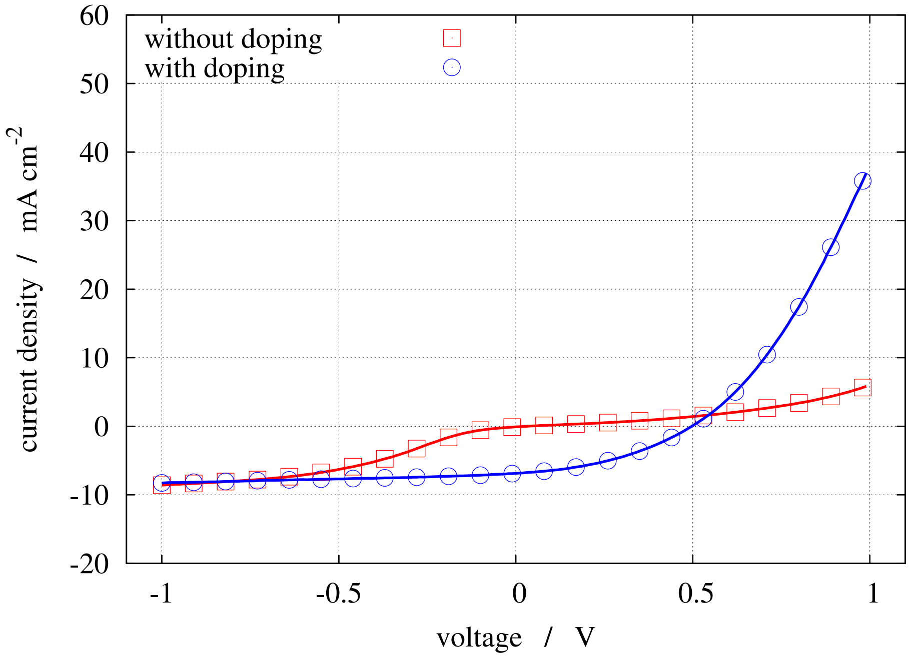

Figure 4.5: Two I *vs.*V *curves of typical p-i-n organic solar cells made with an undoped and a doped hole transport layer.*

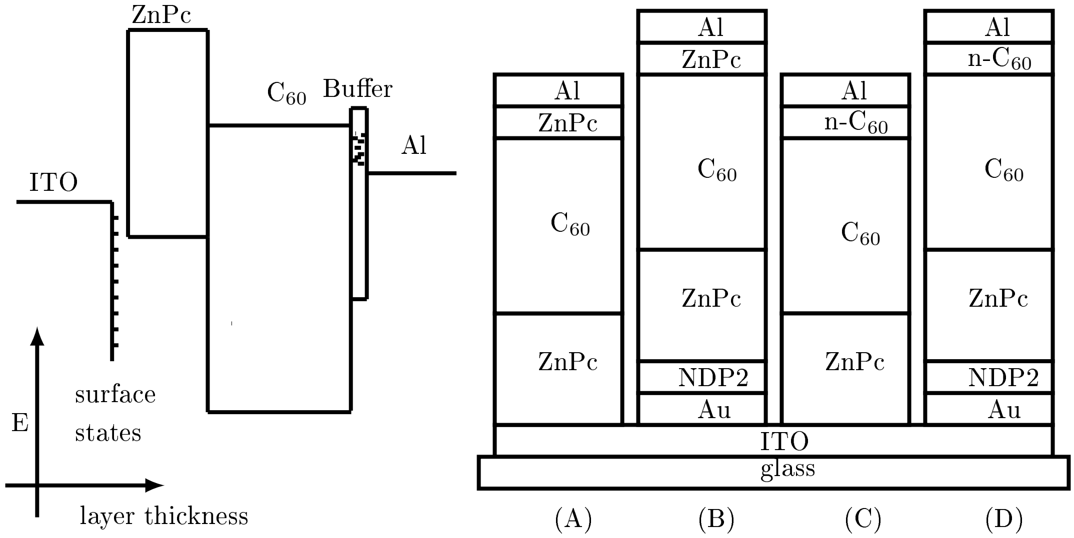

Figure 4.6: Energy diagram (left) of a device made of glass / ITO (120 nm) / ZnPc (18 nm) / C_{60} *(52 nm) / buffer layer / Al (100 nm). On the right hand side the investigated structures are shown. Some samples have additional Au (1 nm) / NDP2 (1 nm) layer (structure B and D). The buffer layers are ZnPc (4 nm) (devices A, B) or AOB doped* C_{60} *(devices C, D).*

4.4 Aging behavior

The following figures 4.8 to 4.11 show the characteristic I *vs.*V curve for each type of device structure. The right side shows the I *vs.*V curve measured under simulated Sun spectra of a sample which is not

structure	V_{OC} (V)	I_{SC} (A)	MPP (W)	FF	S
A	0.54	-4.13×10^{-4}	1.00×10^{-4}	0.45	1.21
B	0.43	-3.52×10^{-4}	7.88×10^{-5}	0.52	1.21
C	0.49	-4.02×10^{-4}	6.47×10^{-5}	0.33	1.31
D	0.39	-3.49×10^{-4}	4.91×10^{-5}	0.36	1.26

Table 4.2: Typical values of 4 samples with different device structures.

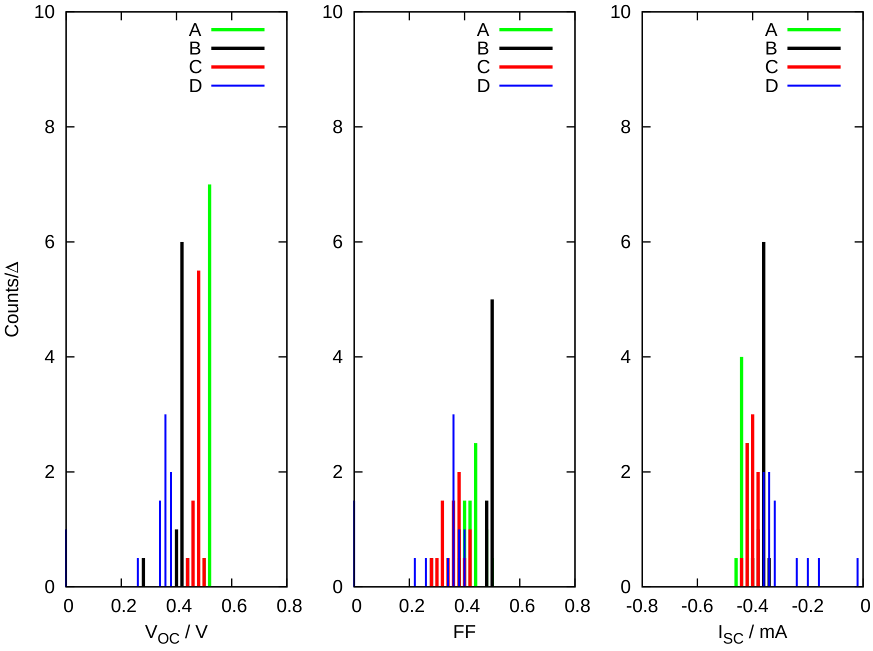

Figure 4.7: Distribution of measured values for V_{OC}, I_{SC} and FF on the wafer with structures A, B, C and D, Δ is always 0.02 with the respective unit.

aged and a sample aged at 50 °C for 1200 h in the developed measurement setup. The graphic on the right side shows the temporal evolution of the characteristic quantities V_{OC}, I_{SC}, FF, MPP and $I(-1V)$. The characteristic quantities are normalized to facilitate the visualization.

Fig. 4.8 shows the measurements for a sample with structure A which has a structure ITO / ZnPc/ C_{60}/ ZnPc buffer / Al. The ITO surface is treated with oxygen plasma and heated for 30 minutes in nitrogen atmosphere under mechanical vacuum before loading in the deposition chamber. The initial I *vs.*V curve has a reasonable good diode shape, after aging the forward current intensity is strongly decreased.

Device B has a structure ITO / Au / NDP2 / ZnPc/ C_{60}/ ZnPc buffer / Al. In the I *vs.*V curve of device B shown in Fig. 4.9 a similar effect as in device A takes place. However, device with structure B shows an increased forward current if compared to device with structure A.

A sample with structure C is used to show the typical behavior of an illuminated sample with a substrate temperature of 50 ± 0.5 ^{o}C. The I *vs.*V curves of the aged devices under AM1.5 simulated Sun spectra are compared in Fig. 4.10. A device, stored in parallel, shows only minor changes in the I *vs.*V curve before and after the experiment. From the normalized transients (Fig. 4.10) one can see the overall behavior of the main extracted parameters. After the fast initial decay, the I($-$1V) appears to reach a constant value (which can further drop if the device encapsulation fails). The t$_H$ of the I($-$1V) is very high, on the order of $\sim 10^5$ h, indicating that chemical reactions with the absorbing centers have almost completely ceased at the end of the measurement.

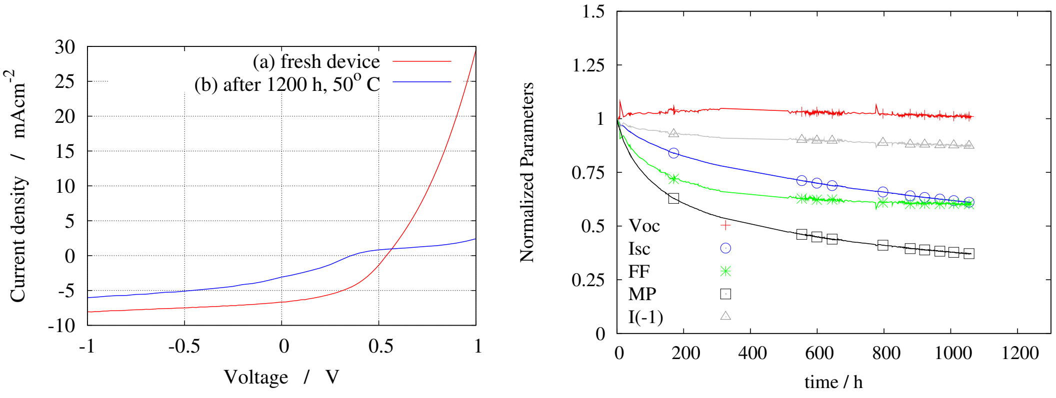

Figure 4.8: Left: Comparison of the I *vs.*V *curves of the devices with structure (A) before and after aging under 50 ^{o}C and the corresponding reference, which was stored in dark.* I *vs.*V *curves were measured under simulated AM1.5 spectrum with an intensity of 100 mW/cm^2. Right: Normalized values of characteristic parameters of a device with structure (A) aged at illumination of 475 nm and temperature of 50 ^{o}C.*

Figure 4.12 shows the complete dynamics of the light I *vs.*V curve under aging conditions (blue light, T=50 ^{o}C). A drastic increase in the series resistance takes place already in the first hours. The FF seems to be affected not only by the increase in series resistance, but also by a developing 'S-shape' which is already present in the fresh condition (See for example in the left graphic of fig. 4.11). This S-shape is related to an internal energy barrier [57]. During the accelerated aging experiment, the dark I *vs.*V curves (not shown) have a strongly reduced forward current compared to the first I *vs.*V curve. After 100 h the exponent (n) from the voltage dependence of the current $I \propto V^n$ tends towards 2 for the forward current, and the voltage range with this exponent increases over time. This is an indication of a space charge built up [268]. This is probably due to low mobility in one or both main materials (ZnPc and C_{60}).

Figures 4.12 and 4.13 show the I *vs.*V dynamics of devices with structure C and D on the same

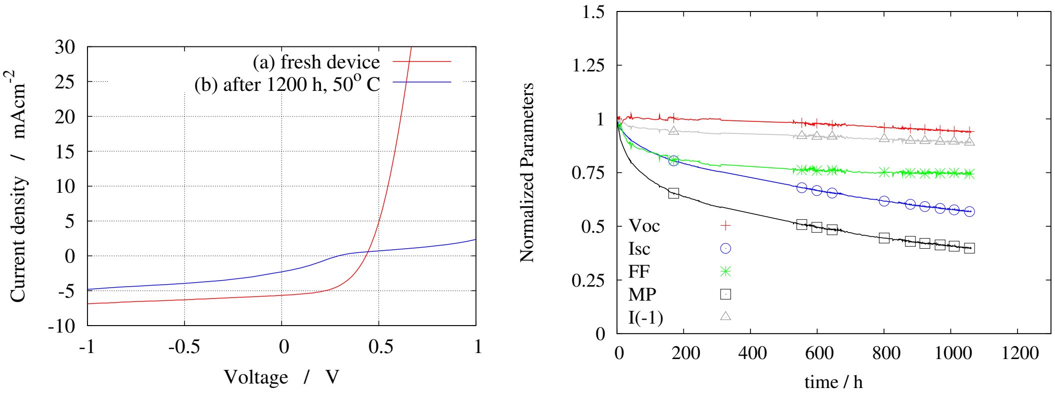

Figure 4.9: Left: Comparison of the I *vs.*V *curves of the devices with structure (B) before and after aging under 50 °C.* I *vs.*V *curves were measured under simulated AM1.5 spectrum with an intensity of 100 mW/cm^2. Right: Normalized values of characteristic parameters of a device with structure (B) aged at illumination of 475 nm and temperature of 50 °C.*

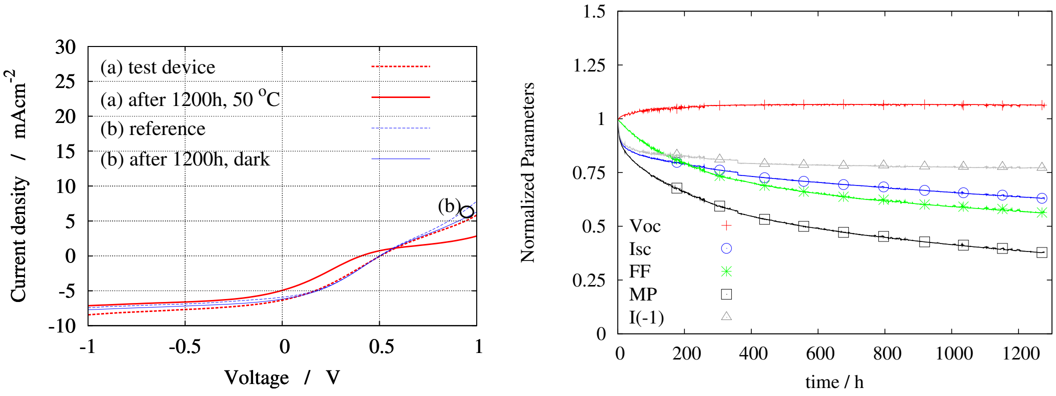

Figure 4.10: Left: Comparison of the I *vs.*V *curves of the devices with structure (C) before and after aging under 50 °C and the corresponding reference, which was stored in dark.* I *vs.*V *curves were measured under simulated AM1.5 spectrum with an intensity of 100 mW/cm^2. Right: Normalized values of characteristic parameters of a device with structure (C) aged at illumination of 475 nm and temperature of 50 °C. The initial values are: open circuit voltage (V_{OC}) = 0.41 V, short circuit current (I_{SC}) = -1.52×10^{-4} A, fill factor (FF) = 0.45, maximum power (MP) = -2.78×10^{-5} W, I(-1 V) = -1.13×10^{-4} A. f(x) is a stretched exponential shown fitted over* $\mathrm{I}(-1\mathrm{V})$. *The fit parameters are $\tau = 4.8 \times 10^6$ h, β = 0.16 resulting in t_H = 485736 h.*

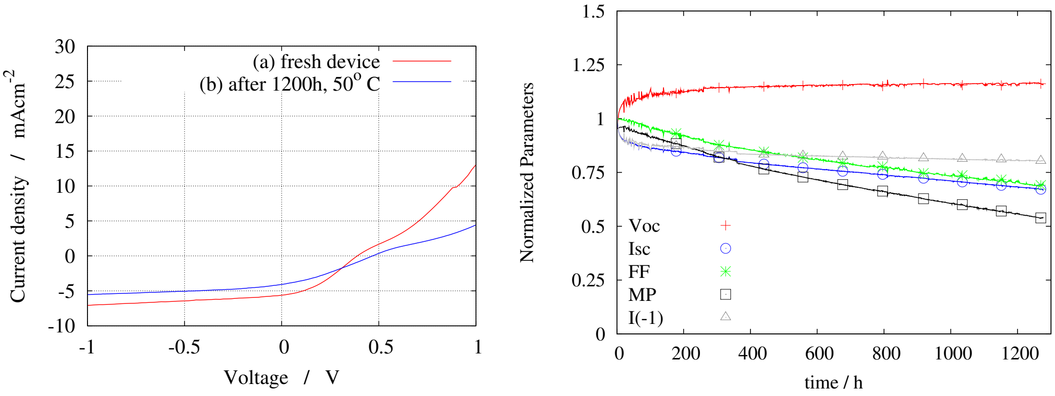

Figure 4.11: Left: Comparison of the I *vs.*V *curves of the devices with structure (D) before and after aging under 50 °C.* I *vs.*V *curves were measured under simulated AM1.5 spectrum with an intensity of 100 mW/cm*^{2}*. Right: Normalized values of characteristic parameters of a device with structure (D) aged at illumination of 475 nm and temperature of 50 °C.*

substrate. The difference on the devices is the Au (1 nm) / NDP2 (1 nm) layer over ITO on device with structure D, this device is slightly more stable with a higher conversion power at the end of the experiment. This kind of graph is not available for structure A and B, due to software development during the measurements.

4.5 Chemical analysis

The laser desorption/ionization time of flight mass spectrometry (LDI-TOF-MS or simply LDI) was used to determine the chemical signature of fragments or reaction products comparing fresh and old samples. Experiments were done by Sebastian Scholz (IAPP). In figures 4.14 and 4.15, one can see the typical mass spectra of C_{60} and ZnPc. The proposed fragmentation spectra for ZnPc is shown in figure 4.5. There were no clear signals of other molecules, indicating that the starting materials and the device fabrication process are quite clean.

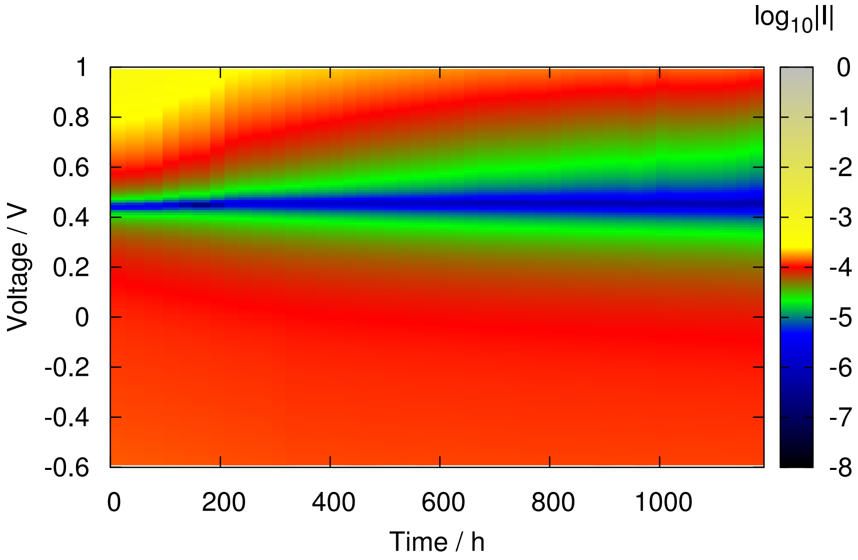

Figure 4.12: Color map of $\log_{10}|I|$ *as function of applied voltage and time for a device with structure C illuminated at 475 nm and held at 50 °C.*

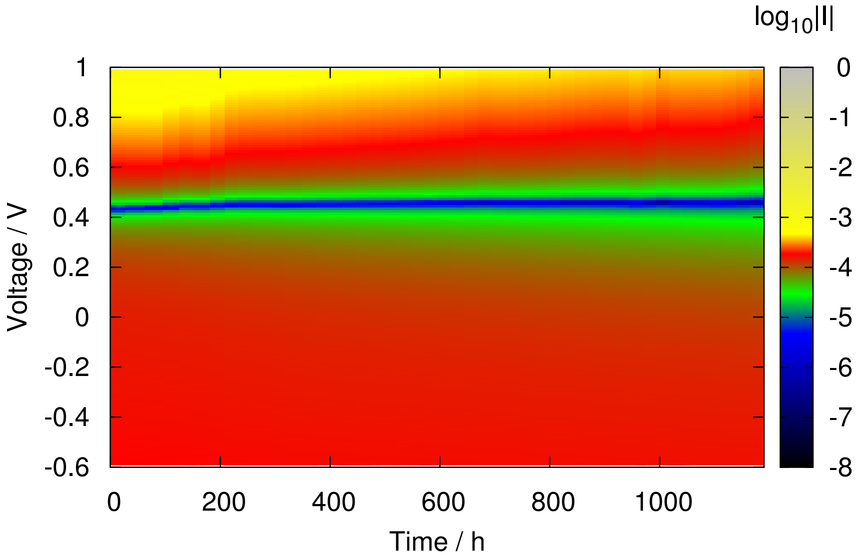

Figure 4.13: Color map of $\log_{10}|I|$ *as function of applied voltage and time for a device with structure D illuminated at 475 nm and held at 50 °C.*

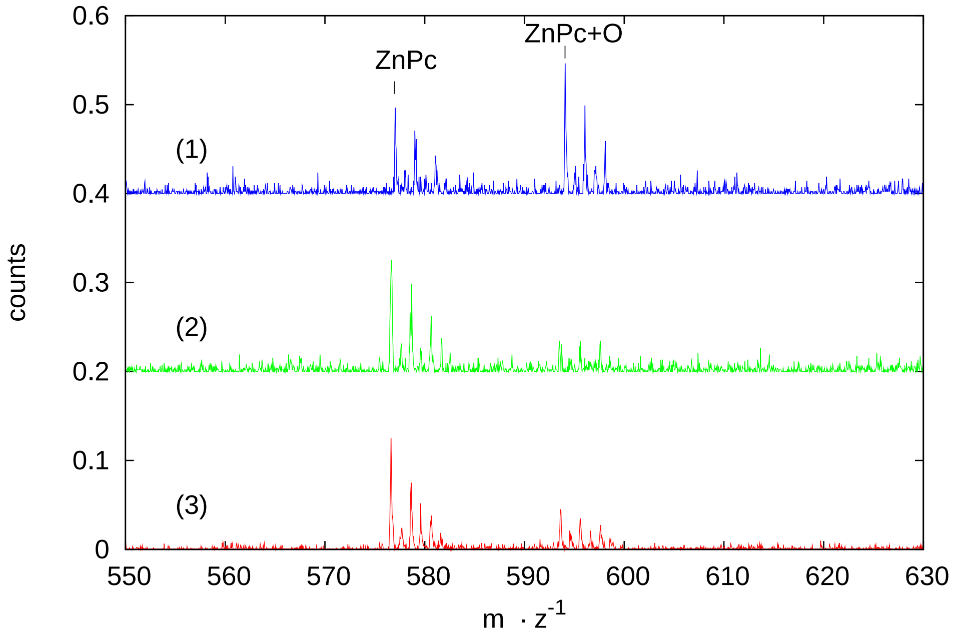

Figure 4.14: Positive mass spectra of samples with structure C showing the typical pattern of ZnPc and an oxidized form of ZnPc. (1) is the reference device, (2) and (3) are the devices aged for 1000 h at 80 ° C and (3) is further aged for 200 h at 115 °C

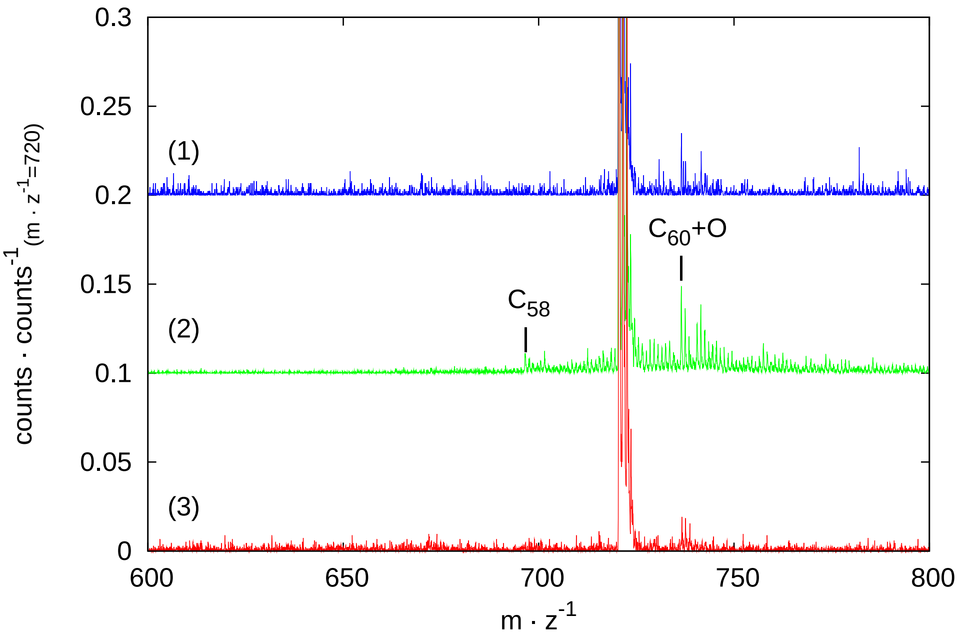

Figure 4.15: Negative mass spectra of samples with structure C, with the peak at 720 normalized to one emphasizing the lateral peaks. (1) is the reference device, (2) and (3) are the devices aged for 1000 h at 80 °C and (3) is further aged for 200 h at 115 °C.

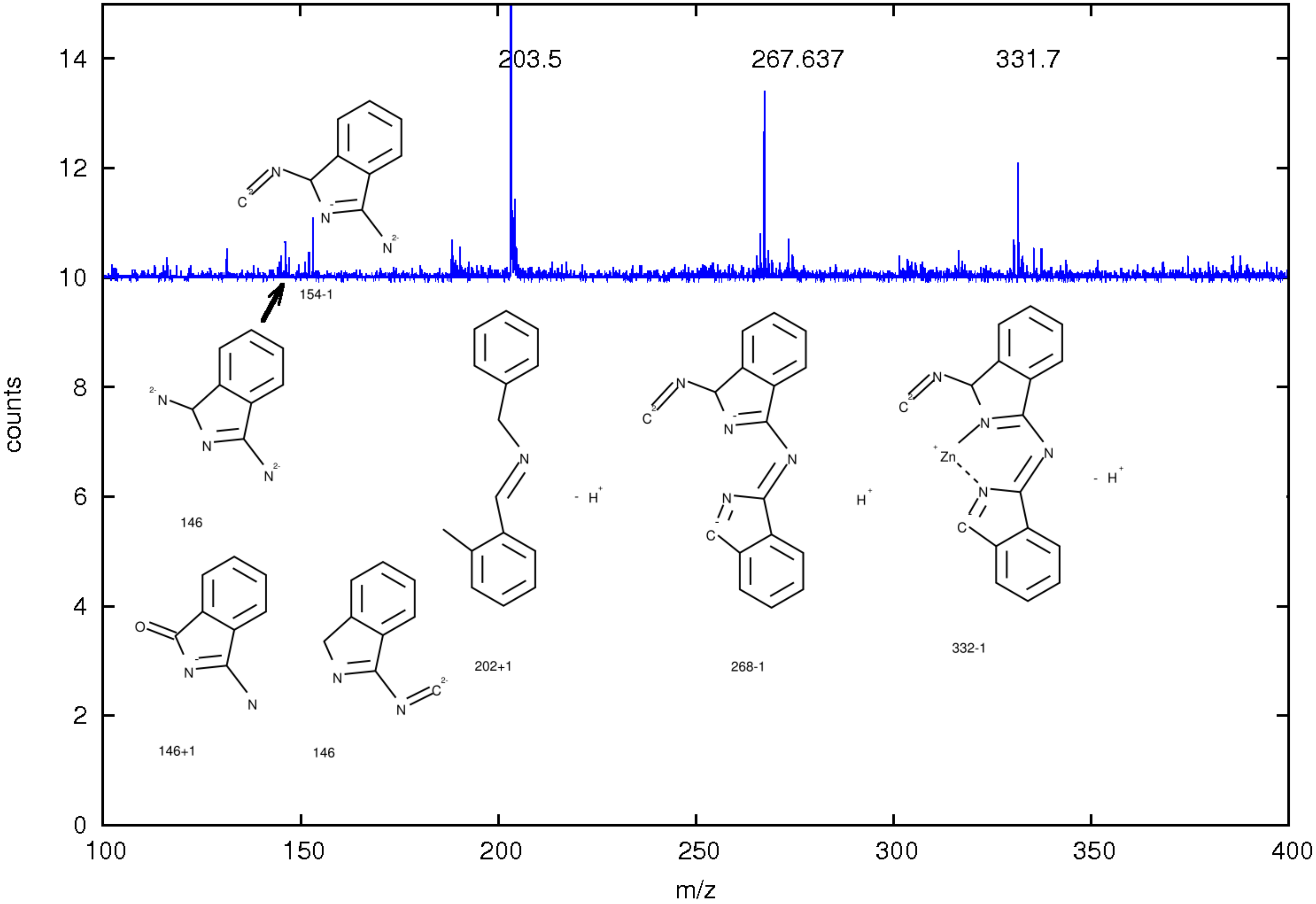

Figure 4.16: Positive mass spectra of sample with structure A. The proposed fragments results from a joint work with Sebastian Scholz.

We analyzed 3 samples with structure A with LDI. One sample is kept in the dark (1). Two samples are aged for 1000 h at 80 °C, one was taken out of the measurement setup and stored in the glove box (2) and one is then further heated at T = 115 °C for 200 h (3) leading to a darkening of the sealant and a complete loss of all photovoltaic characteristics.

ZnPc, ZnPc+O are clearly observed in the spectrum for positive charge (Fig. 4.14). C_{60}, C_{60}+O, and C_{58} are observed in the negative spectrum (Fig. 4.15). C_{56} and C_{54} signals are observed only with stronger laser intensities.

The ratio of intensities from ZnPc+O / ZnPc for the 3 characterized samples is: $(1) > (2) \simeq (3)$. On heating, the ZnPc+O is destroyed, either by losing the oxygen or by fragmentation of the ZnPc part. No strong peaks of fragments from ZnPc were observed. Stronger C_{60}+O and C_{58} signals are detected in the sample B. Since there is oxygen inside the fresh sample, it is expected to react especially with C_{60}. Probably this oxygen in the bulk is already partially reacted in the fresh sample.

The thermal activation energies for the dark reaction described by Wohlers et al [269] can be easily overcome by photoexcitation of C_{60} [207], creating the $C_{60}{>}O$ (the adduct, one oxygen bound to two different adjacent C atoms, breaking a double bond) and the $C_{60}{=}O$ molecule and subsequently breaking the C_{60} cage into smaller molecules. Those are stable only with an even number of C atoms [213]. In the fresh sample there is already molecular oxygen available in the bulk and is partially reacted (1). Over time, atomic oxygen is created and reacts forming C_{60}+O; later it dissociates in C_{58} (2). After further heating (3) the partially oxidized C_{60} or C_{58} further decomposes (CO_2) or polymerizes.

4.6 External quantum efficiency - EQE

There is a direct non-destructive way to test for the degradation of one material in a heterojunction solar cell if the two materials absorb in different parts of the spectrum. This is the case with C_{60} and ZnPc. Despite the changes in the ZnPc contribution to the photocurrent, the main loss in I_{SC} is due to loss of the C_{60} contribution. Dividing the EQE of the aged device by the EQE of the reference device (Fig. 4.17), it can be seen that the main drop of I_{SC} comes from C_{60}. The signal has a similar pattern to the EQE and the C_{60} contribution can be seen inverted, indicating that there is a much stronger degradation of C_{60} than of ZnPc. Nevertheless ZnPc also degrades with a relatively weak signal change between 600 nm and 700 nm.

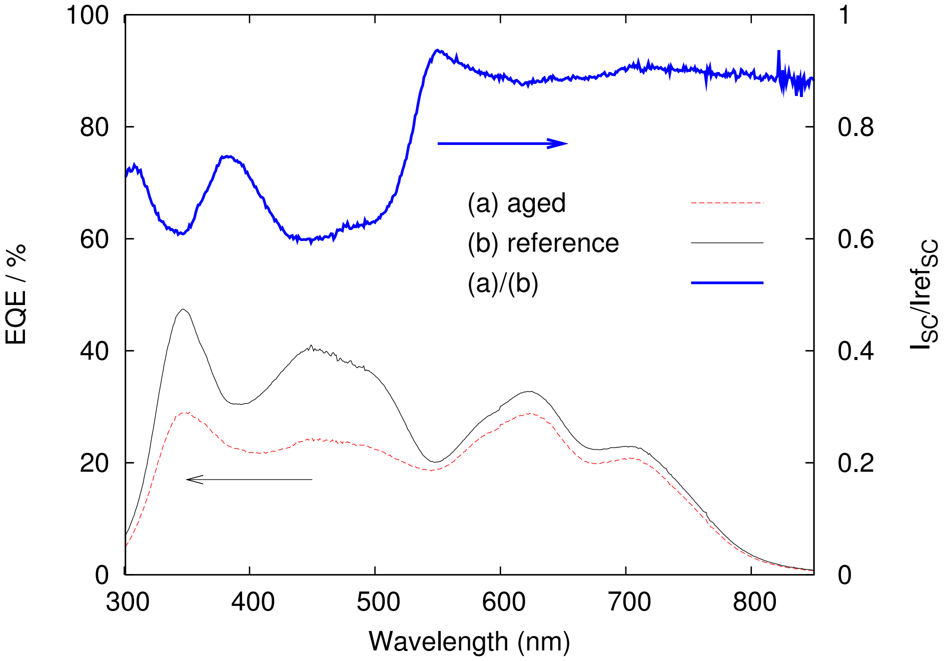

Figure 4.17: EQE of device with structure (C), after aging (a) and reference device (b). The ratio (a)/(b) is shown to emphasize the differences of the aged sample.

4.7 Aging at different operating points

An experiment was conducted with one sample containing 4 devices with structure A [2], where each device was held at a different bias condition (Fig. 4.18). Device 0 was held -0.652 V, device 1 was shorted, device 2 was let open and device 3 was held at a forward voltage of +0.665 V. These voltages were achieved by connecting a small battery (type AAA) in series with Si diodes.

device	Condition	τ	β	$t_{1/2}$ (h)
0	+0.665 V	2887	0.44	1253
1	open	2811	0.54	1417
2	short	3328	0.59	1792
3	-0.652 V	3867	0.49	1817

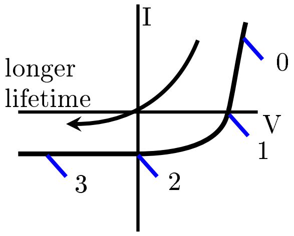

Table 4.3: Summary of the fitting parameters and the time for the I_{SC} *reach half of its initial value, for four devices aged at different voltage conditions. The schematics at the right shows the location of the points in an* I *vs.*V *curve.*

Note that in Fig. 4.18 the data at I_{SC} appears to be aging faster than at -0.652 V. In this case, the graphical representation is not very representative, because the difference in the curves is very small.

---

[2] device with structure A was chosen because a fresh sample was left from this sample batch.

The fitted values are a much better comparison of the aging speed, it shows that both curves have almost the same $t_{1/2}$. In fact, there is a crossing of the two curves at around t=1100 h.

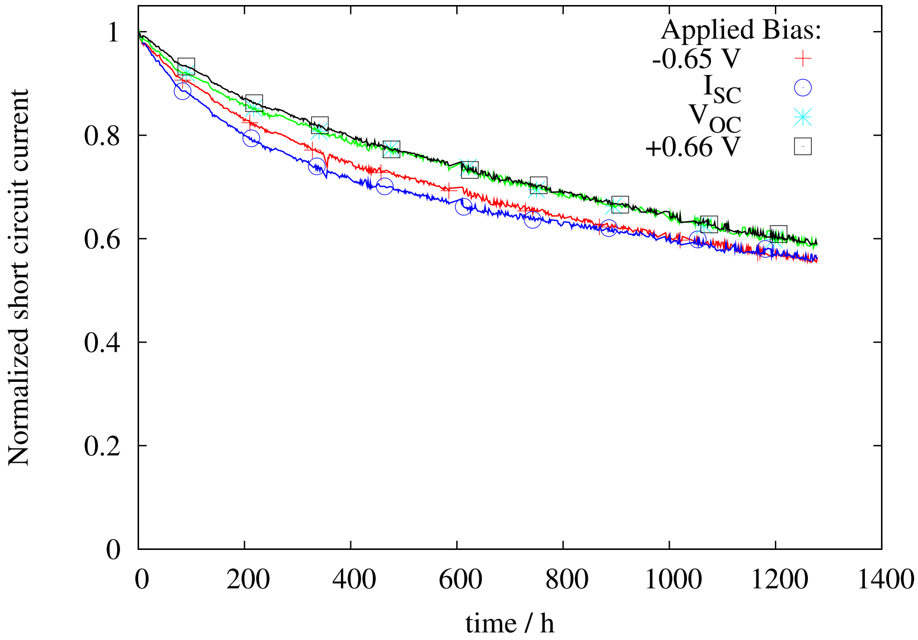

Figure 4.18: Short circuit transients of 4 devices on the same substrate aged at same illumination intensity, same temperature, but different applied bias.

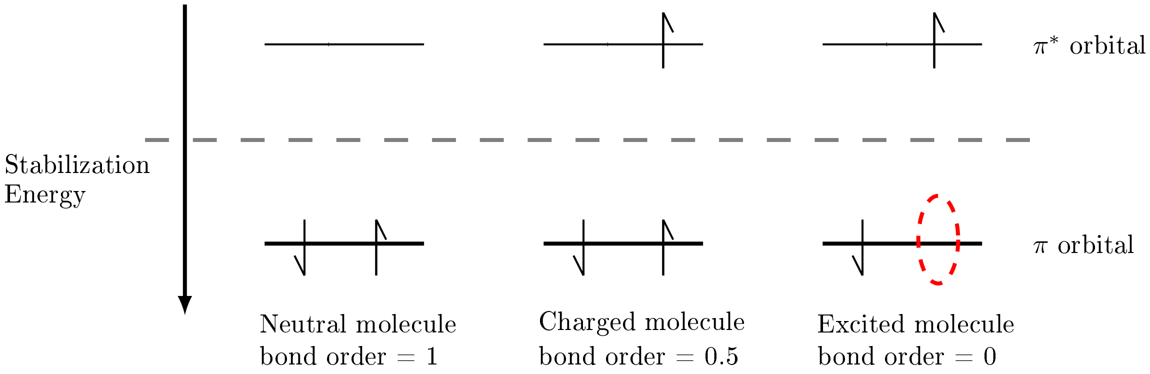

Figure 4.19: Simple representation of the outer energy orbitals of conjugated bonds: neutral molecule, negatively charged molecule, and excited molecule. The respective bond order is given by $1/2\{\mathrm{Nr_{el}}(\pi) - \mathrm{Nr_{el}}(\pi^*)\}$.

Degradation is faster if the device is biased positively, such that the 1/2 lifetime for reverse bias (-0.65 V) is about twice than that with positive bias of +0.67 V. Comparing the 4 devices in table 4.7, we see that $t_{1/2,-0.65V} > t_{1/2,short} > t_{1/2,open} > t_{1/2,+0.67V}$. The fact that $t_{1/2,open}$ is shorter than $t_{1/2,short}$ is not immediately expected, since short circuit is the condition with higher current.

This indicates that the degradation is intensified if the molecules are in the charged or the excited state. The density of charged and excited molecules is higher near the open circuit region than in the region where the device is shorted or reverse polarized. The probable explanation for that is that an excited molecule has one empty binding orbital (π) and one populated anti-binding orbital (π^*), being more unstable, i.e. more susceptible to a bond break or to a chemical reaction than a simple charged molecule with just one filled anti-binding orbital (see Fig. 4.19).

A voltage assisted anodizadion of the Al cathode does not play a role because the dependence of the lifetime with the applied voltage would be opposite. However an assisted reduction of the oxidized Al species and release of oxygen into the organic layers cannot be excluded.

4.7.1 Series and parallel resistance

In large solar cells, a small series resistance(R_S) of several ohms may be responsible for a very low fill factor. An example is given by Prince [233]; a Si solar cell with an area of 6 cm × 1.5 cm has its FF reduced from 77% to 27% when the series resistanceis increased from $\sim 0\ \Omega$ to $5\ \Omega$ ($45\ \Omega cm^2$). For the small areas and small currents used in this work, larger values of series resistance are expected. The R_S dependence on the magnitude of the photocurrent can be calculated using the one diode model (Eq. 2.10). Values of 20 or 30 Ω ($1.86\ \Omega cm^2$) are sufficient for our solar cells to have a well defined I *vs.*V curve with a steep forward current.

The shunt resistance (R_{sh}) of the ZnPc / C_{60} devices is in the range of 10^4 to $10^6\ \Omega$ (620 to 62k Ωcm^2), comparable to the R_{sh} of Si solar cells. For such a high resistance, even relatively large changes of 50% will not affect significantly the shape of the I *vs.*V curve, and the overall performance. The saturation current will not deviate significantly from the photocurrent value.

Fig. 4.20 shows the development of the shunt resistance of a device (with structure B) aged under the same conditions as in section 4.4, the temperature is 74 °C. The R_{sh} is measured by impedance spectroscopy, only a few frequencies are shown. The very weak degradation of R_{sh} is an indication that there is no strong migration of dopants and metals within the device and consequently no effective thickness variation of the intrinsic layers region.

The evolution of series resistance over time, for the same device, is shown in Fig. 4.21. Two different methods for R_S calculation are compared, both are derived from the simple diode model (see sections 2.4.4 and 2.4.3). The method of Kaminski et al [232] gives an increased weight for the points with higher currents. The methods were explained before in sections 2.4.3 and 2.4.4.

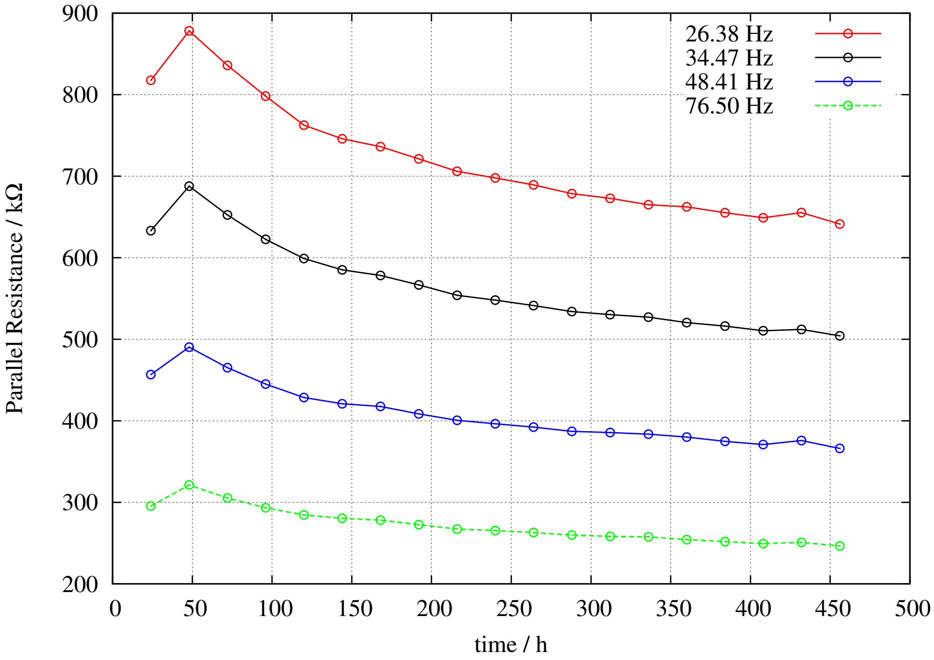

Figure 4.20: Evolution of the parallel resistance of a device ITO / Au (1) / NDP2(1) / ZnPc (20) / C_{60} (40) / ZnPc (3.5) / Al (100), over time. The resistance is calculated from the impedance, for different frequencies.

4.8 Activation energy

An Arrhenius plot to extract the activation energy for I(−1V) is not possible because the t_H values do now show any clear correlation with the temperature. A measurement in the scale of 1000 h may not be sufficient do correctly determine the t_H values of the I(−1V), which are very high ($\sim 10^5$ h). Longer, and even more precisely controlled measurements may be needed. Therefore only the results for I_{SC} are shown here. However, a conclusion can be made with the measured I(−1V) data: if the chemical reactions can be related to decay of the I(−1V) intensity, one can conclude that main chemical reactions are almost completed after the first 200 h of the experiment.

The activation energy is calculated as explained in sec. 2.5, the values based on the I_{SC} data, obtained for structures A, B, C, and D are 0.79 eV, 0.86 eV, 1.20 eV, and 1.44 eV respectively (see Fig. 4.22).

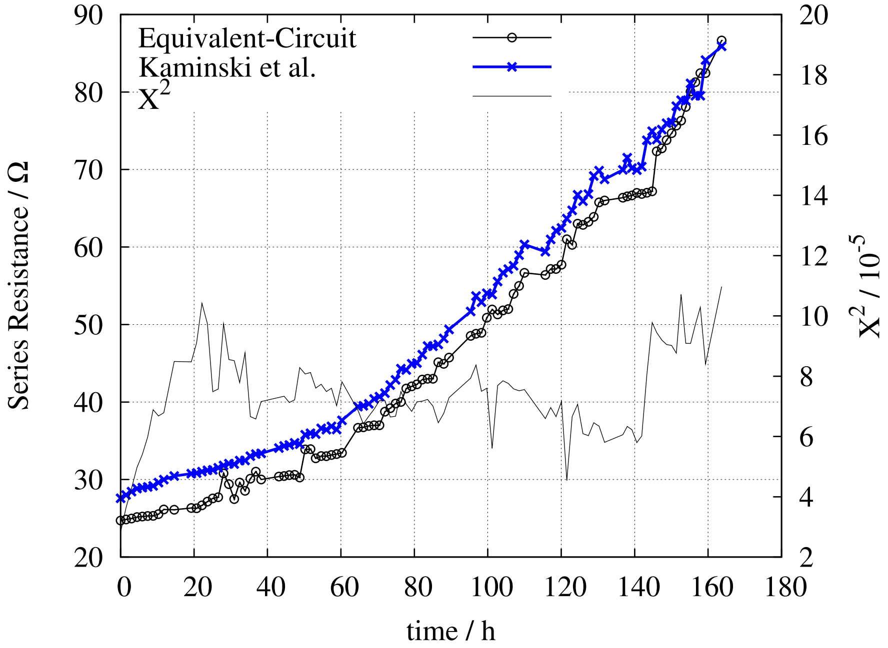

Figure 4.21: Evolution of series resistance of a device ITO / Au (1) / NDP2(1) / ZnPc (20) / C_{60} (40) / ZnPc (3.5) / Al (100), over time. Each data point correspond to a value obtained from a fit to an I *vs.*V *curve. The method of Kaminski et al [232] (* ∗ *) gives an increased weight for the* I *vs.*V *curve region with higher current. The direct fitting* (×) is a fit of the Shockley equation.

4.9 Conclusions

The knowledge of the electronic properties of the interface between the organic semiconductive layers and the electrodes is of high importance for stable solar cells. We have discussed the use of buffer layers on anode and cathode side, organic charge carrier injection layers, n-doping of C_{60}, and ITO surface modification with oxygen plasma. The use of buffer layers on the cathode side is well established in literature and requires a careful thickness optimization. The use of organic dopants as injection layers or in doped semiconductor layers is the simplest way to achieve good and stable ohmic contacts. The plasma treatment of ITO is not a stable solution, it was shown in an accelerated experiment (heating in vacuum) that the improvement of charge carrier injection is strongly reversed.

Precise measurements were shown of encapsulated organic solar cells aged under controlled temperature and illumination for 1000 h. The transients show a fast initial degradation of I_{SC}, FF, I(−1V), and a relatively strong decrease in the exponent dependency of the forward current with applied voltage. V_{OC} is constant or, in some cases, it has a slight increase over the whole measurement period. The saturation current, defined as I(−1V) decays rapidly in the first hours following the decay of I_{SC},

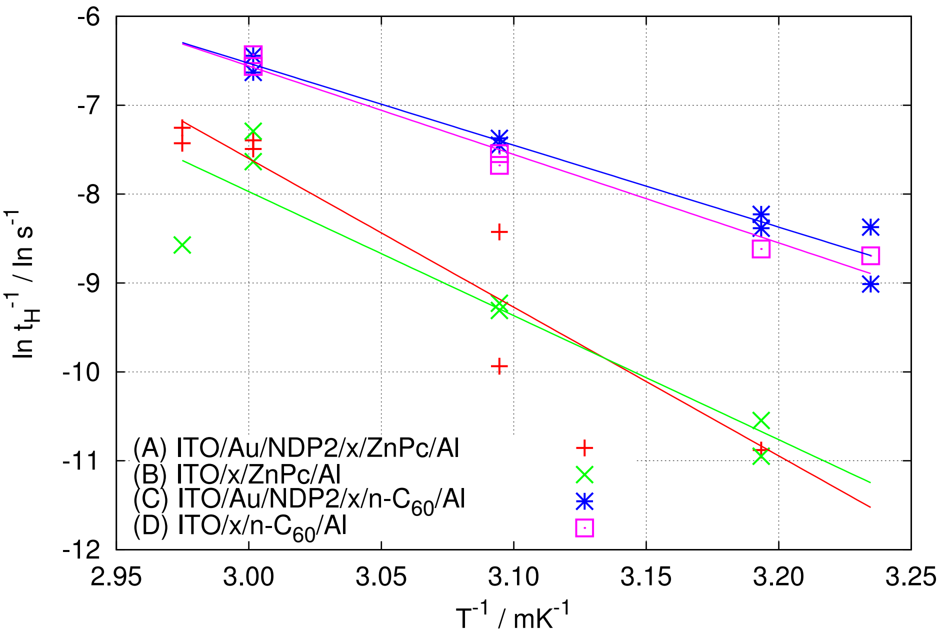

Figure 4.22: Arrhenius plot and linear fits to extract the activation energy of the 4 different device structures, the x *stands for ZnPc (18 nm) / C_{60} (52 nm).*

and then remains constant. The initial decay takes place up to 400 h, whereafter I(−1V) remains almost constant showing that intrinsic material degradation has ceased. We assume that this reduction in I(−1V) is directly related to a strong reduction of the C_{60} contribution to the external quantum efficiency. The photocurrent is more affected by loss of the contribution from C_{60} than from ZnPc, as shown by EQE measurements.

Oxidized C_{60} and sub-products are identified by mass spectrometry. The further degradation of I_{SC} and FF is probably originating from these oxidized species that strongly interfere with the transport.

The activation energy, as calculated from the transients of I_{SC}, varies from 0.79 eV to 1.44 eV, depending on the ITO surface modification and on the buffer layer used. From the very high thermal activation energy, it can be inferred that morphology changes in the photo-active layers play a minor role in degradation.

In summary, the results are very promising: they show that C_{60} and ZnPc, two of the most common materials employed in small molecule organic solar cells, are intrinsically very stable in the device. Some work is still necessary to enable robust, stable ohmic contacts between aluminum and C_{60} and the key stability issue is the oxygen contamination of the organic materials. ZnPc / C_{60} solar cells have the potential to be very stable for a time scale of many years.

Chapter 5

Aging of m-i-p cells

As shown in the last chapter, simple ITO / ZnPc / C_{60} / Al solar cells are not very stable showing a strong initial decrease in I_{SC}, I(-1V) and FF. These devices have a not well defined electronic interface between anode and organic. Degradation of the n-side (C_{60} layer) has also been shown. The solution to this problem may be the use of another kind of electrode. Substituting Al for Ag is not a good solution; Ag tends to diffuse trough the organic layers and create short paths. This is confirmed by the work of Hiramoto's group, they use electron transport layers as thick as 1 μm to avoid short circuits caused by the deposition of the Ag electrode [256]. Another alternative is the Metal-Insulator-p-Semiconductor (m-i-p) device with a donor-acceptor BHJ [21, 270]. As a test structure, devices were made with a layer sequence of ITO / C_{60} / C_{60} : ZnPc / HTL / p:HTL / p:ZnPc / Au.

Both device structures, the Metal-Insulator-p-Semiconductor and the bulk heterojunction, can be compared in the figure 5.1. The m-i-p device can also be considered as an inverted structure, basically the electron extraction is made by the interface between ITO and organic layer. For instance, for polymer solar cells, the inverted structure has several advantages over the non-inverted structure where usually the unstable PEDOT-PSS [271] and the reactive metals Ca, Al or Ba are used as electrodes [272]. In this inverted polymer device structure, the interface for electron extraction can be made directly to ITO and Ag can be used for hole extraction. Silver seems to work in this case because the polymer layers are more than 100 nm thick.

In the m-i-p devices, the thick p-doped HTL ensures a stable contact to the electrode and works as protection layer at the same time. The p-doped layer is, in principle, more stable against the environment than an n-doped layer that uses strong donors, since the strong donors can be easily

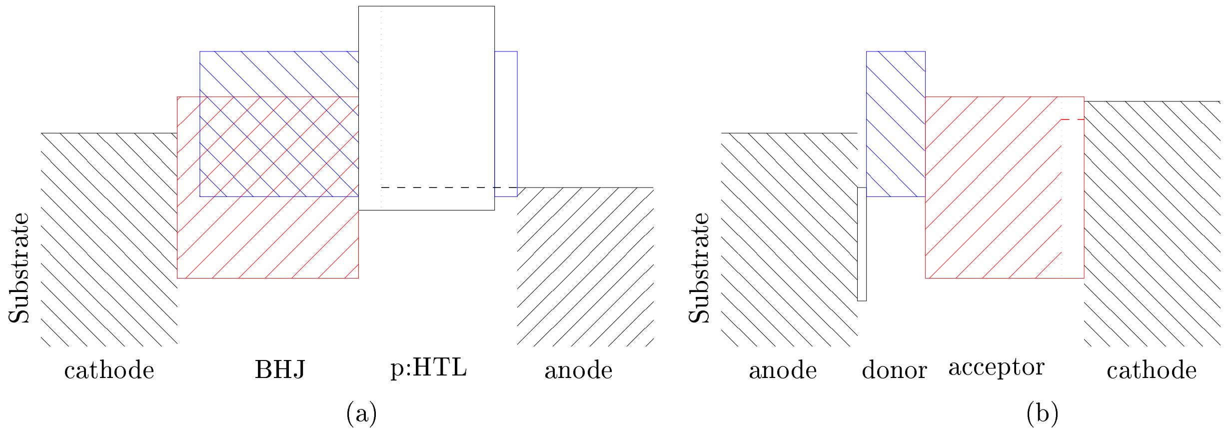

Figure 5.1: Energy diagram comparing the bulk heterojunction Metal-Insulator-p-Semiconductor device (a) and the donor-acceptor flat heterojunction device (b). In both device structures, the bottom electrode is transparent and the top electrode is reflective.

oxidized by atmospheric oxygen. Exceptions can occur when the n-doped layer is stable, even if the separated donor and matrix materials are not (as in AOB:C_{60}, discussed in Sec. 2.1.1). The elimination of the reactive aluminum surface further contributes to the stability of the device.

This chapter addresses the high temperature aging of m-i-p cells, a comparison between different hole transport layers, and the outdoor long time behavior of ITO / C_{60} (5) / C_{60} (20) : ZnPc (10) / DiNPB (5) / p:DiNPB (40) / p:ZnPc (10) / Au (10) / Ag (40) / Au (5) devices.

5.1 High temperature testing

The m-i-p structure is ideal for the testing of HTL, specially for testing the temperature limits of a solar cell. In this device, the active layers are contacted to ITO on one side and to the HTL on the other side. Triphenyl-amine derivatives are known to have a high hole mobility and a wide gap, therefore MeoTPD, MeNPB, and DiNPB were chosen for the experiments. The glass transition temperature (T_g) for DiNPB is 157.8 ºC [229]. Triphenyldiamine (TPD) has a T_g of 60 ºC and we expect that MeoTPD and MeNPB have its T_g slightly above the T_g of TPD (based on the work of Tokito et al [273]).

A blend layer was made with MeoTPD and MeNPB as an attempt to stabilize the HTL at higher temperatures. As one can see on the left side of figure 5.2, the layers are not stable at a temperature of 70 ºC. When using DiNPB as HTL the device is more stable under higher temperatures. The right side of figure 5.2 shows the development of I_{SC} and V_{OC} at 105 ºC of a m-i-p device using DiNPB as HTL.

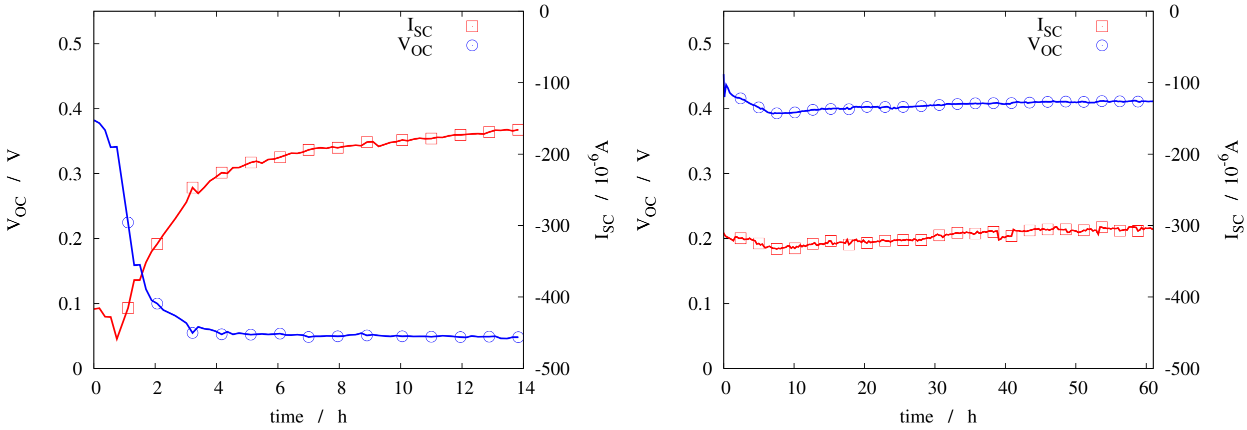

Figure 5.2: Comparison of the aging of two similar devices ITO / C_{60} / C_{60} : ZnPc / HTL / p:HTL / p:ZnPc / Au with two different HTLs. On the left side the hole transport layer is MeoTPD/p:MeNPB:MeoTPD and the sample is kept at 70 °C during measurement, the molecular structure shown is MeNPB. The HTL on the right side it is DiNPB/p:DiNPB and the sample is measured at 105 °C, the molecular structure of DiNPB is shown inside. The illumination is simulated Sun spectra (AM1.5, 127 mW / cm^2).

DiNPB was chosen also for its HOMO position (around 5.4 eV [229]), it still can be doped and it is highly transparent in the visible [1].

From the comparison with different hole transport materials it can be concluded that DiNPB is an adequate material for devices which are submitted to high temperature. A stable structure was chosen for further analysis based on the results of aging of different hole transport materials. The test structure for the following experiments is ITO / C_{60} / C_{60} : ZnPc / HTL / p:HTL / p:ZnPc / Au. All devices were produced on one single wafer. Figure 5.3 shows the distribution of V_{OC}, I_{SC} and FF of all devices of the wafer, measured under simulated AM1.5 (115 mW / cm^2).

5.2 Characteristic aging dynamics

M-i-p devices do not show any deterioration in device performance in the first 200 h of operation. After 200 to 400 h the FF starts to drop drastically. The I_{SC} has typically a smaller drop of a few % after 1000 h, I(−1V) and the V_{OC} remain almost constant.

Figures 5.6 and 5.7 show usual aging profiles of the characteristic parameters of a m-i-p device under constant illumination and under two different temperatures. A possible explanation for the initial

---

[1] The reader is asked to refer to the work of Steffen Pfützner for further information about HTLs in m-i-p diodes [229].

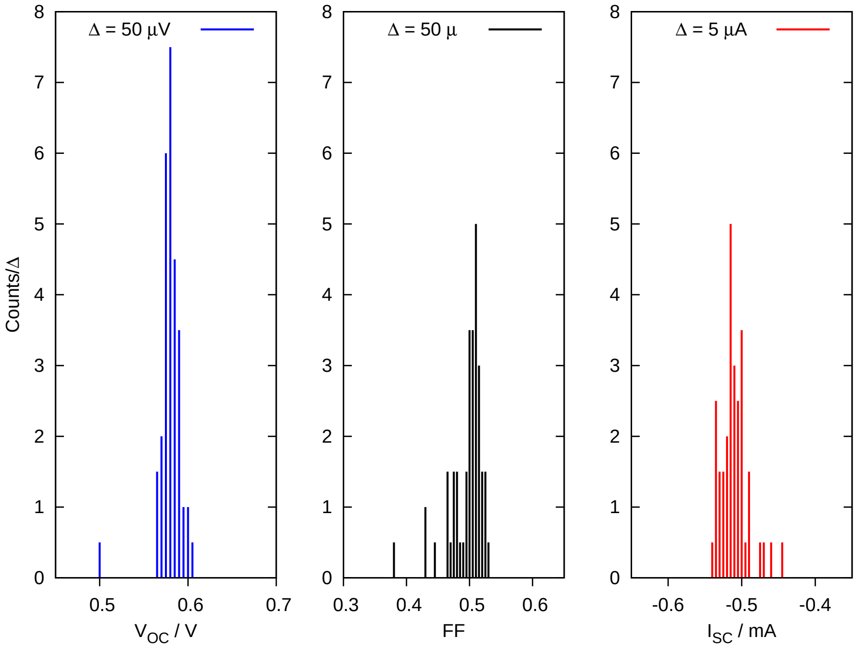

Figure 5.3: Distribution of measured V_{OC}, I_{SC}, *and* FF *from the m-i-p devices on the wafer.*

increase in V_{OC} and FF is an increase in the lowest charge carrier mobility of the intrinsic layer. The FF is limited by the lowest mobility of the bulk heterojunction, in this case it is the hole mobility in ZnPc. Oxygen released from the ITO surface or dopants from the p-doped hole transport layer could diffuse into the intrinsic layer improving the mobility. The initial diffusion in small concentration will not affect the I_{SC} significantly. However, a further increased diffusion is no longer beneficial to the efficiency of the device. In higher concentrations, oxygen in presence of light can undergo chemical reactions with organic materials. Independently of the contamination source, oxygen or p-dopant diffusion, the states created in the active layer can quench excitons, decreasing the FF and the I_{SC}. Figure 5.7 shows this behavior, where initially V_{OC} and FF increase, then the V_{OC} achieves a constant level, and the FF drops again. The decrease of I_{SC} is stronger than the decrease of I(−1V).

This explanation is not complete, because this phenomenon is not observed in all samples in the same manner and besides a slight tendency to occur at higher temperatures, no statistical correlation was yet found. The planar interface between the layers and the bulk interface between donor and acceptor certainly also plays an important role in the aging process. Finally, encapsulation irregularities can not be completely discarded. Small variations in the glue layer thickness between the substrate and the encapsulation cover is an additional variable into the lifetime of the device.

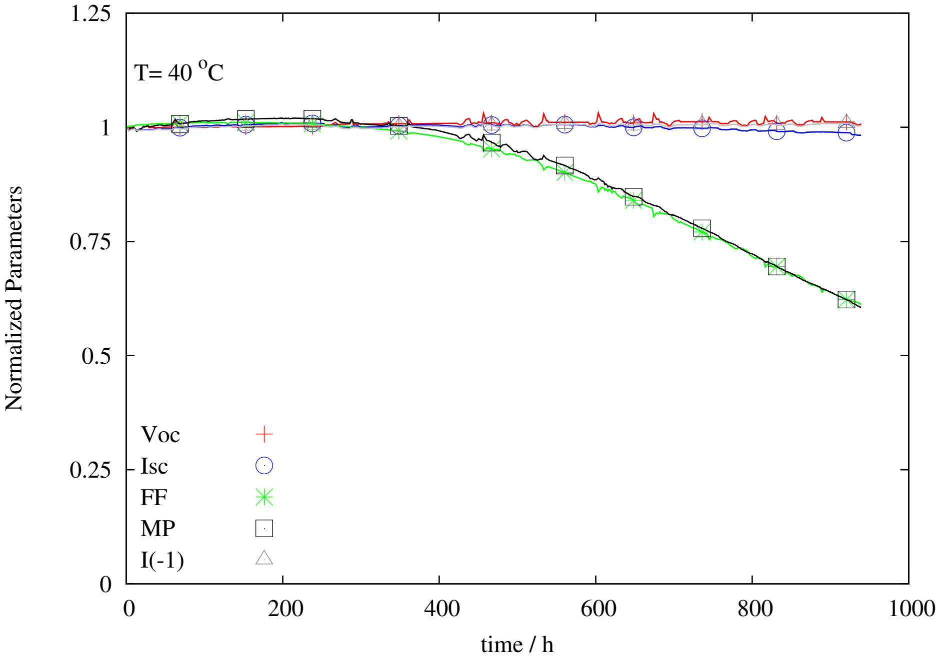

Figure 5.4: Typical aging of a m-i-p cell with structure ITO / C_{60} / C_{60} : ZnPc / HTL / p:HTL / p:ZnPc / Au under 40 °C and illumination of 475 nm at 60 mW / cm^2.

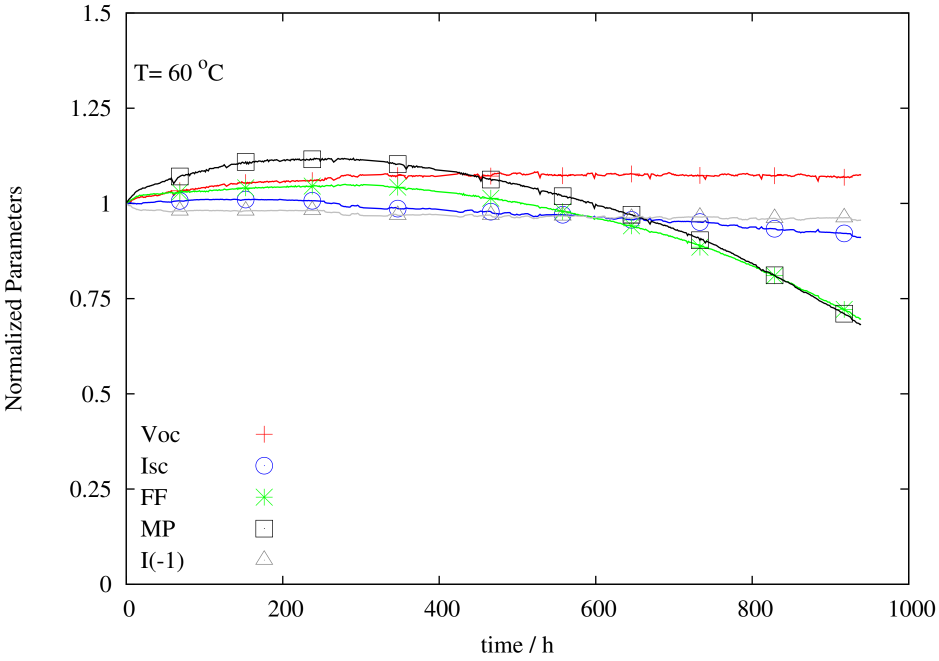

Figure 5.5: Typical aging of a m-i-p cell with structure ITO / C_{60} / C_{60} : ZnPc / HTL / p:HTL / p:ZnPc / Au under 60 °C and illumination centered at 475 nm at 60 mW / cm^2.

5.3 I *vs.*V light and I *vs.*V dark

A dark I *vs.*V curve from a “well behaved” diode, like the fresh m-i-p samples, can be reasonably fitted with the Shockley equation in the range from -1 to +1 V. The approximation $I_{Shockley} = I_{Shockley} + I_{Light}$

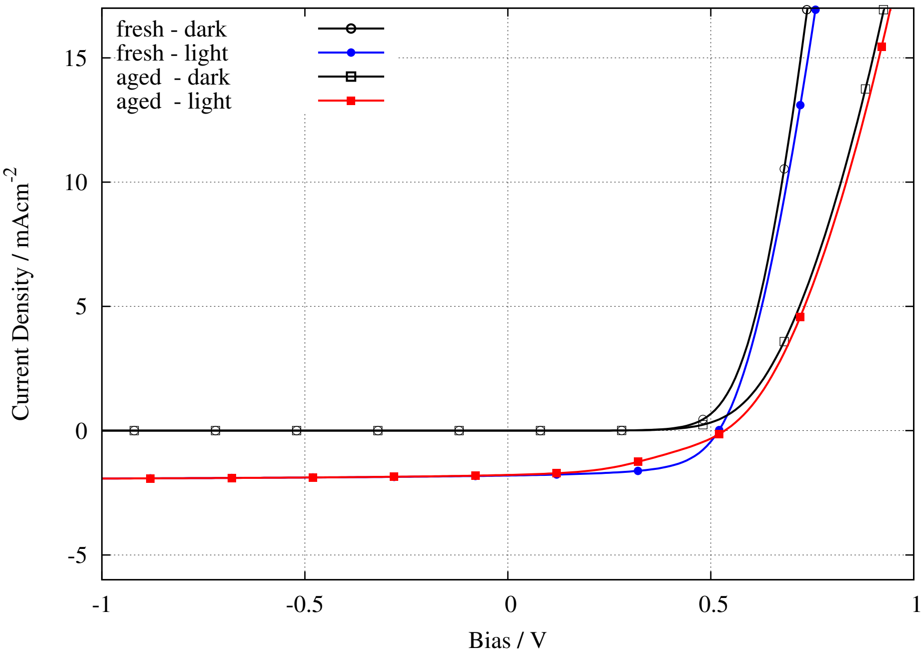

Figure 5.6: I *vs.*V *curve of a m-i-p cell before and after aging for 66 h at a temperature of 40 °C and illumination of 475 nm at 60 mW / cm^2.*

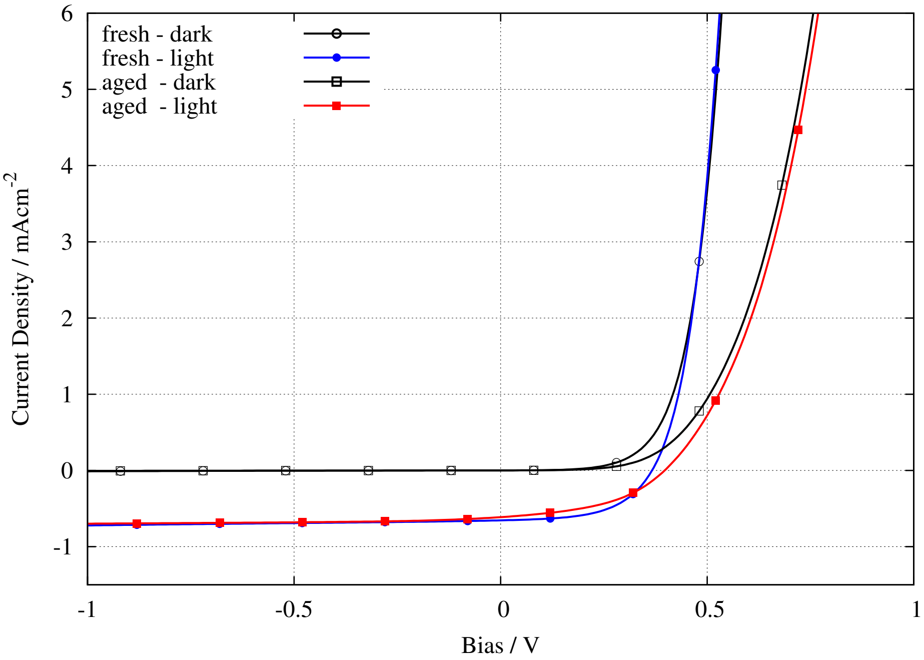

Figure 5.7: I *vs.*V *curve of a m-i-p cell before and after aging for 66 h at a temperature of 60 °C and illumination of 475 nm at 60 mW / cm^2.*

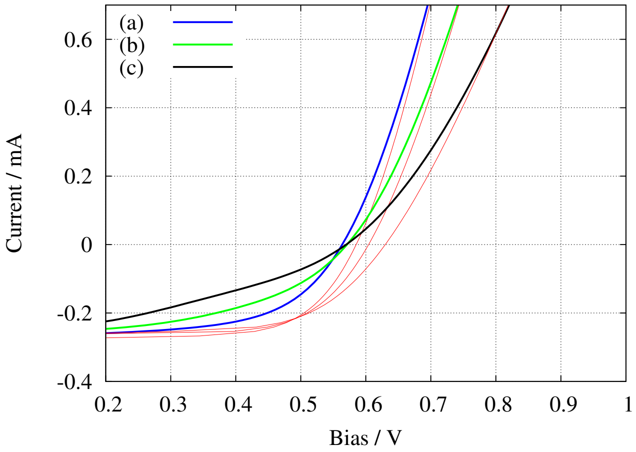

Figure 5.8: Fitting of Shockley equation (in red) on light I *vs.*V *measurements (thicker lines). (a) is at 0 h, (b) at 606 h and (c) at 892 h. The fourth quadrant is emphasized to show the mismatch between the measured data and the fit.*

is very crude as one can see in figures 5.6 - 5.8. The agreement of the fitting is good in the 1st and 3rd quadrants but the dynamics are completely different in the 4th quadrant.

Figure 5.7 shows two pairs of light and dark I *vs.*V curves for new and aged device. In the fresh device, the dark and light currents have the same magnitude at a bias of 0.5 V. The aged device does not show the crossing between the light and the dark I *vs.*V curves. The curves follow in parallel to each other in the aged device. The crossing point, in the fresh device, is an indication for photoconductivity, which facilites charge carrier injection and therefore promote the slightly larger current in the illuminated device. The photoconductivity disappears on the aged device and a series resistancetakes its place.

The aged device also has alterated recombination characteristics, which is reflected by the modified FF. As can be seen in figure 5.8, this difference cannot be explained by the Shockley equation; the corresponding fits added by a constant current does perfectly match the dark I *vs.*V curve (not shown in the picture due to overlap) but only match the light I *vs.*V curve in saturation and in forward current.

5.4 Influence of light intensity and electrical stress

A high measurement rate of up to 11 I *vs.*V curves per hour was used to have the full characterization of the aging of m-i-p diodes. The measurement is from -1.1 V to 1.1 V with 221 points and a delay of 1 s. This relatively slow measurement drives the solar cell on a high current for a time sufficiently long to accelerate the degradation. By comparing figure 5.5 with 5.10, it can be seen that the degradation is current induced. In the former one, there are samples measured at 40 °C and 50 °C with a low rate of

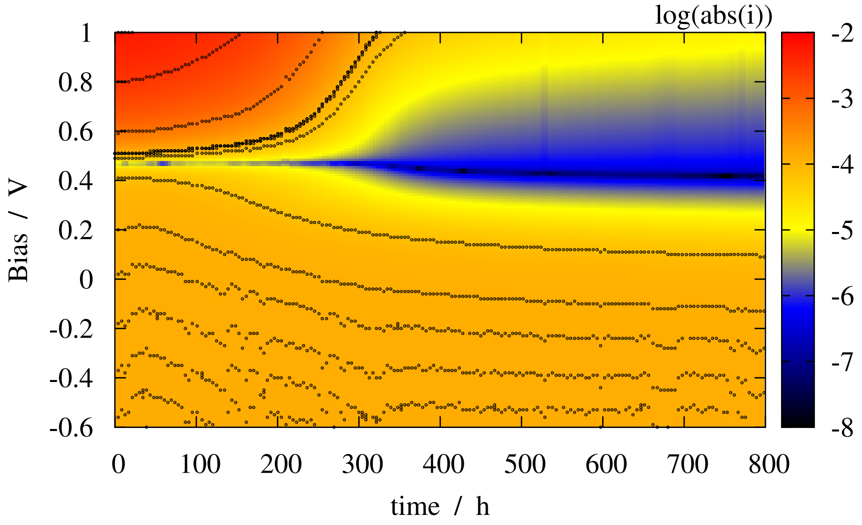

Figure 5.9: Map of I *vs.*V *curves vs. time for a MIP solar cell illuminated with light centered at 475 nm, mW / cm*^{2}*, 50 °C. The black dotted lines are equi-magnitude markers.*

I *vs.*V curves of 1.6 per hour. In the latter one, the device is aged at 50 ℃ with the high measurement rate.

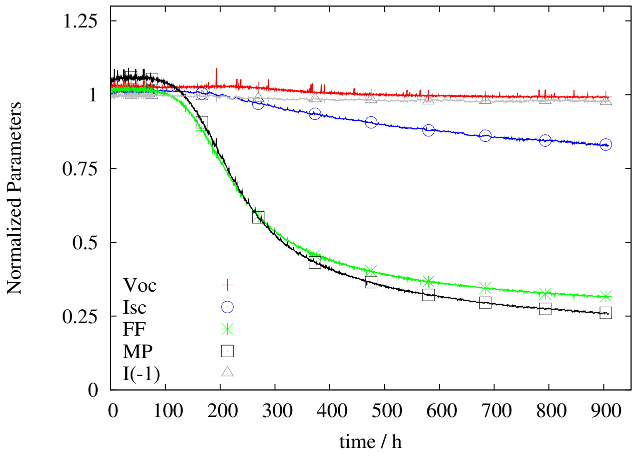

Figure 5.10: Normalized parameters for a ITO / C_{60} */* C_{60} *: ZnPc / HTL / p:HTL / p:ZnPc / Au cell aged under 475 nm light at 2.6 mW / cm*^{2}*. The sample temperature was kept at 50 °C.*

The I *vs.*V curves map of figure 5.9 shows the overall behavior of the aging. Each column is representing one I *vs.*V measurement in the format $\log_{10}(\mathrm{abs}(I))$ *vs.*V; the current value is given by the color coordinate and the time is represented by the abscissa. Its behavior is somehow similar to the ITO / ZnPc / C_{60} / buffer / Al devices: the forward current and the fill factor drop strongly and the curve becomes more flat (absolute current around V_{OC} is lower). The drop in I_{SC} can only be seen in the equi-magnitude lines (dotted lines) plotted on the graph, they also show that the current for more negative bias has lower losses. Figure 5.10 shows the extracted, normalized, parameters for the same measurement, here one can see more clearly that the V_{OC} and the I(−1V) have only very small changes, the I_{SC} drops to $\simeq 80$ % of its initial value, and the FF is the main reason for the strong degradation of the device's converted power, after 200 h.

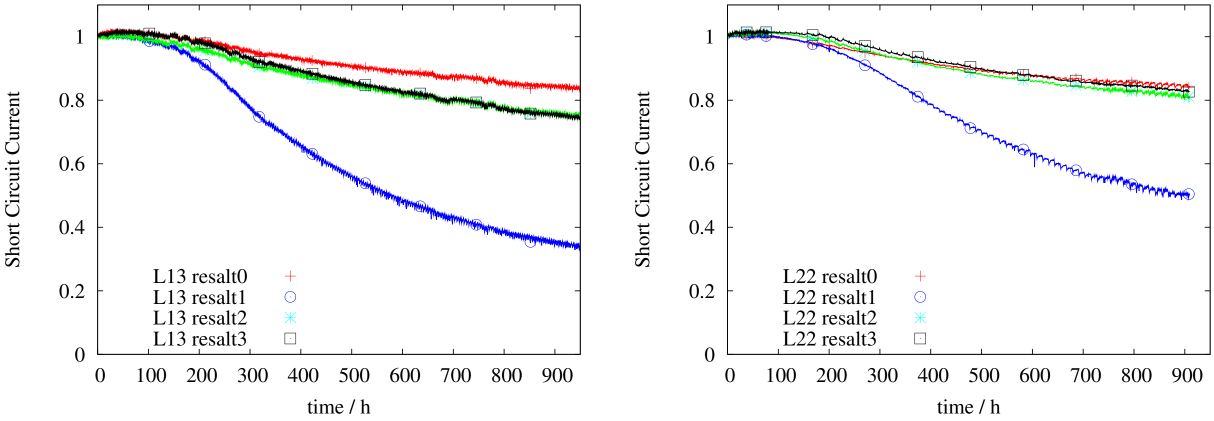

Figure 5.11: Transients of the normalized I_{SC} *of two similar experiments. From each sample, the devices where aged with the light intensities 60, 25.5, 4.8, and 2.6 mW / cm*^{2}*. Device 1 was aged under open circuit condition, devices 0, 1 and 3 were aged under short condition.*

Figure 5.11 shows the transients of the normalized I_{SC} of two similar experiments (left one is same as figs. 5.9 and 5.10) to determine the effect of the light intensity on the degradation of the m-i-p cells. From devices 0 to 3, the devices were illuminated with irradiance of 60, 25.5, 4.8, and 2.6 mW / cm^2 respectively. Device 1 was aged under open circuit condition, devices 0, 2 and 3 were aged under short condition. No dependence on the light intensity can be seen in this graphs, but clearly the device aged under open circuit ages much faster. A small dependence can be seen in the fill factor, and is shown in a semi-logarithmic plot to emphasize it, in figure 5.12.

5.5 Outdoor testing

On site testing of solar cells is the final goal to provide real data for their stability. Ambient conditions are very variable: since light intensity and temperature are not constant, one can not make direct plots from the main parameters, nor from the efficiency vs. time. However, the continuous change in parameters can provide much information for a broad range of values. The connection setup for this experiment is summarized in table 5.1.

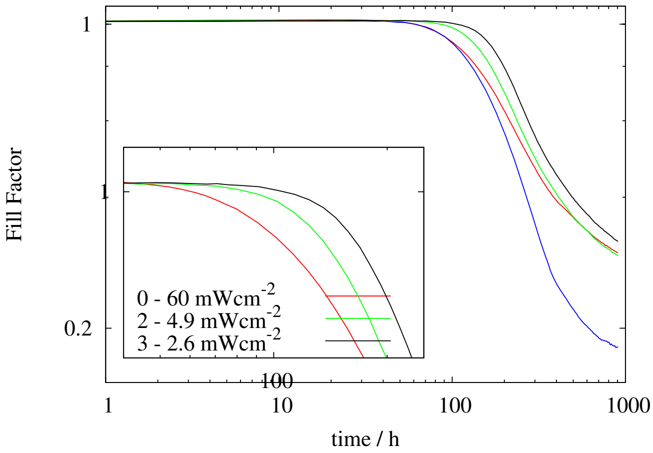

Figure 5.12: Degradation of FF *with time for 3 identical m-i-p devices aged at 50 °C and under different illumination intensities.*

Channel	connection	function
Channel 1	organic solar cell 1	device under test
Channel 2	organic solar cell 2	device under test
Channel 3	organic solar cell 3	device under test
Channel 4	Si solar cell	comparative
Channel 5	Si p-i-n photodiode	reference
Channel 6	Si diode	temperature

Table 5.1: Configuration of the measurement setup for outdoor measurements.

For the outdoor testing a m-i-p sample was fixed to one of the self developed measurement boxes, with three of the four organic solar cells connected to the sample socket. The 4^{th} analog channel was connected to an encapsulated mono-crystalline Si solar cell (encapsulated with the same glass as the organic solar cell, glued with epoxy). A Si p-i-n (BPW42L) photodiode was used to record the light intensity; which photocurrent I_{ref} is linearly proportional to the light intensity. A black encapsulated Si diode (1N4004) was used to record the temperature, measuring the forward voltage drop for a probe current of 1 mA. The sample socket, the sample, and the other sensor components were fixed ouside the window. The rest of the equipment was installed indoors.

Figure 5.13 shows the V_{OC}, the I_{SC}, and the FF over time starting on Monday, 10^{th} of March 14:57:47 2008 (CET) ($51^o1'46.24"N$ $13^o43'42.99"E$ elev. 145 m). The 5^{th} day is a sunny day, the 13^{th} day is cloudy and the others are mixed. The V_{OC} nearly saturates at daylight, depending only little on the light intensity (because the dependence is logarithmic). There is no visible change in V_{OC} and I_{SC} over the whole measurement period of 900 h. Figure 5.14 supports this, showing that the ratio between I_{SC} and I_{ref} does not changes dramatically. The peaks in the ratio are measurements artifacts, caused

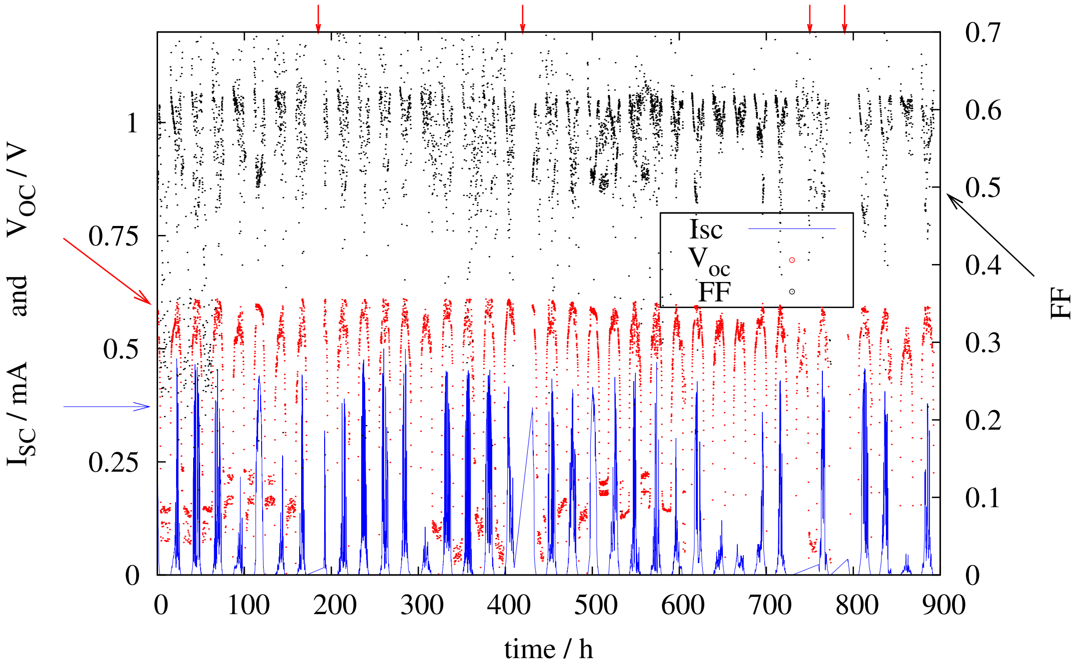

Figure 5.13: Photocurrent, open circuit voltage and FF vs. time for a device ITO / C_{60} / C_{60} : ZnPc / HTL / p:HTL / p:ZnPc / Au fixed on the outside of a lab window at IAPP (51°1′46.24" N 13°43′42.99" E elev. 145 m). The red arrows on the top show the region without data due to system maintenance.

by abrupt change in illumination during the non-simultaneous measurement of the organic solar cell and the Si reference diode[2].

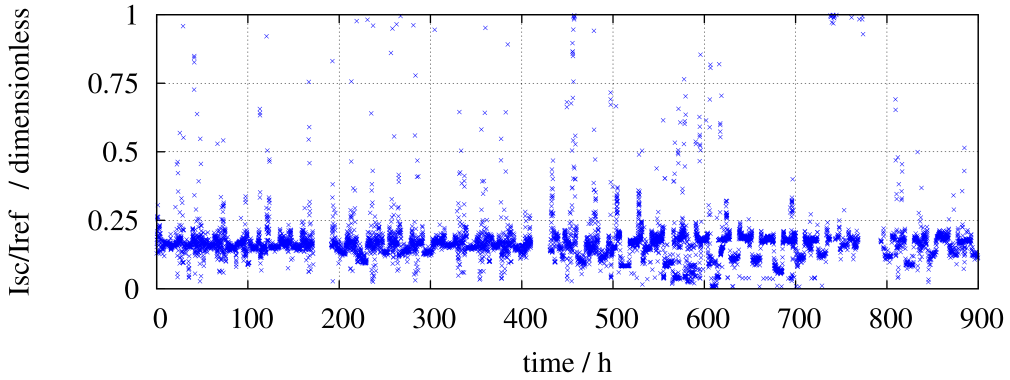

Figure 5.14: Ratio between the short circuit current of the organic solar cell (I_{SC})and the short circuit current of the Si p-i-n reference photodiode (I_{ref}) during the outdoor measurement.

The acquisition speed for the FF determination was increased after 460 h, decreasing considerably the scattering of points. A whole FF measurement takes 3 s. The scattering is created when the irradiance

---

[2] abrupt change in illumination is mainly caused by clouds.

changes during the measurement and a wrong point is measured for the FF, leading e.g. to erroneous values much larger than 0.6.

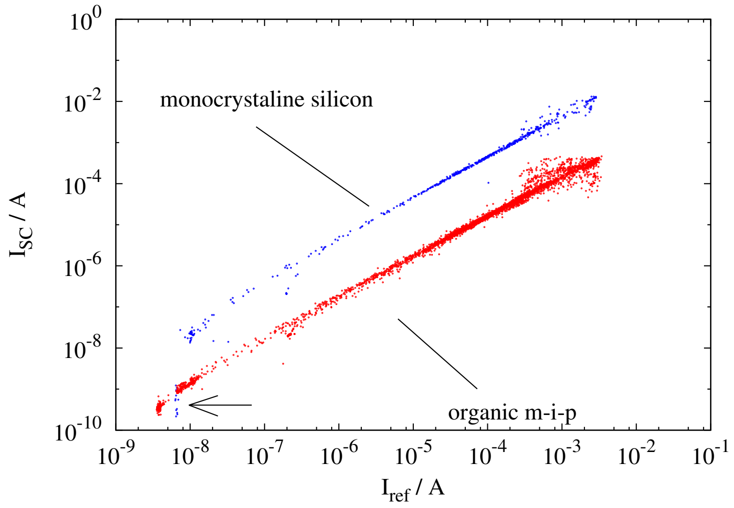

Figure 5.15: Photocurrent and short circuit current of a monocrystaline silicon solar cell vs. the incident light intensity (given by the photocurrent I_{ref}*, of a Si p-i-n photodiode) for a device ITO /* C_{60} */* C_{60} *: ZnPc / HTL / p:HTL / p:ZnPc / Au fixed on the outside a lab window at IAPP. The arrow on the bottom left corner shows the region where the* $\mathrm{I_{SC}}$ *of the silicon solar cell is no longer linearly proportional to the insident light intensity, in contrast to the* $\mathrm{I_{SC}}$ *of the organic solar cell.*

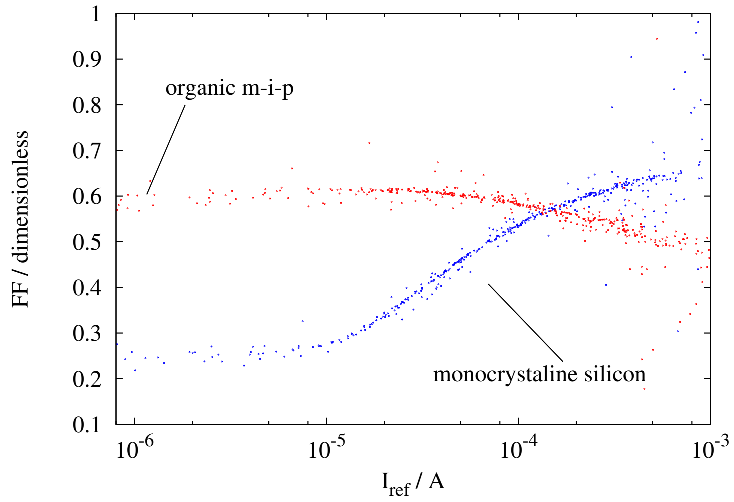

Figure 5.16: Fill factor vs. short circuit current for a device ITO / C_{60} */* C_{60} *: ZnPc / HTL / p:HTL / p:ZnPc / Au fixed on the outside a lab window at IAPP (*$51^o1'46.24"N$ $13^o43'42.99"E$ *elev. 145 m).*

Figure 5.15 shows the linearity of the $\mathrm{I_{SC}}$ of the silicon and the organic solar cell as function of the incident light ($\mathrm{I_{ref}}$, photocurrent of the reference photodiode, BPW42L, with an active area of 7.5 mm^2). Both are linear over more than five orders of magnitude, which is more than sufficient for most applications. However, the fill factor dependence on the light intensity is completely different for both types of solar cells. Figure 5.16 shows this dependence. The organic solar cell shows a saturation of the FF for lower intensities, but a decrease for higher irradiance. The organic solar cell has an advantage over the crystalline Si solar under low-light intensities, where the efficiency of the c-Si solar cell is strongly decreased due to the surface recombination and the effects of deep energy traps.

5.6 Conclusions

Long time operation of ITO / C_{60} / C_{60} : ZnPc / HTL / p:HTL / p:ZnPc / Au devices have shown improved stability in contrast to ITO / ZnPc / C_{60} / Al devices. Both types of devices show almost no deterioration of the saturation current and open circuit voltage. In the m-i-p structure, the aging properties of I_{SC} and FF was further improved. This is attributed to the better protection of the intrinsic layers and stable electrical ohmic contacts. The intrinsic layers are protected by the more stable Au electrode and the thick p-doped transport layers. The FF shows some degradation after several hundred hours, and, together with the forward current it is the most affected characteristic value (provided that the initial FF is large).

Charge carrier transport materials with high glass transition temperature are necessary to ensure thermal stability of the hole transport layers. DiNPB has shown to be far more stable than MeNPB and MeoTPD. The stable operation of a doped organic solar cell at 105 °C was demonstrated.

The outdoor testing of the organic m-i-p solar cell yielded a large amount of information. It was shown that fast measurements cicles are required, specially by searching the maximum power point, because the I *vs.*V curve must not change during the approximation procedure. The encapsulation, and simple mechanical contacts proved to be stable, at least for temperatures between -5 and 25 °C under the Sun (March - April, in Germany). The device itself is also stable, as far as it can be observed over 900 h.

The effects of shunt resistance are much lower in the organic solar cell as compared to solar cell grade silicon, this is naturally given by the lower conductivity of the intrinsic organic materials. Therefore, the organic solar cells are more efficient under lower irradiance, with a similar behavior as the a-Si solar cells.

The measurements demonstrate that the solar cells are stable when exposed to the environment, and that the technical details of the glass encapsulation[3] and electrical connection are not critical and are already solved to a large extent. This indicates an excellent potential for the use of organic solar cells in large scale solar power plants.

---

[3] It is worth to mention that the glass encapsulation may be to expensive or unsuitable for many applications. Further development is necessary to create cheaper and even flexible encapsulations, such as multilayer thin film barriers.

Summary and outlook

This work has addressed the stability of organic solar cells, the analysed devices were donor - acceptor junctions composed of ZnPc and C_{60}. It was shown that the organic molecules are stable on their photoexcitation and charge separation cycles.

A set of equipment for the aging control and measurement was designed and successfully implemented. The construction of this equipment was essential to the experiments, contrary to measurments under an AM1.5 Sun simulator, very useful data could be obtained due to the very stable illumination and sensitive temperature control.

The developed equipment for long time measurements of solar cells provides constant illumination, temperature control, digital communication with computer, and the remote selection of the device to be measured. A software package was also developed to control the aging conditions, the measurements, and to analyze the data. Special parameters were defined for the faster data acquisition needed in outdoor measurements.

Precise measurements of encapsulated ITO / ZnPc / C_{60} / Al solar cells were made. Different interface treatments between electrodes and organic layers show the same overall behavior of the degradation, and different activation energies for the aging of the short circuit current, all on the order of 1 eV. The $I(-1V)$ is almost constant for at least 400 h showing that there is no direct loss of absorbing centers, i.e., no direct degradation of the organic molecules due to photoexcitation.

Wavelength resolved external quantum efficiency measurements and chemical analysis show that ZnPc and C_{60} form reaction products with oxygen and that the photocurrent in aged devices has lost part of its C_{60} contribution. I *vs.*V curves show an increasing serial resistance and decreasing fill factor indicating that the mobility of the organic layers are affected. Furthermore, an increased “S” shape in the 4^{th} quadrant indicates a modification of the energy levels, creating an energy barrier in at least one of the layer interfaces. Given that the stability of the C_{60} / Al interface is a known issue it is supposed that this energy barrier is formed on this interface.

M-i-p organic solar cells were fabricated to overcome the problems of the ITO / ZnPc / C_{60} / Al devices. It is shown that they are more robust against aging and can be stable for a long time even under high temperatures, slightly above 100 ºC. The stable operation of an organic solar cell at 105 ºC was demonstrated. In the m-i-p structure, the aging properties of I_{SC} and FF could be improved in view of the planar junction. The Au electrode added to the thick p-doped hole transport layer is very stable and offers a protection, to the intrinsic organic layers, against gas diffusion. These devices show stable FF and I_{SC} for several hundred hours.

The outdoor testing of the organic m-i-p devices proved that the solar cells, including their electrical contacts and the encapsulation, are chemically and mechanically stabe. No degradation was observed during the 900 h test, at least for temperatures between -5 and 25 ºC under the Sun (March - April, in Germany).

Outlook

Some modifications can be done in the measurement equipment for further improvement. The power source of the LEDs can be redesigned using a MOS-FET linear amplifier commanded by a digital (D-A) interface. The LEDs are developing fast to higher power and higher efficiency levels. New LEDs can be used as light power source, maybe with broader spectrum.

The sample socket can be further modified, to increase the reproducibility (without calibration) between each measurement equipment and to decrease the number of calibrations steps. One new socket that is under test is a copper block, which contains openings for the light and has two integrated high power resistors. This increases the reproducibility of the heating parameters between different sockets (making the calibration easier), since the former design did use glass/ITO where each ITO plate had different resistivity values.

The equipment can be constructed on a rack mount to facilitate integration in larger systems. A microcontroller with larger memory capacity will enable more functions to be integrated in it (for example, self calibration), simplifying the main control software. The software needs a graphical user interface to facilitate the edition of the parameters in the existing database. It was not necessary for the experiments but can be easily written.

The solar cells that use n-side / cathode far from the substrate need to have that interface improved. The interface to aluminum is highly unstable. It is still not clear how to realize that interface, extra protection layers on top of the Al electrode could work. Another improvement would be thick, wide gap electron transport materials that place the photo-active layers far from the cathode and to the outside environment.

The m-i-p structure has shown to be the most promising device structure, and it is the best structure to test new photo-active materials against photooxidation, comparing their $I(-1V)$ against the C_{60} : ZnPc devices. It is also a good test structure to test hole transport layers against their thermal stability.

The m-i-p devices can be further improved by material purification and additional encapsulation measures.

Longer outdoor measurements, at lower latitudes, should be done with highly efficient devices. This measurements should supply realistic lifetime data and also data for comparison with laboratory measurements.

Finally, as a general rule for organic solar cells and also OLEDs, the higher the efficiency, the longer will be the lifetime of the device. High efficiency in solar cells means less heating due to non-radiative recombination. High efficiency also means better and faster transport, shortening the time the molecules stay in their reactive radical state.

Bibliography

[1] L. J. A. Koster, W. J. van Strien, W. J. E. Beek, and P. W. M. Blom. Device operation of conjugated polymer/zinc oxide bulk heterojunction solar cells. *Advanced Functional Materials*, 17(8):1297–1302, 2007.

[2] Fryderyk Kozlowski. *Numerical simulation and optimisation of organic light emitting diodes and photovoltaic cells.* PhD thesis, Technische Universität Dresden, 2005.

[3] S. Saito and A. Oshiyama. Cohesive mechanism and energy-bands of solid C_{60}. *Physical Review Letters*, 66(20):2637–2640, 1991.

[4] see, for example, the articles about offshore windparks. *Financial Times Deutschland*, pages 4–5, 9. September 2008.

[5] *Solar Revolution: The Economic Transformation of the Global Energy Industry.* MIT Press, 2006.

[6] OECD By International Atomic Energy Agency, International Atomic Energy Agency. *Uranium 2007: Resources, Production and Demand.* OECD Publishing, 2008.

[7] Leonard L. Grigsby. *Electric Power Generation, Transmission, and Distribution.* CRC; 2^{nd} edition, 2007.

[8] J. W. Tester, E. M. Drake, M. J. Driscoll, M. W. Golay, and W. A. Peters. *Sustainable Energy: Choosing Among Options.* MIT Press, Cambridge MA, 2005.

[9] H. Shiokawa, M. Yokoyama, and M. Hiramoto. Long-term operation test of organic solid-state solar cells. *Surface Review and Letters*, 14(4):539, 2007.

[10] Karl Leo. Small molecule organic solar cells - status and perspectives. Lectures of the International Symposium "Towards Organic Photovoltaics" in Linz, February 6th - 8th 2008.

[11] R. Franke, B. Maennig, A. Petrich, and M. Pfeiffer. Long-term stability of tandem solar cells containing small organic molecules. *Solar Energy Materials and Solar Cells*, 92(7):732–735, 2008.

[12] M. Hack, V. Adamovich, M. Weaver, and J. Brown. Status of high efficiency and long lifetime phosphorescent oleds. *The 7^{th} International Conference on Electroluminescence of Molecular Materials and Related Phenomena, Dresden*, 2008.

[13] M. Ichida, A. Nakamura, H. Shinohara, and Y. Saitoh. Observation of triplet state of charge-transfer excitons in c60 thin film. *Chemical Physics Letters*, 289(5-6):579 – 585, 1998.

[14] D. Gebeyehu, B. Maennig, J. Drechsel, K. Leo, and M. Pfeiffer. Bulk-heterojunction photovoltaic devices based on donor-acceptor organic small molecule blends. *Solar Energy Materials and Solar Cells*, 79(1):81–92, 2003.

[15] Z. R. Hong, Z. H. Huang, and X. T. Zeng. Utilization of copper phthalocyanine and bathocuproine as an electron transport layer in photovoltaic cells with copper phthalocyanine/buckminsterfullerene heterojunctions: Thickness effects on photovoltaic perfonnances. *Thin Solid Films*, 515(5):3019–3023, 2007.

[16] J. Y. Kim, K. Lee, N. E. Coates, D. Moses, T. Q. Nguyen, M. Dante, and A. J. Heeger. Efficient tandem polymer solar cells fabricated by all-solution processing. *Science*, 317(5835):222–225, 2007.

[17] Q. L. Song, F. Y. Li, H. Yang, H. R. Wu, X. Z. Wang, W. Zhou, J. M. Zhao, X. M. Ding, C. H. Huang, and X. Y. Hou. Small-molecule organic solar cells with improved stability. *Chemical Physics Letters*, 416(1-3):42–46, 2005.

[18] M. Rusu, J. Strotmann, M. Vogel, M. C. Lux-Steiner, and K. Fostiropoulos. Effects of oxygen and illumination on the photovoltaic properties of organic solar cells based on phtalocyanine : fullerene bulk heterojunction. *Applied Physics Letters*, 90(15):153511, 2007.

[19] R. Slota, G. Dyrda, Z. Hnatejko, J. Karolczak, and Z. Stryla. Effect of air-absorbed oxygen and moisture on the chemical stability of photoexcited Mg, Zn, and Eu phthalocyanines in dimethylformamide. *Journal of Porphyrins and Phthalocyanines*, 10(1):43–54, 2006.

[20] C. W. Tang. 2-layer organic photovoltaic cell. *Applied Physics Letters*, 48(2):183–185, 1986.

[21] B. Maennig, J. Drechsel, D. Gebeyehu, P. Simon, F. Kozlowski, A. Werner, F. Li, S. Grundmann, S. Sonntag, M. Koch, K. Leo, M. Pfeiffer, H. Hoppe, D. Meissner, N. S. Sariciftci, I. Riedel, V. Dyakonov, and J. Parisi. Organic p-i-n solar cells: Organic photovoltaics. *Applied Physics A-Materials Science & Processing*, 79(1):1–14, 2004.

[22] http://www.oled-info.com/history, from 05.10.2008.

[23] http://www.g24i.com, from 05.10.2008.

[24] P Prins, F.C. Grozema, J. M. Schins, S Patil, U Scherf, and L. D. A. Siebbeles. High intrachain hole mobility on molecular wires of ladder-type poly(p-phenylenes). *Physical Review Letters*, 96(14):146601, 2006.

[25] P. M. Thomas and A. Weber. High-resolution raman-spectroscopy of gases with laser sources XIII pure rotational spectra of 1,3,5,7-cyclooctatetraene and 1,5-cyclooctadiene. *Journal of Raman Spectroscopy*, 7(6):353–357, 1978.

[26] R. W. I. de Boer, M. E. Gershenson, A. F. Morpurgo, and V. Podzorov. Organic single-crystal field-effect transistors. *Physica Status Solidi a-Applied Research*, 201(6):1302–1331, 2004.

[27] K. Schulze, C. Uhrich, R. Schüppel, K. Leo, M. Pfeiffer, E. Brier, E. Reinold, and P. Bäuerle. Efficient vacuum-deposited organic solar cells based on a new low-bandgap oligothiophene and fullerene C_{60}. *Advanced Materials*, 18(21):2872–2875, 2006.

[28] H. Tanaka, S. Tokito, Y. Taga, and A. Okada. Novel hole-transporting materials based on triphenylamine for organic electroluminescent devices. *Chemical Communications*, 1(18):2175–2176, 1996.

[29] J. E. Fischer and P. A. Heiney. Order and disorder in fullerene and fulleride solids. *Journal of Physics and Chemistry of Solids*, 54(12):1725–1757, 1993.

[30] M. Gouterman. Spectra of porphyrins. *Journal of Molecular Spectroscopy*, 6(1):138–163, 1961.

[31] J. R. Darwent, P. Douglas, A. Harriman, G. Porter, and M. C. Richoux. Metal phthalocyanines and porphyrins as photosensitizers for reduction of water to hydrogen. *Coordination Chemistry Reviews*, 44(1):83–126, 1982.

[32] C. W. Tang and S. A. VanSlyke. Organic electroluminescent diodes. *Applied Physics Letters*, 51(12):913–915, 1987.

[33] M. A. Baldo, D. F. O'Brien, Y. You, A. Shoustikov, S. Sibley, M. E. Thompson, and S. R. Forrest. Highly efficient phosphorescent emission from organic electroluminescent devices. *Nature*, 395(6698):151–154, 1998.

[34] C. Adachi, M. A. Baldo, S. R. Forrest, S. Lamansky, M. E. Thompson, and R. C. Kwong. High-efficiency red electrophosphorescence devices. *Applied Physics Letters*, 78(11):1622–1624, 2001.

[35] W. P. Su, J. R. Schrieffer, and A. J. Heeger. Solitons in polyacetylene. *Physical Review Letters*, 42(25):1698–1701, 1979.

[36] G. Gustafsson, Y. Cao, G. M. Treacy, F. Klavetter, N. Colaneri, and A. J. Heeger. Flexible light-emitting-diodes made from soluble conducting polymers. *Nature*, 357(6378):477–479, 1992.

[37] W. S. Huang, B. D. Humphrey, and A. G. Macdiarmid. Polyaniline, a novel conducting polymer - morphology and chemistry of its oxidation and reduction in aqueous-electrolytes. *Journal of the Chemical Society-Faraday Transactions I*, 82(8):2385–2400, 1986.

[38] M. R. Andersson, M. Berggren, O. Inganäs, G. Gustafsson, J. C. Gustafsson-Carlberg, D. Selse, T. Hjertberg, and O. Wennerstrom. Electroluminescence from substituted poly(thiophenes) - from blue to near-infrared. *Macromolecules*, 28(22):7525–7529, 1995.

[39] T. Miteva, A. Meisel, W. Knoll, H. G. Nothofer, U. Scherf, D. C. Muller, K. Meerholz, A. Yasuda, and D. Neher. Improving the performance of polyfluorene-based organic light-emitting diodes via end-capping. *Advanced Materials*, 13(8):565–570, 2001.

[40] Ingmar Grenthe. *Chemistry, 1996-2000.* Nobel lectures, including presentation speeches and laureates' biographies. World Scientific, River Edge, N.J., 2003.

[41] Michael Hoffmann. *Frenkel and Charge-Transfer Excitons in Quasi-One-Dimensional Molecular Crystals with Strong Intermolecular Orbital Overlap.* PhD thesis, Technische Universität Dresden, 2000.

[42] M. Klessinger and J. Michl. *Excited states and photochemistry of organic molecules.* VCH, New York, 1995.

[43] J. Franck. Elementary processes of photochemical reactions. *Transactions of the Faraday Society*, 21(3):0536–0542, 1926.

[44] E. Condon. A theory of intensity distribution in band systems. *Physical Review*, 28(6):1182–1201, 1926.

[45] D. Beljonne, Z. Shuai, G. Pourtois, and J. L. Brédas. Spin-orbit coupling and intersystem crossing in conjugated polymers: A configuration interaction description. *Journal of Physical Chemistry A*, 105(15):3899–3907, 2001.

[46] M. Klessinger and J. Michl. *Excited states and photochemistry of organic molecules.* VCH, New York, 1995. pp. 255, 266.

[47] K. Horie, U. Ushiki, and F. M. Winnik. *Molecular Photonics.* Wiley-VCH, 2000.

[48] M. Klessinger and J. Michl. *Excited states and photochemistry of organic molecules.* VCH, New York, 1995. pp. 253, 310.

[49] Martin Klessinger and Josef Michl. *Excited states and photochemistry of organic molecules.* VCH, New York, 1995. pp. 266.

[50] V. M. Agranovich and R. M. Hochstrasser. *Spectroscopy and excitation dynamics of condensed molecular systems.* North-Holland; Elsevier Science, 1983.

[51] M. Ichida, A. Nakamura, H. Shinohara, and Y. Saitoh. Observation of triplet state of charge-transfer excitons in C_{60} thin film. *Chemical Physics Letters*, 289(5-6):579–585, 1998.

[52] A. Moliton and J. M. Nunzi. How to model the behaviour of organic photovoltaic cells. *Polymer International*, 55(6):583–600, 2006.

[53] R. C. Powell and Z. G. Soos. Singlet exciton energy-transfer in organic solids. *Journal of Luminescence*, 11(1-2):1–45, 1975.

[54] M. Grover and R. Silbey. Exciton migration in molecular crystals. *Journal of Chemical Physics*, 54(11):4843, 1971.

[55] M. R. Black, C. Chavez, and E. Brosha. Exciton diffusion length of tris (dibenzoylmethane) mono (phenanthroline) europium (III) measured by photocurrent and absorption as a function of wavelength. *Organic Electronics*, 8(5):601–605, 2007.

[56] K. Harada, A. G. Werner, M. Pfeiffer, C. J. Bloom, C. M. Elliott, and K. Leo. Organic homojunction diodes with a high built-in potential: Interpretation of the current-voltage characteristics by a generalized einstein relation. *Physical Review Letters*, 94(3):036601, 2005.

[57] C. Uhrich, R. Schüppel, A. Petrich, M. Pfeiffer, K. Leo, E. Brier, P. Kilickiran, and P. Baeuerle. Organic thin-film photovoltaic cells based on oligothiophenes with reduced bandgap. *Advanced Functional Materials*, 17(15):2991–2999, 2007.

[58] I. I. Fishchuk, A. Kadashchuk, H. Bässler, and S. Něspůrek. Nondispersive polaron transport in disordered organic solids. *Physical Review B*, 67(22), 2003.

[59] I. I. Fishchuk, V. I. Arkhipov, A. Kadashchuk, P. Heremans, and H. Bässler. Analytic model of hopping mobility at large charge carrier concentrations in disordered organic semiconductors: Polarons versus bare charge carriers. *Physical Review B*, 76(4):045210, 2007.

[60] X. Q. Jiang, Y. Harima, L. H. Zhu, Y. Kunugi, K. Yamashita, M. Sakamoto, and M. Sato. Mobilities of charge carriers hopping between π-conjugated polymer chains. *Journal of Materials Chemistry*, 11(12):3043–3048, 2001.

[61] D. S. Liu, L. X. Wang, S. J. Xie, S. H. Han, and L. M. Mei. Electronic confinement in quasi-one-dimensional triblock copolymers. *Chinese Physics*, 12(5):548–552, 2003.

[62] A. Einstein. Über die von der molekularkinetischen theorie der wärme geforderte bewegung von in ruhenden flüssigkeiten suspendierten teilchen. *Ann. Phys.*, 322(8):549–560, 1905.

[63] Y.Q. Peng, J.H. Yang, F.P. Lu, Q.S. Yang, H.W. Xing, X.S. Li, and C.A. Song. Generalization of Einstein relation for doped organic semiconductors. *Applied Physics A: Materials Science & Processing*, 83(2):305–311, 2006.

[64] L. L. Chua, J. Zaumseil, J. F. Chang, E. C. W. Ou, P. K. H. Ho, H. Sirringhaus, and R. H. Friend. General observation of n-type field-effect behaviour in organic semiconductors. *Nature*, 434(7030):194–199, 2005.

[65] J. Simon and J.J. André. *Molecular Semiconductors: photoelectrical properties and solar cells.* Springer-Verlag, 1^{st} edition, 1985.

[66] J. Simon and J.J. André. *Molecular Semiconductors: photoelectrical properties and solar cells.* Springer-Verlag, 1^{st} edition, 1985.

[67] J. Frenkel. On pre-breakdown phenomena in insulators and electronic semi-conductors. *Physical Review*, 54(8):647–648, 1938.

[68] J. G. Simmons. Poole-frenkel effect and Schottky effect in Metal-Insulator-Metal systems. *Physical Review*, 155(3):657–660, 1967.

[69] G. Horowitz. Organic field-effect transistors. *Advanced Materials*, 10(5):365–377, 1998.

[70] G. Pfister. Hopping transport in a molecularly doped organic polymer. *Physical Review B*, 16(8):3676–3687, 1977.

[71] C. Child. Discharge from hot CaO. *Phys. Rev.*, 32(5):492, 1911.

[72] N. Mott and R. Gurney. *Electronic Processes in Ionic Crystals.* Dover, New York, 2 edition, 1940.

[73] M. Koehler and I. Biaggio. Space-charge and trap-filling effects in organic thin film field-effect transistor. *Physical Review B*, 70(045314), 2004.

[74] R. Kepler. Charge carrier production and mobility in anthracene crystals. *Phys. Rev.*, 119(4):1226–1229, 1960.

[75] D. Hertel, H. Bässler, U. Scherf, and H. Hörhold. Charge carrier transport in conjugated polymers. *J. Chem. Phys.*, 110(18):9214, 1999.

[76] A.J. Mozer, N. S. Sariciftci, L. Lutsen, D. Vanderzande, R. Österbacka, M. Westerling, and G. Juška. Charge transport and recombination in bulk heterojunction solar cells studied by the photoinduced charge extraction in linearly increasing voltage technique. *Applied Physics Letters*, 86:112104, 2005.

[77] Y. Harima, T. Eguchi, K. Yamashita, K. Kojima, and M. Shiotani. An in situ ESR study on poly(3-methylthiophene): charge transport due to polarons and bipolarons before the evolution of metallic conduction. *Synthetic Metals*, 105(2):121–128, 1999.

[78] F. Ebisawa, T. Kurobawa, and S. Nara. Electrical properties of polyacetylene-polysiloxane interface. *Journal of Applied Physics*, 54(6):3255–3259, 1983.

[79] A. Tsumura, H. Koezuka, and T. Ando. Macromolecular electronic device- field-effect transistor with a polythiophene thin film. *Applied Physics Letters*, 49(18):1210–1212, 1986.

[80] S. Sze. *Physics of Semiconductor Devices.* John Wiley & Sons, 2^{nd} edition, 1981.

[81] M. Pope and C. Swenberg. *Electronic Processes in Organic Crystals and Polymers.* Oxford Un. Press, New York, 2 edition, 1999.

[82] G. Hadziioannou and P. Hutten, editors. *Semiconducting Polymers: Chemistry, Physics and Engineering.* Wiley-VCH, 2000.

[83] R. Valaski, L. Moreira, L. Micaroni, and I. Hümmelgen. The electronic behavior of poly(3-octylthiophene) electrochemically synthesized onto au substrate. *Brasilian Journal of Physics*, 33(2):392–397, 2003.

[84] G. Heilmeier and S. Harrison. Charge transport in copper phthalocianine single crystals. *Phys. Rev.*, 132(5):2010, 1963.

[85] M. Pfeiffer, A. Beyer, T. Fritz, and K. Leo. Controlled doping of phthalocyanine layers by cosublimation with acceptor molecules: A systematic seebeck and conductivity study. *Applied Physics Letters*, 73(22):3202–3204, 1998.

[86] G. Malliaras, V. Krasnikov, H. Bolink, and G. Hadziioannou. Holographic time-of-flight meassurements of the hole-drift mobility in a photorefractive polymer. *Physical Review B*, 52(10):R14324–R14327, 1995.

[87] F. Martens, H. Brom, and P. Blom. Frequency-dependent electrical response of holes in poly(p-phenylene vinylene). *Physical Review B*, 60(12):R8489–R8492, 1999.

[88] F. Krebs and M. Jørgensen. High carrier mobility in a series of new semiconducting ppv-type polymers. *Macromolecules*, 36(12):4374–4383, 2003.

[89] A. G. Mückl, S. Berleb, W. Brütting, and M. Schwoerer. Transient electroluminescence measurements on organic heterolayer light emitting diodes. *Synthetic Metals*, 111-112(1):91–94, 2000.

[90] M. Redecker and H. Bässler. Optical detection of charge carriers in organic light-emitting diodes. *Applied Physics Letters*, 69(1):70–72, 1996.

[91] K. Book, H. Bässler, A. Elschner, and S. Kirchmeyer. Hole injection form an ITO|PEDT anode into the hole transporting layer of an OLED probed by bias induced absorption. *Org. Elec.*, 4(4):227–232, 2003.

[92] A. Many and G. Rakavy. Theory of transient space-charge-limited currents in solids in the presence of trapping. *Phys. Rev.*, 126(6):1980–1988, 1962.

[93] E. Pinotti, A. Sassella, A. Borghesi, and R. Tubino. Electrical characterization of organic semiconductors by transient current methods. *Synthetic Metals*, 122(1):169–171, 2001.

[94] H. Martens, J. Huiberts, and P. Blom. Simultaneous measurement of electron and hole mobilities in polymer light-emitting diodes. *Applied Physics Letters*, 77(12):1852–1854, 2000.

[95] B. Maennig, M. Pfeiffer, A. Nollau, X. Zhou, K. Leo, and P. Simon. Controlled p-type doping of polycrystalline and amorphous organic layers: Self-consistent description of conductivity and field-effect mobility by a microscopic percolation model. *Physical Review B*, 64(19):195208, 2001.

[96] H. Fritzsche. A general expression for the thermoelectric power. *Solid State Communications*, 9(21):1813–1815, 1971.

[97] A. J. Campbell, D. D. C. Bradley, J. Laubender, and M. Sokolowski. Thermally activated injection limited conduction in single layer n,n'-diphenyl-n,n'-bis(3-methylphenyl)1-1'-biphenyl-4,4'-diamine light emitting diodes. *Journal of Applied Physics*, 86(9):5004–5011, 1999.

[98] Z. Chiguvare, J. Parisi, and V. Dyakonov. Current limiting mechanisms in indium-tin-oxide / poly3-hexylthiophene/aluminium thin film devices. *Journal of Applied Physics*, 94:2440, 2003.

[99] R. Fowler and L. Nordheim. Electron emission in intense electric fields. *Proceedings of the Royal Society of London Series A*, 119(781):173–181, 1928.

[100] M. Koehler, J. R. de Lima, M. G. E. da Luz, and I. A. Hummelgen. Charge injection into thin conjugated polymer films. *Physica Status Solidi A-Applied Research*, 173(1):29–39, 1999.

[101] D. V. Geppert. Space-charge-limited tunnel emission into an insulating film. *Journal of Applied Physics*, 33(10):2993–2995, 1962.

[102] M. Koehler and I. A. Hummelgen. Regional approximation approach to space charge limited tunneling injection in polymeric devices. *Journal of Applied Physics*, 87(6):3074, 2000.

[103] S. Sze. *Physics of Semiconductor Devices.* John Wiley & Sons, 2^{nd} edition, 1981.

[104] D. R. Kearns, G. Tollin, and M. Calvin. Electrical properties of organic solids II effects of added electron acceptor on metal-free phthalocyanine. *Journal of Chemical Physics*, 32(4):1020–1025, 1960.

[105] B. A. Bolto, R. McNeil, and D. E. Wiess. Electronic conduction in polymers. *Australian Journal of Chemistry*, 16(6):1090–1103, 1963.

[106] Y. Yamamoto, K. Yoshino, and Y. Inuishi. Electrical-properties of Phthalocyanine-Halogen complexes. *Journal of the Physical Society of Japan*, 47(6):1887–1891, 1979.

[107] T. J. Marks. Electrically conductive metallomacrocyclic assemblies. *Science*, 227(4689):881–889, 1985.

[108] M. Maitrot, G. Guillaud, and B. Boudjema. Molecular material-based junctions: Formation of a schottky contact with metallophthalocyanine thin films doped by the cosublimation method. *Journal of Applied Physics*, 60(7):2396, 1986.

[109] H. Shirakawa, E.J. Louis, A.G. MacDiarmid, C.K. Chiang, and A.J. Heeger. Synthesis of electrically conducting organic polymers: halogen derivatives of polyacetylene, $(CH)_x$. *J. Chem. Soc.: Chemical Communications*, (16):578–580, 1977.

[110] C.K. Chiang, C.R. Fincher, Y.W. Park Jr, A.J. Heeger, H. Shirakawa, and E.J. Louis. Electrical conductivity in polyacetylene. *Physicl Review Letters*, 39:1098–1101, 1977.

[111] Y. Harima, T. Eguchi, and K. Yamashita. Enhancement of carrier mobilities in poly(3-methylthiophene) by an electrochemical doping. *Synthetic Metals*, 95(1):69–74, 1998.

[112] N. El-khatib, B. Boudjema, G. Guillaud, M. Maitrot, and H. Chermette. Theoretical and experimental doping of molecular materials - p-doping and n-doping of zinc phthalocyanine. *Journal of the Less-Common Metals*, 143(1-2):101–112, 1988.

[113] Wolfgang Brütting. *Physics of Organic Semiconductors.* Wiley-VCH, 2006.

[114] Z. Q. Gao, B. X. Mi, G. Z. Xu, Y. Q. Wan, M. L. Gong, K. W. Cheah, and C. H. Chen. An organic p-type dopant with high thermal stability for an organic semiconductor. *Chemical Communications*, 1(1):117–119, 2008.

[115] K. Walzer, B. Maennig, M. Pfeiffer, and K. Leo. Highly efficient organic devices based on electrically doped transport layers. *Chemical Reviews*, 107(4):1233–1271, 2007.

[116] M. A. Khan, W. Xu, K. U. Haq, Y. Bai, F. Wei, X. Y. Jiang, Z. L. Zhang, and W. Q. Zhu. Highly power efficient organic light-emitting diodes based on p-doped and novel n-doped carrier transport layers. *Journal of Physics D-Applied Physics*, 40(21):6535–6540, 2007.

[117] A. Werner, F. H. Li, K. Harada, M. Pfeiffer, L. Fritz, K. Leo, and S. Machill. n-type doping of organic thin films using cationic dyes. *Advanced Functional Materials*, 14(3):255–260, 2004.

[118] F. H. Li, M. Pfeiffer, A. Werner, K. Harada, K. Leo, N. Hayashi, K. Seki, X. J. Liu, and X. D. Dang. Acridine orange base as a dopant for n doping of C_{60} thin films. *Journal of Applied Physics*, 100(2):023716, 2006.

[119] F. H. Li, A. Werner, M. Pfeiffer, K. Leo, and X. J. Liu. Leuco crystal violet as a dopant for n-doping of organic thin films of fullerene C_{60}. *Journal of Physical Chemistry B*, 108(44):17076–17082, 2004.

[120] M. Y. Chan, S. L. Lai, M. K. Fung, C. S. Lee, and S. T. Lee. Doping-induced efficiency enhancement in organic photovoltaic devices. *Applied Physics Letters*, 90(2):094506, 2007.

[121] M. Hiramoto. Design of nanostructure for photoelectric conversion by vertical organic superlattice. *Electronics and Communications in Japan (Part II Electronics)*, 89(11):13–18, 2006.

[122] S. H. Park, A. Roy, S. Beaupré, S. Cho, N. Coates, J. S. Mon, D. Moses, M. Leclerc, K. Lee, and A. J. Heeger. Bulk heterojunction solar cells with internal quantum efficiency approaching 100 %. *Nature Photonics*, 3(5):297–303, 2009.

[123] M Reyes-Reyes, K Kim, and D. L. Carroll. High-efficiency photovoltaic devices based on annealed poly(3-hexylthiophene) and 1-(3-methoxycarbonyl)-propyl-1-phenyl-(6,6)C_{61} blends. *Applied Physics Letters*, 87(8), 2005.

[124] U. Bach, D. Lupo, P. Comte, J.E. Moser, F. Weissörtel, J. Salbeck, H. Spreitzer, and M. Grätzel. Solid-state dye-sensitized mesoporous TiO_2 solar cells with high photon-to-electron conversion efficiencies. *Nature*, 395(6702):583–585, 1998.

[125] Fryderyk Kozlowski. *Numerical simulation and optimisation of organic light emitting diodes and photovoltaic cells.* PhD thesis, Technische Universität Dresden, 2005.

[126] L. J. A. Koster, E. C. P. Smits, V. D. Mihailetchi, and P. W. M. Blom. Device model for the operation of polymer/fullerene bulk heterojunction solar cells. *Physical Review B*, 72(8):085205, 2005.

[127] S. Sze. *Physics of Semiconductor Devices.* John Wiley & Sons, 2^{nd} edition, 1981.

[128] K. Müllen and U. Scherf. *Organic Light Emitting Devices: Synthesis, Properties and Applications.* Wiley-VCH, 2006. see chapter 2.

[129] L. Onsager. Initial recombination of ions. *Physical Review*, 54(8):554–557, 1938.

[130] L. J. A. Koster, V. D. Mihailetchi, and P. W. M. Blom. Bimolecular recombination in polymer/fullerene bulk heterojunction solar cells. *Applied Physics Letters*, 88(5):052104, 2006.

[131] Peter Würfel. *Physik der Solarzellen.* Spektrum Akademischer Verlag, Heidelberg-Berlin, 2000.

[132] S. Gunes, H. Neugebauer, and N. S. Sariciftci. Conjugated polymer-based organic solar cells. *Chemical Reviews*, 107(4):1324–1338, 2007.

[133] Fryderyk Kozlowski. *Numerical simulation and optimisation of organic light emitting diodes and photovoltaic cells.* PhD thesis, Technische Universität Dresden, 2005.

[134] B. Mazhari. An improved solar cell circuit model for organic solar cells. *Solar Energy Materials and Solar Cells*, 90(7-8):1021–1033, 2006.

[135] B. P. Rand, D. P. Burk, and S. R. Forrest. Offset energies at organic semiconductor heterojunctions and their influence on the open-circuit voltage of thin-film solar cells. *Physical Review B*, 75(11):115327, 2007.

[136] E. Hecht. *Optics.* Addison Wesley, 1998.

[137] Fryderyk Kozlowski. *Numerical simulation and optimisation of organic light emitting diodes and photovoltaic cells.* PhD thesis, Technische Universität Dresden, 2005.

[138] N.-K. Persson, M. Schubert, and O. Inganas. Optical modelling of a layered photovoltaic device with a polyfluorene derivative/fullerene as the active layer. *Solar Energy Materials and Solar Cells*, 83(2-3):169–186, 2004.

[139] J. Drechsel, B. Männig, F. Kozlowski, M. Pfeiffer, K. Leo, and H. Hoppe. Efficient organic solar cells based on a double *p-i-n* architecture using doped wide-gap transport layers. *Applied Physics Letters*, 86(24):244102, 2005.

[140] O. Kohle. The photovoltaic stability of bis(isothiocyanato)ruthenium(II)-bis-2,2'-bipyridine-4,4'-dicarboxylic acid and related sensitizers. *Advanced Materials*, 9(11):904–906, 1997.

[141] M.K.I. Senevirathnaa, P.K.D.D.P. Pitigalaa, E.V.A. Premalala, K. Tennakonea, G.R.A. Kumarab, and A. Konno. Stability of the SnO_2/MgO dye-sensitized photo electrochemical solar cell. *Solar Energy Materials and Solar Cells*, 91(6):544–547, 2007.

[142] S. Schuller, P. Schilinsky, J. Hauch, and C. J. Brabec. Determination of the degradation constant of bulk heterojunction solar cells by accelerated lifetime measurements. *Applied Physics A-Materials Science & Processing*, 79(1):37–40, 2004.

[143] R. De Bettignies, J. Leroy, M. Firon, and C. Sentein. Accelerated lifetime measurements of P3HT : PCBM solar cells. *Synthetic Metals*, 156(7-8):510–513, 2006.

[144] K. Manabe, S. Kusabayashi, and M. Yokoyama. Long-life organic solar-cell fabrication using quinacridone pigment. *Chemistry Letters*, 16(4):609–612, 1987.

[145] M. L. Wang, Q. L. Song, H. R. Wu, B. F. Ding, X. D. Gao, X. Y. Sun, X. M. Ding, and X. Y. Hou. Small-molecular organic solar cells with C_{60}/Al composite anode. *Organic Electronics*, 8(4):445–449, 2007.

[146] V. Nadenau, U. Rau, A. Jasenek, and H. W. Schock. Electronic properties of $CuGaSe_2$-based heterojunction solar cells. part I. transport analysis. *Journal of Applied Physics*, 87(1):584–593, 2000.

[147] J. W. Arbogast, A. P. Darmanyan, C. S. Foote, Y. Rubin, F. N. Diederich, M. M. Alvarez, S. J. Anz, R. L. Whetten, and Er. Photophysical properties of C_{60}. *Journal of Physical Chemistry*, 95(1):11–12, 1991.

[148] F. C. Krebs and K. Norrman. Analysis of the failure mechanism for a stable organic photovoltaic during 10 000 h of testing. *Progress in Photovoltaics: Research and Applications*, 15(8):697–712, 2007.

[149] K. Norrman, N. B. Larsen, and F. C. Krebs. Lifetimes of organic photovoltaics: Combining chemical and physical characterisation techniques to study degradation mechanisms. *Solar Energy Materials and Solar Cells*, 90(17):2793–2814, 2006.

[150] M. Lira-Cantu, K. Norrman, J. W. Andreasen, and F. C. Krebs. Oxygen release and exchange in niobium oxide MEHPPV hybrid solar cells. *Chemistry of Materials*, 18(24):5684–5690, 2006.

[151] R. Könenkamp, G. Priebe, and B. Pietzak. Carrier mobilities and influence of oxygen in C_{60} films. *Physical Review B*, 60(16):11804–11808, 1999.

[152] Z. Li and H. Meng. *Organic Light-Emitting Materials and Devices.* CRC Press, 2007.

[153] D. J. Milliron, I. G. Hill, C. Schen, A. Kahn, and J. Schwartz. Surface oxidation activates indium tin oxide for hole injection. *Journal of Applied Physics*, 87(1):572–576, 2000.

[154] I. G. Hill, D. Milliron, J. Schwartz, and A. Kahn. Organic semiconductor interfaces: electronic structure and transport properties. *Applied Surface Science*, 166(1-4):354–362, 2000.

[155] K. Sugiyama, H. Ishii, Y. Ouchi, and K. Seki. Dependence of indium-tin-oxide work function on surface cleaning method as studied by ultraviolet and x-ray photoemission spectroscopies. *Journal of Applied Physics*, 87(1):205–298, 2000.

[156] C. Qiu, Z. Xie, H. Chen, M. Wong, and H. S. Kwok. Comparative study of metal or oxide capped indium-tin oxide anodes for organic light-emitting diodes. *Journal of Applied Physics*, 93(6):3253–3258, 2003.

[157] C. C. Wu, C. I. Wu, J. C. Sturm, and A. Kahn. Surface modification of indium tin oxide by plasma treatment: An effective method to improve the efficiency, brightness, and reliability of organic light emitting devices. *Applied Physics Letters*, 70(11):1348–1350, 1997.

[158] A. Wan, J. Hwang, F. Amy, and A. Kahn. Impact of electrode contamination of the α-npd/au hole injection barrier. *Organic Electronics*, 6(1):47–54, 2005.

[159] I. G. Hill, A. Rajagopal, A. Kahn, and Y. Hu. Molecular level alignment at organic semiconductor-metal interfaces. *Applied Physics Letters*, 73(5):662–664, 1998.

[160] Y. Hirose, A. Kahn, V. Aristov, and P. Soukiassian. Chemistry, diffusion, and electronic properties of a metal/organic semiconductor contact: In/perylenetetracarboxilic dianhydride. *Applied Physics Letters*, 68(2):217–219, 1996.

[161] S. T. Lee, Z. Q. Gao, and L. S. Hung. Metal diffusion from electrodes in organic light-emitting diodes. *Applied Physics Letters*, 75(10):1404–1406, 1999.

[162] G. Li, V. Shrotriya, J. Huang, Y. Yao, T. Moriarty, K. Emery, and Y Yang. High-efficiency solution processable polymer photovoltaic cells by self-organization of polymer blends. *Nature*, 4(11):864–868, 2005.

[163] Z. R. Hong, B. Maennig, R. Lessmann, M. Pfeiffer, K. Leo, and P. Simon. Improved efficiency of zinc phthalocyanine/C_{60} based photovoltaic cells via nanoscale interface modification. *Applied Physics Letters*, 90(20):3, 2007.

[164] S. Pfuetzner, J. Meiss, A. Petrich, M. Moritz, and K. Leo. Thick c60:znpc bulk heterojunction solar cells with improved performance by film deposition on heated substrates. *Applied Physics Letters*, 94(25):253303, 2009.

[165] S. Heutz, P. Sullivan, B. M. Sanderson, S. M. Schultes, and T. S. Jones. Influence of molecular architecture and intermixing on the photovoltaic, morphological and spectroscopic properties of cupc-c-60 heterojunctions. *Solar Energy Materials and Solar Cells*, 83(2-3):229–245, 2004.

[166] H.R. Kerp and E.E. van Faassen. Quantitative analysis of oxygen doping in zinc phthalocyanine thin films. In *Proceedings of the 11th workshop on quantum solar energy conversion - QUANTSOL'98*, 1999.

[167] H. R. Kerp and E. E. van Faasen. Effects of oxygen on exciton transport in zinc phthalocyanine layers. *Chemical Physics Letters*, 232(1-2):5–12, 2000.

[168] H. R. Kerp, K. T. Westerduin, A. T. van Veen, and E. E. van Faassen. Quantification and effects of molecular oxygen and water in zinc phthalocyanine layers. *Journal of Materials Research*, 16(2):503–511, 2001.

[169] I. G. Hill, A. Rajagopal, and A. Kahn. Energy-level alignment at interfaces between metals and the organic semiconductor 4,4'-n,n'-dicarbazolyl-biphenyl. *JAP*, 84(6):3236–3241, 1998.

[170] H. Ishii, H. Oji, N. Ito, E. amd Hayashi, D. Yoshimura, and K. Seki. Energy level alignment and band bending at model interfaces of organic electroluminescent devices. *Journal of Luminescence*, 87-89(1):61–65, 2000.

[171] H. Vázquez, W. Gao, F. Flores, and A. Kahn. Energy level alignment at organic heterojunctions: Role of the charge neutrality level. *Physical Review B*, 71(4):041306, 2005.

[172] L. Ma, J. Ouyang, and Y. Yang. High-speed and high-current density c60 diodes. *Applied Physics Letters*, 84(23):4786, 2004.

[173] P. E. Burrows, V. Bulovic, S. R. Forrest, L. S. Sapochak, D. M. McCarty, and M. E. Thompson. Reliability and degradation of organic light emitting devices. *APL*, 65(23):2922–2924, 1994.

[174] D. Kosolov, D. S. English, V. Bulovic, P. F. Barbara, S. R. Forrest, and M. E. Thompson. Direct observation of structural changes in organic light emitting devices during degradation. *JAP*, 90(7):3242–3247, 2001.

[175] L. S. Liao, J. He, X. Zhou, M. Lu, Z. H. Xiong, Z. B. Deng, X. Y. Hou, and S. T. Lee. Bubble formation in organic light-emitting diodes. *JAP*, 88(5):2386–2390, 2000.

[176] S. F. Lim, W. Wang, and S. J. Chua. Degradation of organic light-emitting devices due to formation and growth of dark spots. *Materials Science and Engineering*, B85(2-3):154–149, 2001.

[177] C. Shen and A. Kahn. The role of interface states in controlling the electronic structure of alq$_3$/reactive metal contacts. *Organic Electronics*, 2(2):89–95, 2001.

[178] H. Aziz, Z. Popovic, N. Hu, A. Hor, and G. Xu. Degradation mechanism of small molecule-based organic light-emitting devices. *Science*, 283(5409):1900, 1999.

[179] R. Meerheim, K. Walzer, M. Pfeiffer, and K. Leo. Ultrastable and efficient red organic light emitting diodes with doped transport layers. *Applied Physics Letters*, 89(6):061111, 2006.

[180] M. A. Baldo, M. E. Thompson, and S. R. Forrest. Phosphorescent materials for application to organic light emitting devices. *Pure Appl. Chem.*, 71(1):2095–2106, 1999.

[181] Hartmut Yersin. Triplet emitters for oled applications, mechanisms of exciton trapping and control of emission properties. *Top. Cur. Chem.*, 241:1–26, 2004.

[182] P. W. Atkins and Julio De Paula. *Physical chemistry.* W.H. Freeman, New York, 7^{th} edition, 2002.

[183] A. Hirsch and M. Brettreich. *Fullerenes: Chemistry and Reactions.* Wiley-VCH, 2005.

[184] Peter Peumans. Phd thesis: Organic thin-film photodiodes, princeton university. 2004.

[185] http://www.kip-sussex.co.uk/co-owner/index.html.

[186] G. Van Tendeloo, C. Van Heurck, J. Van Landuyt, S. Amelinckx, M. A. Verheijen, P. H. M. Vanloosdrecht, and G. Meijer. Phase-transitions in C_{60} and the related microstructure: A study by electron-diffraction and electron-microscopy. *Journal of Physical Chemistry*, 96(18):7424–7430, 1992.

[187] S. Behler, H. P. Lang, S. H. Pan, V. Thommen-Geiser, and R. Hofer. Low-temperature scanning tunneling microscopy study of fuleritte. *Electronic properties of fullerenes : proceedings of the international winterschool on electronic properties of novel materials, Kirchberg, Tyrol, March 6-13, 1993*, page 232, 1993.

[188] C. S. Yannoni, R. D. Johnson, G. Meijer, D. S. Bethune, and J. R. Salem. Carbon-13 NMR-study of the C_{60} cluster in the solid-state - molecular-motion and carbon chemical-shift anisotropy. *Journal of Physical Chemistry*, 95(1):9–10, 1991.

[189] Min Gu, Yening Wang, Tong Tang, Weiyi Zhang, Chen Hu, Feng Yan, and Duan Feng. The transition from the ordered to the merohedral disordered phase in oxygenated solid C_{60}. *Physics Letters A*, 223(4):273–279, 1996.

[190] G. B. M. Vaughan, P. A. Heiney, D. E. Cox, A. R. McGhie, D. R. Jones, R. M. Strongin, M. A. Cichy, and A. B. Smith. The orientational phase-transition in solid buckminsterfullerene epoxide ($C_{60}O$). *Chemical Physics*, 168(1):185–193, 1992.

[191] K. M. Kadish and Rodney S. R. *Fullerenes.* Electrochemical Society, Pennington, NJ, 1994.

[192] Karl M. Kadish and Rodney S. Ruoff. *Fullerenes.* Electrochemical Society, Pennington, NJ, 1996.

[193] K. M. Kadish and Rodney S. R. *Fullerenes : chemistry, physics, and technology.* Wiley-Interscience, New York, 2000.

[194] J. Fink, H. Kuzmany, M. Mehring, and S. Roth. *Electronic properties of fullerenes : proceedings of the international winterschool on electronic properties of novel materials, Kirchberg, Tyrol, March 6-13, 1993.* Springer series in solid-state sciences ;. Springer-Verlag, Berlin ; New York, 1993.

[195] Andreas Hirsch. *The chemistry of the fullerenes.* Thieme organic chemistry monograph series. G. Thieme Verlag, Stuttgart ; New York, 1994.

[196] H. W. Kroto, J. E. Fischer, and D. Cox. *The Fullerenes.* Pergamon, Oxford ; New York, 1^{st} edition, 1993.

[197] Y. Wang, J. M. Holden, A. M. Rao, P. C. Eklund, U. D. Venkateswaran, D. Eastwood, E. L. Lidberg, G. Dresselhaus, and M. S. Dresselhaus. Optical absorption and photoluminescence in pristine and photopolymerized C_{60} solid films. *Physical Review B*, 51(7):4547–4556, 1995.

[198] K. Németh P.R. Surján and L. Udvardi. Jahn-teller distorted excited states of c_{60}. *Electronic properties of fullerenes : proceedings of the international winterschool on electronic properties of novel materials, Kirchberg, Tyrol, March 6-13, 1993*, page 126, 1993.

[199] Q. S. Xie, E. Perezcordero, and L. Echegoyen. Electrochemical detection of ${C_{60}}^{(6-)}$ and ${C_{70}}^{(6-)}$ - enhanced stability of fullerides in solution. *Journal of the American Chemical Society*, 114(10):3978–3980, 1992.

[200] C. A. Reed and R. D. Bolskar. Discrete fulleride anions and fullerenium cations. *Chemical Reviews*, 100(3):1075–1120, 2000.

[201] O. V. Molodtsova and M. Knupfer. Electronic properties of the organic semiconductor interfaces CuPc / C_{60} and C_{60} / CuPc. *Journal of Applied Physics*, 99(5):053704, 2006.

[202] Y. Ge and J. E. Whitten. Energy level alignment between sexithiophene and buckminsterfullerene films. *Chemical Physics Letters*, 448(1-3):65–69, 2007.

[203] Th.B. Singh, N. Marjanović, G.J. Matt, S. Günes, N.S. Sariciftci, A. Montaigne Ramil, A. Andreev, H. Sitter, Schwödiauer R., and S. Bauer. High-mobility n-channel organic field-effect transistors based on epitaxially grown C_{60} films. *Organic Electronics*, 6(3):105–110, 2005.

[204] L. Ma, J. Ouyang, and Yang Y. High-speed and high-current density C_{60} diodes. *Applied Physics Letters*, 84(23):4786–4788, 2004.

[205] A. Tapponnier, I. Biaggio, and P. Gunter. Ultrapure c_{60} field-effect transistors and the effects of oxygen exposure. *Applied Physics Letters*, 86(11):112114, 2005.

[206] H. Werner, M. Wohlers, D. Bublak, T. Belz, and W. Bausch. Chemical and structural aspects of the interaction between c_{60} and molecular oxygen. In *Electronic properties of fullerenes : proceedings of the international winterschool on electronic properties of novel materials, Kirchberg, Tyrol*, 1993.

[207] G. H. Kroll, P. J. Benning, Y. Chen, T. R. Ohno, J. H. Weaver, L. P. F. Chibante, and R. E. Smalley. Interaction of O_2 with C_60 - photon-induced oxidation. *Chemical Physics Letters*, 181(2-3):112–116, 1991.

[208] A. Ito, T. Morikawa, and T. Takahashi. Photoinduced polymerization and oxidation of c-60 observed by photoelectron-spectroscopy. *Chemical Physics Letters*, 211(4-5):333–336, 1993.

[209] S. Lebedkin, S. Ballenweg, J. Gross, R. Taylor, and W. Kratschmer. Synthesis of $c_{120}O$ - a new dimeric [60]fullerene derivative. *Tetrahedron Letters*, 36(28):4971–4974, 1995.

[210] A. Gromov, S. Lebedkin, S. Ballenweg, A. G. Avent, R. Taylor, and W. Kratschmer. C120o2: The first [60]fullerene dimer with cages bis-linked by furanoid bridges. *Chemical Communications*, (2):209–210, 1997.

[211] A. Gromov, S. Ballenweg, S. Giesa, S. Lebedkin, W. E. Hull, and W. Kratschmer. Preparation and characterisation of C_{119}. *Chemical Physics Letters*, 267(5-6):460–466, 1997.

[212] N. Hayashi, N. K. Kanai, Y. Ouchi, and K. Seki. Ultrahigh vacuum seebeck effect and conductivity measurements on n-doping of C_{60} films. In *MRS Fall meeting*, 2007.

[213] H. W. Kroto. The stability of the fullerenes C_n, with n=24, 28, 32, 36, 50, 60 and 70. *Nature*, 329(6139):529–531, 1987.

[214] Neil Bruce McKeown. *Phthalocyanine Materials: Synthesis, Structure and Function.* Cambridge University Press, 1998.

[215] Arthur Louis Thomas. *Phthalocyanine Research and Applications.* CRC Press, 1990.

[216] Ichiro Okura. *Photosensitization of Porphyrins and Phthalocyanines.* Gordon & Breach, 2001.

[217] S. Senthilarasu, S. Velumani, R. Sathyamoorthy, A. Subbarayan, J. A. Ascencio, G. Canizal, P. J. Sebastian, J. A. Chavez, and R. Perez. Characterization of zinc phthalocyanine (ZnPc) for photovoltaic applications. *Applied Physics A-Materials Science & Processing*, 77(3-4):383–389, 2003.

[218] K. Kajihara, K. Tanaka, Hrao K., and N. Soga. Photovoltaic effect in titanium dioxide / zinc phthalocyanine cell. *Japanese Journal of Applied Physics*, 35(12A):6110–6116, 1996.

[219] D. Frackowiak, A. Planner, A. Waszkowiak, A. Boguta, R-M. Ion, and K. Wiktorowicz. Yield of intersystem (singlet-triplet) crossing in phthalocyanines evaluated on the basis of a time in resolved photothermal method. *Journal of Photochemistry A: Chemistry*, 141(2-3):101–108, 2001.

[220] W. Gao and A. Kahn. Controlled p-doping of zinc phthalocyanine by coevaporation with tetrafluorotetracyanoquinodimethane: A direct and inverse photoemission study. *Applied Physics Letters*, 79(24):4040, 2001.

[221] J.P. Meyer, D. Schlettwein, D. Wöhrle, and J. I. Jaeger. Charge transport in thin films of molecular semiconductors as investigated by measurements of thermoelectric power and electrical conductivity. *Thin Solid Films*, 258(1-2):317–324, 1995.

[222] Martin Pfeiffer. Controlled doping of organic vacuum deposited dye layers: Basics and applications. 1999. PhD Thesis, Technische Universität Dresden.

[223] F.T. Reis, D. Mencaraglia, S. O. Saad, I. Séguy, M. Oukachmih, P. Jolinat, and P. Destruel. Characterization of ITO/CuPc/Al and ITO/ZnPc/Al structures using optical and capacitance spectroscopy. *Synthetic Metals*, 138(1-2):33–37, 2003.

[224] Q. Zhou and R.D Gould. The effects of oxygen doping and annealing on the surface and bulk electrical conductivity in planar copper phthalocyanine thin films for gas-sensing applications. *Thin Solid Films*, 317(1-2):432–435, 1998.

[225] T. G. Abdel-Malik. Effect of oxygen on the electrical properties of zinc phthalocyanine single crystals. *Physica Status Solidi A*, 76(2):K159–K162, 1983.

[226] A. K. Sobbi, D. Wöhrle, and D. Schlettwein. Photochemical stability of various porphyrins in solution and as thin-film electrodes. *Journal of the Chemical Society-Perkin Transactions 2*, (3):481–488, 1993.

[227] A. Barbon, M. Brustolon, and E. E. van Faassen. Photoexcited spin triplet states in zinc phthalocyanine studied by transient EPR. *Phys. Chem. Chem. Phys*, 3(3):5342–5347, 2001.

[228] M. Pfeiffer, K. Leo, X. Zhou, J. S. Huang, M. Hofmann, A. Werner, and J. Blochwitz-Nimoth. Doped organic semiconductors: Physics and application in light emitting diodes. *Organic Electronics*, 4(2-3):89–103, 2003.

[229] Steffen Pfützner. Untersuchung des Ladundsträgertransports in transparenten p-Transportmaterialien für organische pin-Solarzellen. dec 2007. Diploma Thesis, Technische Universität Dresden.

[230] http://www.gnuplot.info, from 05.10.2008.

[231] http://www.python.org, from 05.10.2008.

[232] A. Kaminski, J.J. Marchand, A. Fave, and A. Laugier. New method of parameters extraction from dark I-V curve. *IEEE 26th PVSC*, 1997.

[233] M. B. Prince. Silicon solar energy converters. *Journal of Applied Physics*, 26(5):534, 1955.

[234] S. Sze. *Physics of Semiconductor Devices*. John Wiley & Sons, 2nd edition, 1981.

[235] M. Galassi, J. Davies, J. Theiler, B. Gough, G. Jungman, M. Booth, and F. Rossi. *GNU Scientific Library Reference Manual*. 2006.

[236] G. Williams and D. C. Watts. Non-symmetrical dielectric relaxation behaviour arising from a simple empirical decay function. *Transactions of the Faraday Society*, 66(565P):80, 1970.

[237] R. Kohlrausch. Theorie des elektrischen ruckstandes in der leidener flasche. *Annalen der Physik und Chemie*, 91(2):179–214, 1854.

[238] M. Cardona, R.V. Chamberlin, and Marx W. The history of the stretched exponential function. *Annalen der Physik*, 16(12):842–845, 2007.

[239] M. Berberan-Santos, E.N. Bodunov, and Valeur B. History of the kohlrausch (stretched exponential) function: Pioneering work in luminescence. *Annalen der Physik*, 17(7):460–461, 2008.

[240] W. Weibull. A statistical distribution function of wide applicability. *Journal of Applied Mechanics*, 18(3):293–297, 1951.

[241] S. Bailey, D. Brinker, H. Curtis, P. Jenkins, and D. Scheiman. Solar cell calibration and measurement techniques. *32nd Intersociety Energy Conversion Engineering Conference*, page 412, 1997.

[242] J. Metzdorf, S. Winter, and T. Wittchen. Radiometry in photovoltaics: calibration of reference solar cells and evaluation of reference values. *Metrologia*, 37(5):573–578, 2000.

[243] H. Mullejans, A. Ioannides, R. Kenny, W. Zaaiman, H. A. Ossenbrink, and E. D. Dunlop. Spectral mismatch in calibration of photovoltaic reference devices by global sunlight method. *Measurement Science & Technology*, 16(6):1250–1254, 2005.

[244] S. Scholz, C. Corten, K. Walzer, D. Kuckling, and K. Leo. Photochemical reactions in organic semiconductor thin films. *Org. Electronics*, 8(6):709, 2007.

[245] S. Krauter and R. Hanitsch. Actual optical and thermal performance of PV-modules. *Solar Energy Materials and Solar Cells*, 41-42(1):557–574, 1996.

[246] http://sdcc.sourceforge.net, from 06.10.2008.

[247] F. Yang, M. Shtein, and S. Forrest. Controlled growth of a molecular bulk heterojunction photovoltaic cell. *Nature Materials*, 4(1):37–41, 2005.

[248] J. G. Xue, B. P. Rand, S. Uchida, and S. R. Forrest. A hybrid planar-mixed molecular heterojunction photovoltaic cell. *Advanced Materials*, 17(1):66–71, 2005.

[249] D. W. Owens, C. M. Aldao, D. M. Poirier, and J. H. Weaver. Charge-transfer, doping, and interface morphologies for al-c-60. *Physical Review B*, 51(23):17068–17072, 1995.

[250] J. K. Baral, H. S. Majumdar, A. Laiho, H. Jiang, E. I. Kauppinen, R. A. Ras, J. Ruokolainen, O. Ikkala, and R. Osterbacka. Organic memory using [6,6]-phenyl-C_{61} butyric acid methyl ester: morphology, thickness and concentration dependence studies. *Nanotechnology*, 19(3), 2008.

[251] Z. R. Hong, Z. H. Huang, and X. T. Zeng. Investigation into effects of electron transporting materials on organic solar cells with copper phthalocyanine/C_{60} heterojunctions. *Chemical Physics Letters*, 425(1-3):62–65, 2006.

[252] P. Peumans, A. Yakimov, and S. R. Forrest. Small molecular weight organic thin-film photodetectors and solar cells. *Journal of Applied Physics*, 93(7):3693–3723, 2003.

[253] M. Vogel, S. Doka, C. Breyer, M. C. Lux-Steiner, and K. Fostiropoulosa. On the function of a bathocuproine buffer layer in organic photovoltaic cells. *Applied Physics Letters*, 89(16):163501, 2006.

[254] M. Y. Chan, C. S. Lee, S. L. Lai, M. K. Fung, F. L. Wong, H. Y. Sun, K. M. Lau, and S. T. Lee. Efficient organic photovoltaic devices using a combination of exciton blocking layer and anodic buffer layer. *Journal of Applied Physics*, 100(9):023504, 2006.

[255] S. Toyoshima, K. Kuwabara, T. Sakurai, T. Taima, K. Saito, H. Kato, and K. Akimoto. Electronic structure of bathocuproine on metal studied by ultraviolet photoemission spectroscopy. *Japanese Journal of Applied Physics Part 1-Regular Papers Brief Communications & Review Papers*, 46(4B):2692–2695, 2007.

[256] K. Suemori, Y. Matsumura, M. Yokoyama, and M. Hiramoto. Large area organic solar cells with thick and transparent protection layers. *Japanese Journal of Applied Physics*, 45(17):L472–L474, 2006.

[257] H. Y. Fu, Q. L. Song, X. Y. Huo, F. Xiao, and B. X. Shao. Photovoltaic characteristics of a naphthylamine derivative. *Chinese Journal of Chemistry*, 25(9):1242–1245, 2007.

[258] B. P. Rand, J. Li, J. G. Xue, R. J. Holmes, M. E. Thompson, and S. R. Forrest. Organic double-heterostructure photovoltaic cells employing thick tris(acetylacetonato)ruthenium(III) exciton-blocking layers. *Advanced Materials*, 17(22):2714–2718, 2005.

[259] Ronny Timmreck. Elektron-loch-koversionskontakte in organischen tandemsolarzellen. 2007. Diploma Thesis, Technische Universität Dresden.

[260] Karsten Fehse, Selina Olthof, Karsten Walzer, Karl Leo, Robert L. Johnson, Hendrik Glowatzki, Benjamin Broker, and Norbert Koch. Energy level alignment of electrically doped hole transport layers with transparent and conductive indium tin oxide and polymer anodes. *Journal of Applied Physics*, 102(7):073719, 2007.

[261] M.L. Wang, Q.L. Song, H.R. Wu, B.F. Ding, X.D. Gao, X.Y. Sun, X.M. Ding, and X.Y. Hou. Small-molecular organic solar cells with C_{60} / Al composite anode. *Organic Electronics*, 8(4):439–444, 2007.

[262] J. Blochwitz, T. Fritz, M Pfeiffer, K. Leo, D. M. Alloway, P.A. Lee, and N.R. Armstrong. Interface electronic structures of controlled doped organic semiconductors. *Organic Electronics*, 2(2):97–104, 2001.

[263] Jun Yeob Lee. Efficient hole injection in organic light-emitting diodes using C_{60} as a buffer layer for Al reflective anodes. *Applied Physics Letters*, 88(7):073512, 2006.

[264] S. Forrest, P. Burrows, M.E. Thompson, and V. Bulovic. Organic light emitting device containing a hole injection enhancement layer. (US Patent 5998803), 1999.

[265] A. Rajagopal, C. I. Wi, and A. Kahn. Energy level offset at organic semiconductor heterojunctions. *Journal of Applied Physics*, 83(5):2649–2655, 1998.

[266] J. R. Ostrick, A. Dodabalapur, L. Torsi, A. J. Lovinger, E. W. Kwock, T. M. Miller, M. Galvin, M. Berggren, and H. E. Katz. Conductivity-type anisotropy in molecular solids. *Journal of Applied Physics*, 81(10):6804–6808, 1997.

[267] T. Taima, S. Toyoshima, K. Hara, K. Saito, and K. Yase. Control of measurement environments for high-efficiency organic photovoltaic cells. *Japanese Journal of Applied Physics Part 2-Letters & Express Letters*, 45(8-11):L217–L219, 2006.

[268] A. R. V. Benvenho, R. Lessmann, I. A. Hummelgen, R. M. Q. Mello, R. W. C. Li, F. F. C. Bazito, and J. Gruber. Physical and chemical characterization of poly(2-bromo-5-hexyloxy-p-phenylenevinylene) and poly(5,5 '-dibromo-2,2 '-bis-hexyloxy-4,4 '-biphenylenevinylene) - comparison to related polymers. *Materials Chemistry and Physics*, 95(1):176–182, 2006.

[269] M. Wohlers, A. Bauer, Th. Rühle, F. Neitzel, H. Werner, and R. Schlögl. The dark reaction of C_{60} and of C_{70} with molecular oxygen at atmospheric pressure and temperatures between 300 K and 800 K. *Fullerenes, Nanotubes and Carbon Nanostructures*, 5(1):49–83, 1997.

[270] J. Drechsel, B. Männig, D. Gebeyehu, M. Pfeiffer, and H. Hoppe. Mip-type organic solar cells incorporating phthalocyanine/fullerene mixed layers and doped wide-gap transport layers. *Organic Electronics*, 5(4):175–186, 2004.

[271] R. Png, P. Chia, S. Sivaramakrishnan, L. Wong, M. Zhou, L. Chua, and P. K. Ho. Electromigration of the conducting polymer in organic semiconductor devices and its stabilization by cross-linking. *Applied Physics Letters*, 91(1):013511, 2007.

[272] M. O. Reese, A. J. Morfa, M. S. White, N. Kopidakis, S. E. Shaheen, G. Rumbles, and D. S. Ginley. Pathways for the degradation of organic photovoltaic P3HT : PCBM based devices. *Solar Energy Materials and Solar Cells*, 92(7):746–752, 2008.

[273] S. Tokito, H. Tanaka, K. Noda, A. Okada, and Y. Taga. Thermal stability in oligomeric triphenylamine/tris(8-quinolinolato) aluminum electroluminescent devices. *Applied Physics Letters*, 70(15):1929, 1997.

List of publications

2009 R. Lessmann, Z. R. Hong, S. Scholz, B. Maennig, M. K. Riede, K. Leo. Degradation of ZnPc / C_{60} photovoltaic cells. to submit

2009 V. Kažukauskas, A. Arlauskas, M. Pranaitis, R. Lessmann, M. Riede, K. Leo. Characterization of effective charge carrier mobility in ZnPc/C_{60} Solar Cells after ageing. Submitted to Physica Status Solidi.

2009 Z. Hong, R. Lessmann, B. Maennig, Q. Huang, K. Harada, M. Riede, K. Leo. Antenna effects and improved efficiency in multiple heterojunction photovoltaic cells based on pentacene, zinc phthalocyanine and C_{60}. Journal of Applied Physics. v. 106. pp. 064511

2007 Z. Hong, B. Männig, R. Lessmann, M. Pfeiffer, K. Leo, P. Simon. Improved efficiency of zinc phthalocyanine/C_{60} based photovoltaic cells via nanoscale interface modification. Applied Physics Letters, v. 90, pp. 203505.

Appendix

8.1 Derivation of the Arrhenius relation for the activation energy

The Arrhenius equation (below) is an empirical relation for the dependency of the rate constant of a chemical reaction (k) on the absolute temperature (T) and the activation energy (E_A).

$$k = A' exp(-E_A/RT) \tag{8.1}$$

where A is the exponential prefactor and R is the ideal gas constant. The next steps transforms the equation in its logarithmic form.

$$ln(k) = ln(A' exp(-E_A/RT)) \tag{8.2}$$

using $ln(X_1X_2) = ln(X_1) + ln(X_2)$, we get:

$$ln(k) = ln(A') - ln(exp(E_A/RT)) \tag{8.3}$$

$$ln(k) = ln(A') - E_A/RT \tag{8.4}$$

A' is the exponential pre-factor, therefore $ln(A')$ is also constant. Making $ln(A') = B'$, one can write:

$$ln(k) = B' - E_A/RT \tag{8.5}$$

making the derivative:

$$\partial(ln(k)) = \partial(B' - E_A/RT) \tag{8.6}$$

using:

$$\partial(X_1 + X_2) = \partial(X_1) + \partial(X_2) \tag{8.7}$$

$$\partial(ln(k)) = \partial(B') - \partial(E_A/RT) \tag{8.8}$$

since:

$$\partial(Constant) = 0 \tag{8.9}$$

$$\partial(ln(k)) = -\partial(E_A/RT) \tag{8.10}$$

E_A and R are constants and can be taken out of the derivative. Now the relation can be arranged in a more convinient form:

$$\partial(ln(k)) = -(E_A/R)\partial(1/T) \tag{8.11}$$

$$\frac{\partial(ln(k))}{\partial(1/T)} = -(E_A/R) \tag{8.12}$$

Equation 8.1 is the definition of the activation energy.

$$-R\frac{\partial(ln(k))}{\partial(1/T)} = E_A \tag{8.13}$$

8.2 Sign convention of the energy quantities used in this work

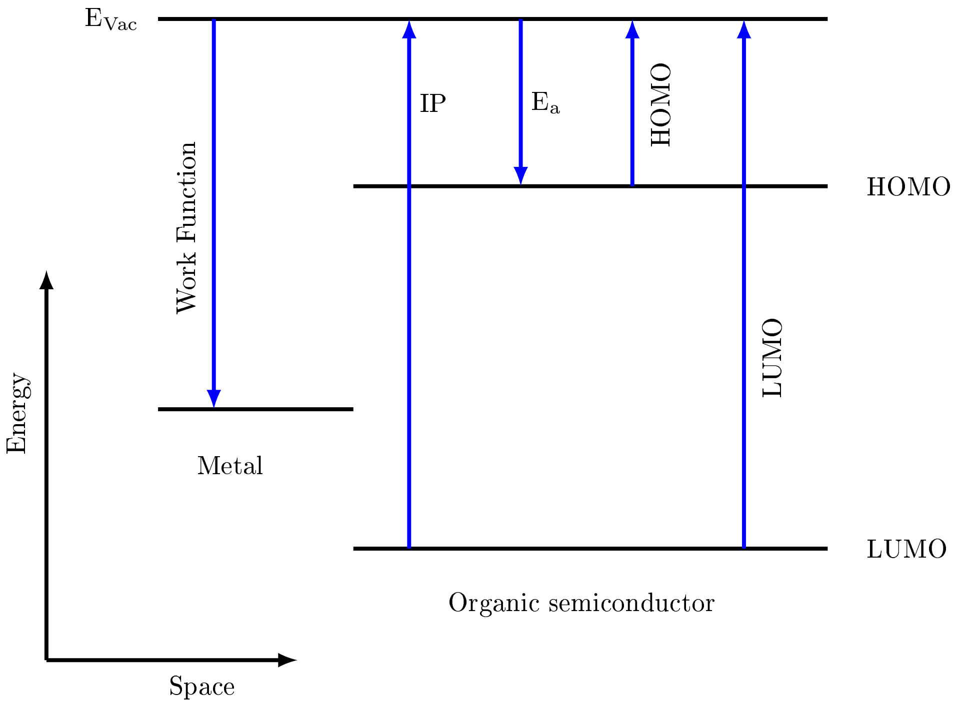

Figure 8.1: Energy diagram showing the sign convention of the physical quantities used to describe the characteristic energy values for metal and organic semiconductors.

The description of energy values follows the definition of the physical quantities. Still, confusion is found in literature, e.g. HOMO and LUMO are often written as positive values. In this work, the energy levels are used in agreement with Fig. 8.1. HOMO, LUMO, and electron affinity are negative values. The ionization potential is a positive value, as well as the work function of a metal.

8.3 Notation of device structure

The device structure are written a sequence of layers, separated by a "/". The layer thickness is given in brackets "()" and the values are in nanometers. The susbstrate, if not explicitly written, is glass. The ITO layer thickness is always 90 nm.

An example:

$$\text{ITO / ZnPc (20) / } C_{60} \text{ (40) / Al (100)}$$

is a device made on a glas substrate, where the cathode is a 90 nm thick ITO layer, the ZnPc layer is 20 nm thick, the C_{60} layer is 40 nm thick and the anode is 100 nm thick.

8.3.1 Code fragment of the fitting functions

The following code is a fragment from the file ivfit.cpp, showing how to initialize the GnuScientificLibrary (GSL) solver and how to execute the fit.

```
/*
Source code fragment with implementation of the fitting functions of Shockley
derivated equations.
This functions initialize the GSL solver
The function calls for matrix operations are made to the GSL functions

Initialization functions:
 ufi_shockley1()
 derivufi_forward()
 ufiderivufi_shockley1()

Fitting function:
 fitsaturation()

RL 2007
*/

struct data{ // Data structure for the I,V values
  size_t n;
//  size_t p;
  double * x; // pointer to array, Voltage values
  double * y; // pointer to array, Current values
  double * js; // pointer to constant shunt current
  double * T; // pointer to constant Temperature
  double * sigma;//weighting data
//  const char *function;
//  const char *names;
};

double sccurr;
double Texp = 75; // Temperature used in the experiments

/*************************************************************************/
/*                        Fitting Equations                              */
/*************************************************************************/
/*  Forward Current, U = ln_{{j-j_l}/{j_s} + 1 } {nkT}/{q} + jR_s
  *x    - is used for the constants
  *data - is used for the I,V data
  *f    - is the GSL vector
*/
int ufi_forward (const gsl_vector * x, void *data, /*double *xdt,*/ gsl_vector *f)
```

```
{
  size_t n       = ((struct data *)data)->n;
  double *y      = ((struct data *)data)->y;
  double *sigma = ((struct data *)data)->sigma;
  double *xp     = ((struct data *)data)->x;
  double  T      = *((struct data *)data)->T;
  double js      = gsl_vector_get (x, 0);
  double rs      = gsl_vector_get (x, 1);
  double m       = gsl_vector_get (x, 2);

//   cout << "jsc = " << sccurr << ", ";

  size_t i;
//cout << endl << "----------" << endl;
for (i = 0; i < n; i++)
  {
    double j = xp[i];
    double Yi = log(fabs((j-sccurr)/js + 1))*(k*T*m/q) + j*rs;
//   cout << j << "," << sccurr << "," << Yi << "," << y[i] << "," << sigma[i] << "), (";
    gsl_vector_set (f, i, (Yi - y[i])/sigma[i]);
  }
  return GSL_SUCCESS;
}

int derivufi_forward (const gsl_vector * x, void *data, gsl_matrix *J)
{
  size_t n       = ((struct data *)data)->n;
  double *y      = ((struct data *)data)->y;
  double *sigma = ((struct data *)data)->sigma;
  double *xp     = ((struct data *)data)->x;
  double  T      = *((struct data *)data)->T;

  double js      = gsl_vector_get (x, 0);
  double rs      = gsl_vector_get (x, 1);
  double m       = gsl_vector_get (x, 2);

  size_t i;

  int ii, j;

// sccurr = -5.22389226804384e-05;

for (i = 0; i < n; i++)
  {
           /* Jacobian matrix J(i,j) = dfi / dxj, */
           /* where fi = (Yi - yi)/sigma[i],       */
```

```
           /*        Yi = A * exp(-lambda * i) + b   */
           /* and the xj are the parameters (A,lambda,b) */
  double j = xp[i];
  double kTbyq = (k*T/q);
  double s = sigma[i];

    gsl_matrix_set (J, i, 0, -( kTbyq*m / (j-sccurr+js) )/s );
    gsl_matrix_set (J, i, 1, j/s );
    gsl_matrix_set (J, i, 2,  ( kTbyq*log( fabs(((j-sccurr)/js)+1 )) )/s );
  }

int ufiderivufi_forward (const gsl_vector * x, void *data, gsl_vector *f, gsl_matrix *J)
{
 ufi_forward       ( x, data, f);
 derivufi_forward ( x, data, J);
return GSL_SUCCESS;
}

/* Initialize all the variables and call the GSL solver function */
void ivfit::fitsaturation(gsl_multifit_function_fdf &f, meas_param_t *result, double *x_init,
              double &pjl, double &pjs, double &prp, double &pm, double &pchi, int lverbosity)
{

  double *xp = NULL;
  double *y = NULL;
  size_t iter = 0;
  int status;

 const size_t p = 3;

 gsl_vector_view x = gsl_vector_view_array (x_init, p);
 gsl_matrix *covar = gsl_matrix_alloc (p, p);

//cout << "datalen = " << f.n << endl;
  xp = ((struct data *)f.params)->x;
  if ((xp == NULL) || (result == NULL)) { cout << "fitsaturation():␣NULL␣pointer␣detected" << e
  y = ((struct data *)f.params)->y;

// Confirm that data is there:
// cout << "------------" << endl;
// for ( int i=0; i<f.n; i++ )
//      cout << "(pos;i;v) = (" << i << ";" << y[i] << ";" << xp[i] << ")" << endl;

// set functions to fit
 f.f   = &ufi_shockley1;
 f.df  = &derivufi_forward;
```

```
 f.fdf = &ufiderivufi_shockley1;
 f.p   = p;

// init fitting
 const gsl_multifit_fdfsolver_type *Tt;
 gsl_multifit_fdfsolver *s;

 Tt = gsl_multifit_fdfsolver_lmsder;
 s = gsl_multifit_fdfsolver_alloc ( Tt, f.n, p);
 gsl_multifit_fdfsolver_set (s, &f, &x.vector);

if (lverbosity > 15)  print_state (iter, s);
//cout << " -- init solver -- " << endl;
// check code below

int sls;

       do
         {
           iter++;
           status = gsl_multifit_fdfsolver_iterate (s);

if (lverbosity > 15)   printf ("␣status␣=␣%s\n", gsl_strerror (status));
if (lverbosity > 15)   print_state (iter, s);

           status = gsl_multifit_test_delta (s->dx, s->x,
                                            1e-4, 1e-4);
         }
       while ((status == GSL_CONTINUE) && (iter < 1000));

       gsl_multifit_covar (s->J, 0.0, covar);

     #define FIT(i) gsl_vector_get(s->x, i)
     #define ERR(i) sqrt(gsl_matrix_get(covar,i,i))

       {
         double chi = gsl_blas_dnrm2(s->f);
         double dof = f.n - p;
         double c = GSL_MAX_DBL(1, chi / sqrt(dof));

if (lverbosity > 15)  printf("chisq/dof␣=␣%g\n",  pow(chi, 2.0) / dof);
if (lverbosity > 15)  printf ("A␣␣␣␣␣␣=␣%.5f␣+/-␣%.5f\n", FIT(0), c*ERR(0));

pjs =  gsl_vector_get (s->x, 0);
prp =  gsl_vector_get (s->x, 1);
pm  =  gsl_vector_get (s->x, 2);
```

```
pchi = pow(chi, 2.0) / dof;

        }

if (lverbosity > 15)  printf ("status␣=␣%s\n", gsl_strerror (status));

 gsl_matrix_free (covar);
 gsl_multifit_fdfsolver_free (s);

}
```

8.4 List of source code for the microcontroller

The following shows the firmware source code for the microcontroller PIC16f628. The sample code in section 8.4.5 shows a peace of code for an error free serial communication.

8.4.1 Source code for the microcontroller PIC 16f628 - portmap.h

```
/*
  PIC Port Connection
PORTA
MSB   Signal          Set High    Set Low     Read Mask    PIN
  0 - pic clock                                            16 -- RA7
  1 - pic clock                                            15 -- RA6
  2 - ADC Data                                 &= 0x20     4  i  RA5
  3 - ADC CLK         |= 0x10     &= 0xef                  3  io RA4
  4 - DAC Data        |= 0x08     &= 0xf7                  2  io RA3
  5 - DAC CLK         |= 0x04     &= 0xfb                  1  io RA2
  6 - ADC CS          |= 0x02     &= 0xfd                  18 io RA1
  7 - Relay CLK       |= 0x01     &= ~0x01                 17 io RA0
PORTB
MSB   Signal          Set High    Set Low     Read Mask    PIN
  0 - relay data      |= 0x80     &= ~0x80                 13 io RB7
  1 - relay data      |= 0x40     &= ~0x40                 12 io RB6
  2 - relay data      |= 0x20     &= ~0x20                 11 io RB5
  3 - LED ON          |= 0x10     &= 0xef                  10 io RB4
  4 - LED ON          |= 0x08     &= 0xf7                  9  io RB3
  5 - serial          |= 0x04     &= 0xfb                  8  tx RB2
  6 - serial          |= 0x02     &= 0xfd                  7  rx RB1
  7 - DAC Sync        |= 0x01     &= 0xfe                  6  io RB0
*/
// Set High Mask
#define ADC_DATA  0x20
// to be OR'ed
```

```
#define ADC_CLK   0x10
#define ADC_CS    0x02
#define DAC_SYNC  0x01
#define DAC_DATA  0x08
#define DAC_CLK   0x04
```

8.4.2 Source code for the microcontroller PIC 16f628 - lt16mhzb.c

```
/*
  compile:       sdcc -mpic14 -p16f628 lt16mhzb.c
  burn:          pp -p /dev/usb/ttyUSB0 -d 16f628 -w lt16mhzb.hex
  version 07.april.2008
  Rudolf Lessmann
*/
#include "portmap.h"
/* Define processor and include header file. */
#define __16f628
#include"pic/pic16f628.h"
#define clock_speed  16000000
/* Define device name and version */
#ifndef BOX_VERSION
#define BOX_VERSION 02
#endif
#ifndef BOX_SNP1
#define BOX_SNP1     00
#endif
#ifndef BOX_SNP2
#define BOX_SNP2     10
#endif
/* Calibration for ADC */
#ifndef ADCFACT0
#define ADCFACT0  0x0f
#define ADCFACT1  0xae
#define ADCFACT2  0x83
#define ADCFACT3  0x5e
#endif
/* PIC configuration flags */
/* XT oscillator: Crystal/resonator on RA4/OSC2/CLKOUT and RA5/OSC1/CLKIN */
typedef unsigned int config;
config at 0x2007 __CONFIG = _CP_OFF &
                            _WDT_ON &
                            _BODEN_OFF &
                            _PWRTE_OFF &
                            _ER_OSC_CLKOUT &
                            _MCLRE_OFF &
                            _LVP_OFF &
                            _HS_OSC;
```

```
 /* serial data */
 unsigned char rs_data;
/* general variables */
 unsigned char tempc;
 unsigned char i, j, k;
/* Shadow ports */
 unsigned char PORTA_TMP;
 unsigned char PORTB_TMP;
// INPUT DAC LIMIT ON RS232
 unsigned long tempdac;
/* Clear Watchdog timer */
#define ClrWdt()          do { _asm clrwdt _endasm; } while(0)
#define end_timer  T0CS = 1; /* disable timer */
/* loop control variables */
 unsigned char adquire;
 unsigned char control2;
 unsigned char control3;
 unsigned char doclk;
/* variable for fast 8/32-bit conversion */
typedef union { // This compiler uses byte alignment so we can use
              unsigned int w;
       struct {
               unsigned char b1; // LSB
               unsigned char b0; // MSB byte
              }b;
             } iohw_union16;
typedef union { // This compiler uses byte alignment so we can use
              unsigned long w; // a union for fast 8/32-bit conversion
       struct {
               unsigned char b3; // LSB byte
               unsigned char b2;
               unsigned char b1;
               unsigned char b0; // MSB byte
              }b;
             } iohw_union32;
/* Variables for communication with DAC */
 extern iohw_union16 DAC;
 extern iohw_union16 DAC_LIMIT;
 extern iohw_union32 ADC;
 iohw_union32 tsetpoint;
 extern unsigned char adct_last[2];
 extern unsigned char b1, b2, b3;
 extern unsigned char ferror;
 extern void read_SYNCADC();
 extern void superfoo();
 extern void rs_putc();
```

```
 extern void del7us();
// Set ADC into external clk mode
#define adcintoexternalclock PORTA_TMP = PORTA; \
 PORTA_TMP &= 0x10; \
 PORTA_TMP |= 0x02; \
 PORTA = PORTA_TMP; \
 PORTA_TMP &= 0xfd; \
 PORTA = PORTA_TMP;
#include "t16dac.c"  /* DAC communication functions */
void correct();
void main(void) {
      INTCON = 0;  // Disable all ints !
    while (GIE != 0)
        GIE = 0; // No interrupts
      INTCON = 0; // Clear all interrupt masks
      PIE1 = 0;   // Clear all interrupt masks
//  ********  Clear all possible interrupts enable flags !
// Configure WDT
      PSA = 1;
      PS0 = 1;
      PS1 = 1;
      PS2 = 1;
      CMCON = 0x07;  /* disable comparators */
      T0CS = 0;      /* Internal clk for timer0, liberate RA4 !! */
      VREN = 0;      /* reference voltage is power down */
      VROE = 0;      /* ref voltage is disconected */
      TMR1ON = 0;    /* Disable timer 1 */
//  PORTB = 0;  // Suppose the initial state is 0...
//  PORTA = 0;
      TRISA = 0x20;   /* all output, RA5 Input */
      TRISB = 0x06;   /* RB7-4 output RB2/TX, RB1/RX */
      NOT_RBPU = 1;  /* (negated) turn off all internall pull-ups */
  /*
    Configuration modes for TRISB
    xxxx x00x TX disable, RX disable - does not work for receiving
    xxxx x01x TX disable, RX enable  x
    xxxx x10x TX enable,  RX disable - does not work for receiving
    xxxx x11x TX enable,  RX enable x
  */
// must stay high, otherwise ADC changes to external clock mode
     PORTA_TMP = 0x08;
     PORTA = 0x08;
     PORTB_TMP = 0;
     PORTB = 0;
// Init USART
      BRGH = 1; // High speed mode 1
```

```
        SPBRG = 103; // 9600 baud, high speed, Fosc=16Mhz  103
        TX9 = 0;  // 8 bit ransmission
        RX9 = 0;  // 8 bit reception
 // transmit disable,
// if transmission is enable, tx and rx does not work any more !
        TXEN = 0;
        CREN = 1; // Enable continuous receive
        ADEN = 0; // Disables address detection
        SYNC = 0; // Asynchronous mode
        RCIF = 0;
        RCIE = 0; // No interrupt
        TXIE = 0;
        GIE = 0; // No interrupts
        ClrWdt();
        DAC_LIMIT.w = 0;
      RCIE = 1; // Enable Rs232 interrupt
      TXIE = 0;
      PEIE = 1; // peripheral int mask
      GIE = 1;  // Enable Interrupts
      SPEN = 1; // Enable serial port
       PORTA_TMP = PORTA;
       PORTA_TMP |= 0x02;
       PORTA = PORTA_TMP;
       PORTA_TMP &= 0xfd;
       PORTA = PORTA_TMP;
      adcintoexternalclock;
// put analog channels in tri-state
      PORTB_TMP &= 0x1F;      // POSITION 8 is OPEN, FLOATING CONTACT, DISCONNECTED
      PORTB_TMP |= 0xE0;
      PORTB = PORTB_TMP;
      PORTA_TMP |= 0x01;
      PORTA = PORTA_TMP;
      superfoo();
      PORTA_TMP &= ~0x01;
      PORTA = PORTA_TMP;
//
      control2 = 0;
      control3 = 0;
      adquire = 0;
      ferror = 0;
          doclk=1;
/* ############### MAIN LOOP ################ */
while (1==1) {
      if ((adquire==2)||(control3!=0)) {
        GIE=0;
           ClrWdt();
```

```
            write_DAC();
            ClrWdt();
            adquire=0;
        GIE=1;
     }
superfoo(); // delay
     if ((adquire==1)||(control3!=0))
     {
         ClrWdt();
         GIE=0;
         {
                 ClrWdt();
             read_SYNCADC();
                 ClrWdt();
             }
         adquire = 0;
         GIE=1;
     }
     ClrWdt();
superfoo(); // delay
     if (control3 != 0)
     {
         if (control2 > 10)
         {
             adquire = 2;
             ClrWdt();
             correct();
             control2 = 0;
             ClrWdt();
         }
     control2++;
     }
     }
}
unsigned char correction;
/* Adjust heating */
static void correct()
{
      if (ADC.w>tsetpoint.w)  { if (DAC.w>0) DAC.w--; } else
      if (ADC.w<tsetpoint.w)  { if (DAC.w<60000) DAC.w++; };
}
unsigned char lpb=0;
/* All Communication is done by interruption */
static void rs232(void) interrupt 0
{
ClrWdt();
```

```
if (OERR|FERR)
{
    TXEN=0;
    TXEN=1;
    CREN=0;
    CREN=1;
    del7us();
}
// Assume shadow ports have up-to-date data
 if (RCIF) {
    while(RCIF) rs_data = RCREG; // get last byte, ignore the rest
    switch(rs_data) {
/* Relay Channel selections and Ligh Sources On / OFF states */
        case 1:   PORTB_TMP |= 0x08;  break;   // LED OFF
        case 3:   PORTB_TMP |= 0x10;  break;   // LED OFF
        case 11:  PORTB_TMP &= ~0x08;  break;   // LED ON
        case 13:  PORTB_TMP &= ~0x10;  break;   // LED ON
// Relay 1 - 6
        case 21:  PORTB_TMP &= 0x1F; doclk=1;  break;
        case 22:  PORTB_TMP &= 0x1F;
              PORTB_TMP |= 0x20; doclk=1;  break;
        case 23:  PORTB_TMP &= 0x1F;
              PORTB_TMP |= 0x40; doclk=1;  break;
        case 24:  PORTB_TMP &= 0x1F;
              PORTB_TMP |= 0xC0; doclk=1;  break;
        case 25:  PORTB_TMP &= 0x1F;
              PORTB_TMP |= 0x80; doclk=1;  break;
        case 26:  PORTB_TMP &= 0x1F;
              PORTB_TMP |= 0xA0; doclk=1;  break;
        case 29:  PORTB_TMP &= 0x1F;      // POSITION 8 is OPEN
              PORTB_TMP |= 0xE0; doclk=1;  break;
        case 30:  /*PORTA_TMP |= 0x01;
              PORTA = PORTA_TMP;
              superfoo();
              PORTA_TMP &= ~0x01;  */
              break;
/* version and loopback */
       case 31:        TXREG = BOX_VERSION;  //#### Version 02
                TXEN = 1;
                    while (TRMT!=0) ;              break;
       case 32:      TXREG = BOX_SNP1;        //#### serial number part1
                 TXEN = 1;
                 while (TRMT!=0) ;             break;
       case 33:        TXREG = BOX_SNP2;      //#### serial number part2
                    TXEN = 1;
                    while (TRMT!=0) ;              break;
```

```
    case 56:     del7us();                //#### loop back enable
     while(!RCIF) ;
     rs_data = RCREG;
     TXREG = rs_data;
     TXEN = 1;
     while (TRMT!=0) ;          break;
case 120:       while (1) ;           //#### Reset by WDT
            break;
case 76:     del7us();                //#### GET new DAC value
     while(!RCIF) ;
     DAC.b.b0 = RCREG;
     while(!RCIF) ;
     DAC.b.b1 = RCREG;            break;
case 96:        TXEN = 0;             //#### SEND DAC Variable
            TXREG = DAC.b.b0;
            TXEN = 1;
        while (!TXIF);
            TXREG = DAC.b.b1;
        while (!TXIF);
        while (!TRMT);            break;
case 78: adquire = 2;             //#### Enable Write to DAC
     break;
case 80:         adquire = 1;         //#### enable adquire temperature
             break;
case 101:    del7us();                //#### Send ADC Value (Temperature)
         TXEN = 0;
         TXREG = ADC.b.b0;
         TXEN = 1;
     while (!TXIF);
         TXREG = ADC.b.b1;
         while (!TXIF);
         TXREG = ADC.b.b2;
     while (!TXIF);
         TXREG = ADC.b.b3;
     while (!TRMT);          break;
case 105:        del7us(); /* control3 feedback */
         while(!RCIF) ;
         rs_data = RCREG;
                 control3 = rs_data;     break;
case 106:    del7us();                //#### Send Control3 Value (!=0 means on internal
         TXEN = 0;
         TXREG = control3;
         TXEN = 1;
     while (!TRMT);          break;
case 108:    control3 = 10;           //#### Activate internal temperature controll
         break;
```

```
      case 109:        control3 = 0;          //#### Disable internal temperature controll
                  break;
      case 110:    del7us();                  //##### GET Temperature SETPOINT
           while(!RCIF) ;
           tsetpoint.b.b0 = RCREG;
           while(!RCIF) ;
           tsetpoint.b.b1 = RCREG;
           while(!RCIF) ;
           tsetpoint.b.b2 = RCREG;
           while(!RCIF) ;
           tsetpoint.b.b3 = RCREG;     break;
      case 111:      del7us();                //#### Send Temperature Setpoint
             TXEN = 0;
             TXREG = tsetpoint.b.b0;
             TXEN = 1;
             while (!TXIF);
             TXREG = tsetpoint.b.b1;
             while (!TXIF);
             TXREG = tsetpoint.b.b2;
             while (!TXIF);
             TXREG = tsetpoint.b.b3;
             while (!TRMT);      break;
      case 2:      del7us();                  //#### GET DAC Limit and SET
           while(!RCIF) ;
           DAC_LIMIT.b.b0 = RCREG;
           while(!RCIF) ;
               DAC_LIMIT.b.b1 = RCREG;      break;
//#### SEND CALIBRATION FOR ADC, value for ADC=Vref
      case 121:      TXEN = 0;
             TXREG = ADCFACT0;
             TXEN = 1;
             while (!TXIF);
             TXREG = ADCFACT1;
             while (!TXIF);
             TXREG = ADCFACT2;
             while (!TXIF);
             TXREG = ADCFACT3;
             while (!TRMT);      break;
  default:  break;
   }
         if (doclk==1) {
                     PORTA_TMP &= ~0x01;
             PORTA = PORTA_TMP;
                     PORTB = PORTB_TMP;
             superfoo();
                     PORTA_TMP |= 0x01;
```

```
                    doclk=0;
                  }
/* Update ports from shadow ports */
     PORTA = PORTA_TMP;
     PORTB = PORTB_TMP;
    }
}
```

8.4.3 Source code for the microcontroller PIC 16f628 - lt16adc.c

```
//include"lt16adc.h"
#define __16f628
#include"pic/pic16f628.h"
#include "portmap.h"
#define ClrWdt()         do { _asm clrwdt _endasm; } while(0)
typedef union { // This compiler uses byte alignment so we can use
              unsigned long w; // a union for fast 8/32-bit conversion
       struct {
               unsigned char b3; // LSB byte
               unsigned char b2;
               unsigned char b1;
               unsigned char b0; // MSB byte
              }b;
             } iohw_union32;
iohw_union32 ADC;
unsigned long ad16;
unsigned char adct_last[2];
extern unsigned char PORTA_TMP;
extern unsigned char PORTB_TMP;
extern unsigned char tempc;
extern unsigned char i;
extern unsigned char j;
extern unsigned char rs_data;
unsigned char b1, b2, b3;
unsigned char ferror;
void read3times();
void read_SYNCADC();
#pragma save /* save the current settings */
#pragma nogcse /* turnoff global subexpression elimination */
#pragma noinduction /* turn off induction optimizations */
void del7us()
{
_asm
 NOP;
 NOP;
 NOP;
 NOP;
```

```
 NOP;
 NOP;
 NOP;
_endasm;
}
void superfoo() {
 for (j=0;j<100;j++) {
 for (i=0;i<250;i++) del7us(); } }
#pragma restore /* turn the optimizations back on */
void rs_putc()
{
_asm
        BANKSEL _rs_data
    MOVFW _rs_data
    BANKSEL TXREG
    MOVWF TXREG
    BANKSEL TXSTA /* r0x29    BANKSEL TRMT */
    BCF TXSTA,1 /* r0x29 OOOOOOO is not in datasheet _TRMT CLRF TRMT*/
    BSF STATUS,5
    BCF STATUS,6
_rs_putc_loop1:
    BTFSS     _TXSTA_bits,1
    GOTO      _rs_putc_loop1
/*_rs_putc_loop1:
        BANKSEL _TRMT
    BTFSC     (_TRMT >> 3), (_TRMT & 7)
    goto _rs_putc_loop1 */
_endasm;
}
unsigned int PORTA_TMP2;
void read3times()
{
      PORTA_TMP = PORTA;
      PORTA_TMP |= 0x01;
      PORTA_TMP &= ADC_DATA;   // Clear all bits except DATA
       b1 = PORTA_TMP;
      PORTA_TMP = PORTA;
      PORTA_TMP &= ADC_DATA;   // Clear all bits except DATA
      PORTA_TMP |= 0x01;
       b2 = PORTA_TMP;
       if ((b1 & b2) != 0) ADC.w |= 1; else
       if ((b1 | b2) == 0) ADC.w &= 0xfffffffe; else { ferror = 1; }
}
void read_SYNCADC()
{
  ferror = 0;
```

```
  PORTA_TMP |= ADC_CS; /* PUT /CS High */
  PORTA_TMP |= 0x01;
  PORTA = PORTA_TMP;
  PORTA_TMP = PORTA;
  PORTA_TMP |= 0x01;
  PORTA_TMP &= ~ADC_CLK; // ensure CLK is LOW
  PORTA = PORTA_TMP;
  PORTA_TMP &= ~ADC_CS; /* PUT /CS Low  */
  PORTA = PORTA_TMP;
// Check for /EOC
// check first if /EOC is HIGH for more than 3 bits, avoid init data read in wrong position
     ClrWdt();
   while ((PORTA_TMP & ADC_DATA) != 0) {
   //  ferror++;
     PORTA_TMP = PORTA;   /* Check for /EOC  */
     PORTA_TMP |= 0x01;
//      if (ferror>250) return;
  PORTA_TMP |= ADC_CS; /* PUT /CS High */
  PORTA = PORTA_TMP;
   del7us();
  PORTA_TMP &= ~ADC_CS; /* PUT /CS Low  */
  PORTA = PORTA_TMP;
   } /* TODO TIMO should be 200ms */
ClrWdt();
// clock HIGH
 PORTA_TMP |= ADC_CLK;
 PORTA = PORTA_TMP;
     for (tempc=0;tempc<32;tempc++)  {
     // clock down
          PORTA_TMP = PORTA;
                    PORTA_TMP |= 0x01;
          PORTA_TMP &= ~ADC_CLK;
          PORTA = PORTA_TMP;
          PORTA = PORTA_TMP;
                    del7us();
          read3times();
     if (tempc!=31) {
          ADC.w = ADC.w << 1;
          // clock up
          PORTA_TMP = PORTA;
                    PORTA_TMP |= 0x01;
          PORTA_TMP |= ADC_CLK;
          PORTA = PORTA_TMP;
          PORTA = PORTA_TMP;
          }
     }
```

```
  PORTA = PORTA_TMP;
  PORTA_TMP |= ADC_CS; /* PUT /CS High */
  PORTA = PORTA_TMP;
}
```

8.4.4 Surce code for the serial communication with error detection

```
typedef union { // This compiler uses byte alignment! // maximum size is 8 bytes
                unsigned char dat[8];
        struct {
                unsigned char startbyte;
                unsigned char size;
                unsigned char command;
                unsigned char b3; // LSB byte
                unsigned char b2;
                unsigned char b1;
                unsigned char b0; // MSB byte
        unsigned char dummy;
               }b;
              } inbuffermod;
 unsigned char inbuffer_cnt;
 unsigned char ds;
 unsigned char checksum;
 inbuffermod inbuffer;
 inbuffermod oubuffer;
// communications macros
#define SEND_RS232(data1) \
    { while (!TRMT); \
     TXEN = 0; \
         TXREG = data1; \
     TXEN = 1;   \
    while (TRMT!=0); }
#define insert_inbuffer(data1) \
   { inbuffer.dat[inbuffer_cnt] = data1; \
     inbuffer_cnt++; }
#define is_inbuffer_full \
        (inbuffer_cnt==8)
#define reset_inbuffer \
        { inbuffer_cnt=0; \
    inbuffer.b.size=0; }
#define is_newcom \
        ((inbuffer_cnt>2) && (inbuffer_cnt==inbuffer.b.size) && (inbuffer.b.size<9))
#define is_readytosend \
        (oubuffer.b.size!=0)
#define reset_oubuffer \
        (oubuffer.b.size=0)
#define calc_checksum \
```

```
    { \
    checksum = inbuffer.b.startbyte; \
    for (ds=1; ds<inbuffer.b.size -2; ds++) { \
        checksum ^= inbuffer.dat[ds]; \
        } \
    }
#define calc_outchecksum \
    { \
    checksum = COM_START; \
    for (ds=1; ds<oubuffer.b.size -2; ds++) { \
        checksum ^= oubuffer.dat[ds]; \
        } \
    }
// compare calculated checksum with received checksum
#define is_command_valid \
    ((inbuffer.b.startbyte==COM_START) && (checksum==inbuffer.dat[inbuffer.b.size -1]))
```

8.4.5 Code fragment using the serial communication with error detection

```
       if (is_newcom) {
      if (inbuffer.b.startbyte==COM_START) // check formal input
      calc_checksum;
      if (is_command_valid)
{
         switch (inbuffer.b.command) {
               case COM_CLEAR: // only 3 bytes are received, all are 0x03, CLEAR COMMAND
                     oubuffer.b.size = 5;
                     oubuffer.b.command = 3;
                     oubuffer.b.b3 = 0xaa;
                     oubuffer.b.b2 = 0x55;
                     break;
               case COM_BOXNAME: // response is boxname 8/8
                     oubuffer.b.size = 8;
                     oubuffer.b.command = COM_BOXNAME;
                     oubuffer.b.b3 = BOX_VERSION;
                     oubuffer.b.b2 = BOX_SNP1;
                     oubuffer.b.b1 = BOX_SNP2;
                     oubuffer.b.b0 = 'R';
                     oubuffer.b.dummy = 0;
                     break;
               case COM_CHSEL  : // 5/5
                     PORTA_TMP &= ~0x07;
                     channel=inbuffer.b.b3;
                     switch (channel) {
                        case SIGNAL1: PORTA_TMP |= 0x03; break;
                        case SIGNAL2: PORTA_TMP |= 0x02; break;
                        case SIGNAL3: PORTA_TMP |= 0x01; break;
```

```
            case SIGNAL4: PORTA_TMP |= 0x00; break;
            case SIGNAL5: PORTA_TMP |= 0x05; break;
            case SIGNAL6: PORTA_TMP |= 0x04; break;
            case SIGLED1: PORTA_TMP |= 0x06; break;
            case SIGTRIS: PORTA_TMP |= 0x07; break;
            default: channel = 0xff;
            }
        PORTA_TMP &= ~MUX_CLK;
        PORTA = PORTA_TMP;
        PORTA_TMP |= MUX_CLK;
        PORTA = PORTA_TMP;
        oubuffer.b.size = 5;
        oubuffer.b.command = COM_CHSEL;
        oubuffer.b.b3 = channel;
        oubuffer.b.dummy = 0;
        break;
case COM_LOOPBACK: // b3-b0 will be returned for communication tests 8/8
        for (ds=0; ds<8; ds++)
            oubuffer.dat[ds] = inbuffer.dat[ds];
        break;
case COM_RESET: // Re-Set microcontroller using WDT TIMO 4
        while (1);
        break;
case COM_SET_HEAT: // MSB then LSB 6/8
        DAC.b.b0 = inbuffer.b.b3; // DAC.b.b0 is MSB !
        DAC.b.b1 = inbuffer.b.b2;
        ClrWdt();
        write_DAC();
        oubuffer.b.size = 6;
        oubuffer.b.command = COM_SET_HEAT;
        oubuffer.b.b3 = DAC.b.b0;
        oubuffer.b.b2 = DAC.b.b1;
        break;
case COM_GET_HEAT: // MSB then LSB 4/6
        oubuffer.b.size = 6;
        oubuffer.b.command = COM_GET_HEAT;
        oubuffer.b.b3 = DAC.b.b0;
        oubuffer.b.b2 = DAC.b.b1;
        break;
case COM_SET_HEAT_LIM: // MSB then LSB 6/8
        DAC_LIMIT.b.b0 = inbuffer.b.b3; // DAC.b.b0 is MSB !
        DAC_LIMIT.b.b1 = inbuffer.b.b2;
        ClrWdt();
        oubuffer.b.size = 6;
        oubuffer.b.command = COM_SET_HEAT_LIM;
        oubuffer.b.b3 = DAC_LIMIT.b.b0;
```

```
                oubuffer.b.b2 = DAC_LIMIT.b.b1;
                break;
        case COM_GET_ADC: // MSB then LSB 4/8
                oubuffer.b.size = 8;
                oubuffer.b.command = COM_GET_ADC;
                oubuffer.b.b3 = ADC.b.b0;
                oubuffer.b.b2 = ADC.b.b1;
                oubuffer.b.b2 = ADC.b.b2;
                oubuffer.b.b2 = ADC.b.b3;
                break;
        case COM_ADC_SETPOINT: // MSB then LSB 8/8
                tsetpoint.b.b0 = inbuffer.b.b3;
                tsetpoint.b.b1 = inbuffer.b.b2;
                tsetpoint.b.b2 = inbuffer.b.b1;
                tsetpoint.b.b3 = inbuffer.b.b0;
                oubuffer.b.size = 8;
                oubuffer.b.command = COM_ADC_SETPOINT;
                oubuffer.b.b3 = tsetpoint.b.b0;
                oubuffer.b.b2 = tsetpoint.b.b1;
                oubuffer.b.b2 = tsetpoint.b.b2;
                oubuffer.b.b2 = tsetpoint.b.b3;
                break;
        case COM_WRITE_ADCCAL: // MSB then LSB 8/8
                oubuffer.b.size = 8;
                break;
        case COM_WRITE_SERIAL: // MSB then LSB 8/8
                oubuffer.b.size = 8;
                break;
        case COM_WR_LEDSTA: // MSB then LSB 8/8
                oubuffer.b.size = 8;
                // LED.Nr 4 bits // on/off 1 bit // 3bits reserved
                break;
        case COM_WR_LEDCAL: // MSB then LSB 8/8, led calibration to xxx
                oubuffer.b.size = 8;
                // LED.Nr 4 bits // 4 bits reserved, 2 bytes calibration
                break;
        case COM_WR_LEDLEV: // MSB then LSB 8/8, led level
                oubuffer.b.size = 8;
                // LED.Nr 4 bits // 4 bits reserved, 2 bytes level
                break;
        case COM_RD_LEDCAL: // MSB then LSB 8/8, led cal
                oubuffer.b.size = 8;
                // LED.Nr 4 bits // 4 bits reserved, 2 bytes level
                break;
        case COM_RD_LEDLEV: // MSB then LSB 8/8, led level
                oubuffer.b.size = 8;
```

```
                            // LED.Nr 4 bits // 4 bits reserved, 2 bytes level
                            break;
                    case COM_GETTEMP: // MSB then LSB 8/8
                            oubuffer.b.size = 8;
                            break;
                    case COM_SETTEMP: // MSB then LSB 8/8
                            oubuffer.b.size = 8;
                            break;
                    default:
                            break;
                }
            }
        else {
            oubuffer.b.size = 8;
            oubuffer.b.command = COM_ERROR;
            oubuffer.b.b3 = COM_ERROR_CHECKSUM;
            oubuffer.b.b2 = inbuffer.dat[inbuffer.b.size-1]; // received
            oubuffer.b.b1 = checksum; // calculated
            oubuffer.b.b0 = '0';
            }
        reset_inbuffer;
        }
//      else
//      if (is_inbuffer_full) {
//              // return error invalid command
//              SEND_RS232(error_BUFFER_FULL);
//              reset_inbuffer;
//          }
    if (is_readytosend) {
//oubuffer.b.startbyte=COM_START;
_asm
   MOVLW 0x69;
   BANKSEL   _oubuffer;
   MOVWF (_oubuffer + 0);
_endasm;
            calc_outchecksum;
            ClrWdt();
            oubuffer.dat[oubuffer.b.size-1] = checksum;
            while (!TRMT); // must be, loopback is still sending!
                TMR2IE = 0; // disable timer int
                TXEN = 0;
            for (ds=0; ds<oubuffer.b.size; ds++) {
                TXREG = oubuffer.dat[ds];
                        TXEN = 1;
                        while (!TXIF);
                }
```

```
        while (!TRMT);
        TMR2IE = 1; // enable timer int
    reset_oubuffer;
}
```

List of publications

2010 R. Lessmann, Z. R. Hong, S. Scholz, B. Maennig, M. K. Riede, K. Leo. Aging of flat heterojunction zinc phthalocyanine/fullerene C_{60} organic solar cells. Organic Electronics v. 11, pp. 539

2009 V. Kažukauskas, A. Arlauskas, M. Pranaitis, R. Lessmann, M. Riede, K. Leo. Characterization of effective charge carrier mobility in ZnPc/C_{60} Solar Cells after ageing. Physica Status Solidi. C. Current topics in solid state physics, v. 6 pp. 2864

2009 Z. Hong, R. Lessmann, B. Maennig, Q. Huang, K. Harada, M. Riede, K. Leo. Antenna effects and improved efficiency in multiple heterojunction photovoltaic cells based on pentacene, zinc phthalocyanine and C_{60}. Journal of Applied Physics. v. 106. pp. 064511

2007 Z. Hong, B. Männig, R. Lessmann, M. Pfeiffer, K. Leo, P. Simon. Improved efficiency of zinc phthalocyanine/C_{60} based photovoltaic cells via nanoscale interface modification. Applied Physics Letters, v. 90, pp. 203505.

Conferences

2010 V. Kăzukauskas, A. Arlauskas, M. Pranaitis, R. Lessmann, M. Riede, K. Leo. Photoelectrical properties and ageing of ZnPc/C_{60} solar cells. 53rd Scientific Conference for young students of physics and natural sciences, Open Readings PP23, March 24-27, Lithuania

2008 R. Lessmann, Z. Hong, M.K. Riede, K. Leo. Long term aging behavior of ZnPc:C_{60} organic solar cells under controlled conditions SYSA 5.85 Feb. 25-29. DPG Tagung Berlin

2007 R. Lessmann, Z. Hong, B. Maennig, K. Leo. Long-Term Aging Behavior of ZnPc/C_{60} Solar Cells. The 34th International Symposium on Compound Semiconductors, ISCS2007 Oct. 15-18 Kyoto

2006 R. Lessmann, M. Pfeiffer, K. Leo. High Temperature Stable Solar Cells. CPP 23.46 P2, March 27-31. DPG Tagung Dresden

Acknowledgements

This work has a three year history already, and therefore the list of people who helped is long! My speciall thanks to[1]:

- Prof. Leo, to let the students actively take part in decision making and encourage them to colaborate with other institutions and with the industry,
- Mr. Volker Treppte and Mr. Kramer for all the mechanical modifications of the measurement boxes,
- My Group Leaders, cronologically: Martin Pfeiffer, Bert Männig and Moritz Riede, for creating the nice work environment and for discussions, corrections, *usw.*
- all my coleagues from IAPP specially from OSOL and OLED group, for the discussions and also for the friendship that was very necessary during this time.
- Johanna Bohland and Jenny (Konrad's girlfriend) for kindly spending their time on the grammar corrections of this work.
- Christian Uhrich, Karsten Fehse, Ziruo Hong, Qiang Huang, Christian Kolberg, Philipp Sebastian, Robert Franke, Kerstin Schulze, Sebastian Scholz.
- Frau Schmidt and Frau Wortmann for always promptly solving bureoucratic problems.
- Clovis Maia, Edilson, Ivo, and many other brazilian friends for the motivation.
- Kai Schmidt for the help with insect biology.
- Ralf Raupach and Eginhard Wollrab for fruitfull technical discussions.
- Raphael Neider from the SDCC user forum for helps with the compiler.
- To the IAPP for the great working ambient.
- To the CAPES / DAAD program for the scholarship.

---

[1] this list has a random sequence

Versicherung

Hiermit versichere ich, dass ich die vorliegende Arbeit ohne unzulässige Hilfe Dritter und ohne Benutzung anderer als der angegebenen Hilfsmittel angefertigt habe; die aus fremden Quellen direkt oder indirekt übernommenen Gedanken sind als solche kenntlich gemacht. Die Arbeit wurde bisher weder im Inland noch im Ausland in gleicher oder ahnlicher Form einer anderen Prüfungs behörde vorgelegt.

Diese Arbeit wurde am Institut fur Angewandte Photophysik der Technischen Universität Dresden unter der wissenschaftlichen Betreuung von Prof. Dr. Karl Leo angefertigt.

Ich erkenne die Promotionsordnung der Fakultät Mathematik und Naturwissenschaften der Technischen Universität Dresden vom 20. März 2000 an.

Dresden, den 7 Oktober 2009

(Rudolf Lessmann)